

FLOW AND STRUCTURE INTERACTIONS OF MEMBRANE WINGS AT LOW  
REYNOLDS NUMBER

By

AMORY W. TIMPE

A THESIS PRESENTED TO THE GRADUATE SCHOOL  
OF THE UNIVERSITY OF FLORIDA IN PARTIAL FULFILLMENT  
OF THE REQUIREMENTS FOR THE DEGREE OF  
MASTER OF SCIENCE

UNIVERSITY OF FLORIDA

2012

© 2012 Amory W. Timpe

To my mother, father, sister and brother

## ACKNOWLEDGMENTS

Foremost, I would like to thank my advisor Dr. Larry Ukeiley for providing me with an opportunity to study and research at the University of Florida: Research and Engineering Education Facility (UF-REEF); for his direction, guidance, teachings, and insight. Thanks are also extended to my committee members, Dr. Lou Cattafesta and Dr. Peter Ifju, for their support and input, throughout.

To my colleagues and friends at REEF I am very appreciative; this work would not be possible without their academic and recreational support. Particular thanks to fellow members of the REEF Unsteady Fluid Dynamics Group: Adam Hart, Taylor Lusk, Erik Sällström, and office mate Diego Campos for their camaraderie and many great discussions, both inside and outside of research.

Additional thanks to Zheng Zhang and Alex Arce for assistance with setup and acquisition during experiments. I would like to acknowledge the work of Yaakov Abudaram, a colleague and friend who also created the membrane portions of models tested, and Dr. Pin Wu who assisted in developing the methods used for synchronized experiments. The guidance of Dr. James P. Hubner at the University of Alabama is also greatly appreciated. I enjoyed the collaboration of this project, supported by the Air Force Office of Scientific Research (Grant FA9550-10-1-0152) under program manager Dr. Doug Smith, and by the Florida Center for Advanced Aero-Propulsion (FCAAP).

Finally, I acknowledge the love and support of my family who have provided me with the strength and encouragement to overcome the challenges endured in research and in life.

## TABLE OF CONTENTS

	<u>page</u>
ACKNOWLEDGMENTS.....	4
LIST OF TABLES.....	7
LIST OF FIGURES.....	8
LIST OF ABBREVIATIONS.....	11
ABSTRACT.....	13
CHAPTER	
1 INTRODUCTION.....	15
Motivation for Research.....	15
Membranes Applied to MAV's.....	16
Research Background.....	17
Perimeter-Reinforced Membranes.....	19
Batten-Reinforced Membranes.....	21
Free trailing-edge behavior.....	22
Precursor studies.....	23
The Present Research.....	24
2 EXPERIMENTS.....	26
Facilities and Instrumentation.....	26
Aerodynamic Characterization Facility.....	26
PIV System and Processing Details.....	27
PIV processing.....	27
Camera arrangement.....	28
Flow seeding.....	28
Stereo DIC System and Processing Details.....	31
Procedure and lighting.....	31
DIC processing.....	32
Synchronization of PIV and DIC Systems.....	34
Membrane Models.....	36
Experiments Performed.....	39
Synchronized PIV and DIC Tests.....	40
Independent DIC Measurements.....	42
PIV Measurements of 80x80_2.8ε Wing.....	43
Post Processing/Analysis.....	44
Dynamic Masking Algorithm.....	44

3	RESULTS .....	47
	Velocity Measurements.....	47
	Time-Averaged Velocity Fields.....	48
	Streamwise velocity at low aoa .....	48
	Streamwise velocity at high aoa.....	50
	Root-Mean-Square Velocity Fluctuations .....	52
	Streamwise velocity fluctuations .....	52
	Vertical velocity fluctuations .....	54
	Reynolds Shear Stress.....	55
	Membrane Oscillation Behavior .....	58
	Full-Field Mean and RMS Properties .....	59
	Pointwise mean and rms properties.....	61
	Time-averaged camber effect .....	62
	Membrane Frequency Content.....	62
	Fluid Structure Interactions .....	65
	Trailing-Edge Vorticity Interaction.....	65
	Flow and Membrane Coupled Behaviors .....	69
	Spectral analysis applied to flows .....	69
	Correlation analysis .....	70
4	CONCLUSIONS AND FUTURE WORK .....	98
	Summary .....	98
	Future .....	101
	APPENDIX: DYNAMIC MASKING .....	102
	LIST OF REFERENCES .....	106
	BIOGRAPHICAL SKETCH.....	112

## LIST OF TABLES

<u>Table</u>	<u>page</u>
2-1 Model dimension values .....	38
2-2 Silicone material properties .....	38
2-3 Membrane model properties.....	38
2-4 Data types acquired for each model .....	39
3-1 Estimated proportionality constant and natural frequency .....	72

## LIST OF FIGURES

<u>Figure</u>		<u>page</u>
1-1	Low Re membrane wing flyers .....	25
1-2	Example of lufting during LV and hotwire tests.....	25
2-1	ACF, low speed wind tunnel .....	27
2-2	PIV dual camera setup and seed disperser.....	30
2-3	PIV images showing combined FOV's.....	30
2-4	Installed DIC system and speckled model.....	32
2-5	Cartesian coordinate system used with both PIV and DIC data results.....	33
2-6	DIC images and PIV laser interference .....	35
2-7	TR-PIV & DIC systems with model installed for synchronized data acquisition..	35
2-8	BR Silicone membrane wing models with scalloped trailing edges .....	37
2-9	Model schematic with dimensions .....	37
2-10	Measured pre-strain vs. creation temperature .....	38
2-11	Convergence of PIV statistics vs. sample count.....	41
2-12	Synchronous acquisition of PIV and DIC data .....	42
2-13	Symmetric airfoil standoff mounts with 80x80_2.8ε model. ....	43
2-14	Combined instantaneous PIV and DIC at center span .....	46
3-1	U <sub>mean</sub> /U <sub>∞</sub> contours with streamlines for baseline rigid plate.....	73
3-2	U <sub>mean</sub> /U <sub>∞</sub> contours with streamlines for 1.3ε membrane wing .....	74
3-3	U <sub>mean</sub> /U <sub>∞</sub> contours with streamlines for 2.8ε membrane wing .....	75
3-4	U <sub>mean</sub> /U <sub>∞</sub> slice plots at x/c = 0.2, 1.4 for low aoa .....	76
3-5	U <sub>mean</sub> /U <sub>∞</sub> slice plots at x/c = 0.3, 1.4 for high aoa.....	77
3-6	U <sub>rms</sub> /U <sub>∞</sub> contours comparing wings at low aoa.....	78
3-7	U <sub>rms</sub> /U <sub>∞</sub> contours comparing wings at high aoa.....	79

3-8	Vrms/ $U^\infty$ contours comparing wings at low aoa. ....	80
3-9	Vrms/ $U^\infty$ contours comparing wings at high aoa.....	81
3-10	RSS/ $U^\infty^2$ contours comparing wings at low aoa. ....	82
3-11	RSS/ $U^\infty^2$ contours comparing wings at high aoa.....	83
3-13	RMS membrane displacements $y/c$ , for 1.3 $\epsilon$ , 2.8 $\epsilon$ , and 4.2 $\epsilon$ wings. ....	84
3-14	Indication of mid point, side point, and TE point on 1.3 $\epsilon$ , $\alpha=8^\circ$ , mean plot. ....	85
3-15	Mid Point mean and RMS deformation behavior vs. aoa.....	85
3-16	TE Point mean and RMS deformation behavior vs. aoa.....	86
3-17	Time-averaged displacements (camber) of mid and TE points, full $\alpha$ -sweep ....	87
3-18	PSD computed from membrane Mid, Side, and TE Points.....	87
3-19	Spectral content portraying unique behavior of high pre-tension 4.2 $\epsilon$ wing.....	88
3-20	RMS properties for 4.2 $\epsilon$ wing at high aoa.....	88
3-21	Vibration frequency vs. aoa for 1.3 $\epsilon$ , 2.8 $\epsilon$ , and 4.2 $\epsilon$ membrane wings. ....	89
3-22	Normalized instantaneous vorticity, $\omega^*$ , with streamlines at $\alpha = 8^\circ$ .....	90
3-23	Normalized instantaneous vorticity, $\omega^*$ , with streamlines at $\alpha = 12^\circ$ .....	91
3-24	Normalized instantaneous vorticity, $\omega^*$ , with streamlines at $\alpha = 16^\circ$ .....	92
3-25	Normalized instantaneous vorticity, $\omega^*$ , with streamlines at $\alpha = 24^\circ$ .....	93
3-26	PSD's showing membrane frequency in the flow field for 1.3 $\epsilon$ , $\alpha = 8^\circ$ .....	94
3-27	Correlation coefficient computed from TE $m'$ and $u'$ fluctuating signals.....	95
3-28	Correlation coefficient computed from TE $m'$ and $v'$ fluctuating signals.....	96
3-29	Cross correlation, $\rho(\tau)$ , indicating periodic nature of the correlation values .....	97
A-1	2 <sup>nd</sup> frame PIV image, 80x80_2.8 $\epsilon$ at 12 $^\circ$ aoa.....	102
A-2	Polynomial line tracking bright-pixel membrane shape.....	103
A-3	Example mask where membrane resides.....	103
A-4	2 <sup>nd</sup> frame PIV image, 80x80_2.8 $\epsilon$ at 12 $^\circ$ aoa showing shadow .....	104

A-5	Blurred image after convolution with 7x7 mean filter. ....	105
A-6	Example mask generated for dark regions. ....	105

## LIST OF ABBREVIATIONS

ACF	Aerodynamic Characterization Facility
aoa; $\alpha$	Angle of Attack
APG	Adverse Pressure Gradient
AR	Aspect Ratio
BR	Batten Reinforced
CMOS	Complementary Metal-Oxide-Semiconductor
DFT	Discrete Fourier Transform
DIC	Digital Image Correlation
FFT	Fast Fourier Transform
FOV	Field of View
FSI	Fluid-Structure Interaction(s)
IA	Interrogation Area
L/D	Lift/Drag; Aerodynamic Efficiency
LCO	Limit Cycle Oscillation
LE/TE	Leading Edge/Trailing Edge
MAV(s)	Micro Air Vehicle(s)
PIV	Particle Image Velocimetry
POD	Proper Orthogonal Decomposition
PR	Perimeter Reinforced
PSD	Power Spectral Density
Re	Reynolds Number
REEF	Research and Engineering Education Facility
RSS	Reynolds Shear Stress
St	Strouhal Number

TKE	Turbulent Kinetic Energy
TR	Time-Resolved
UA	University of Alabama
UF	University of Florida
We	Weber Number
1D	One Dimensional
2D	Two Dimensional
3D	Three Dimensional

Abstract of Thesis Presented to the Graduate School  
of the University of Florida in Partial Fulfillment of the  
Requirements for the Degree of Master of Science

FLOW AND STRUCTURE INTERACTIONS OF MEMBRANE WINGS AT LOW  
REYNOLDS NUMBER

By

Amory W. Timpe

May 2012

Chair: Lawrence S. Ukeiley  
Major: Aerospace Engineering

The inherent challenges associated with low Reynolds number flight have stemmed biologically inspired wing designs incorporating highly flexible membranes. Natural membrane wing flyers demonstrate advantages of passive flexibility, showing extremely stable and agile flight. Much of the flow and structure dynamics and how they are coupled, however, remain largely unknown. This work discusses an experimental effort to study the fluid-structure interactions of flexible membrane wings at low Reynolds number by synchronized acquisition of Particle Image Velocimetry and Digital Image Correlation. The membrane wings are batten-reinforced flat plates with multi-cell, scalloped membrane sections similar to some micro air vehicle designs. The data analyzed in this research consists of time-resolved, two-component flow measurements over the model/membrane surface as well as in the near wake, and three dimensional membrane displacement measurements. The flow over a baseline rigid flat-plate is included to compare time-averaged flow properties and investigate how the membrane wings alter the flow for possible aerodynamic advantage. A collaborative and parallel force study was performed on identical wings and some results are incorporated.

Membrane wing models of varying pre-tension, created through a membrane heating process, were employed in the investigation to better understand how tension affects the flow behavior, frequency response, and flexibility of compliant wings. The time-dependent dynamics of velocity and membrane vibrations indicate that membrane fluctuations have a strong influence on the surrounding flow, affecting the shear layer emanating from the wings' leading-edge and the development of the flow in the models' near wake. Membrane oscillations are shown to manipulate the flow causing enhanced turbulent characteristics and favorable mean flow fields. Spectral and correlation analysis show quantitative evidence of membrane vibrations driving flow behavior both over the wing and in its wake.

## CHAPTER 1 INTRODUCTION

### **Motivation for Research**

Passive and flexible lifting surfaces have been utilized in the planforms of many flight systems, including: Micro Air Vehicles (MAVs), hang gliders, paragliders, microlight wings, sails, and power kites where the flexibility and passive shape adaption have demonstrated significant performance advantages [1]–[7]. The underlying physics of the fluid-structure interactions, the nature of the surrounding flow and of the ‘structural’ vibrations, their coupled aero-elastic behavior, and the effects of pre-tension are all key aspects that are currently being studied. Much of the inspiration for implementation of these flexible membranes and materials comes from observed biological systems with adaptive wings performing extremely agile flight and maintaining stability in turbulent and gusty conditions [8]–[12]. The use of flexibility in natural flyers is in particular found for those flying in the low Reynolds number (Re) regime ranging from  $10^4$  through  $10^5$  based on chord length, like various species of insects, bats, and small birds [11], [13]. The fluid-structure interactions (FSI) are significantly different and advantageous in this regime, as compared with those of more understood high Re systems, often the cause of detrimental effects. A better understanding of the low Re FSI is desired.

There are numerous challenges to biological and manmade flight systems operating at low Re. The oncoming flow encountering the wing or planform has less initial momentum and easily separates from shearing and in the presence of a typical adverse pressure gradient (APG), aft of the wing leading edge (LE). The separating flow can rapidly transition to turbulence and sometimes reattach as a turbulent boundary

layer, forming a closed region of separation designated as a separation bubble [15]. This LE separation is in contrast to the trailing edge (TE) separation that is seen for airfoils of high Re systems. The phenomenon is exacerbated by the typically thin wings (minimizing weight) and sharp leading edges of low Re flyers [14]. The presence of a separation bubble causes reduced lift and increased drag by altering the pressure distribution and changing the effective thickness and shape of the airfoil [15]; therefore it is paramount to minimize the size or presence of a bubble for efficient flight [16]–[18].

Additional challenges include the low mass and inertia of the characteristically small and slow flying (10-20 m/s) vehicle or natural flyer, as well as the turbulent low altitude flight conditions, and wind gusts on the order of flight speed. Also, the need for sufficient lifting planform surface area while constrained to a small total wingspan leads to low aspect ratios (ARs), which are susceptible to highly three dimensional effects and roll instabilities [19]. These combined challenges easily lead to unstable flight. It is through the use of adaptable and flexible lifting surfaces that many of these obstacles can be overcome. Examples of manmade and biological low Re flyers that benefit from compliant wings can be seen in Figure 1-1. The major aim of this research is to increase the knowledge and understanding of low Re flow around membrane wings and to experimentally characterize the fluid-structure interactions by novel implementation of synchronized Particle Image Velocimetry (PIV) and Digital Image Correlation (DIC) acquisition techniques.

### **Membranes Applied to MAV's**

Circa 1995 the Defense Advanced Research Projects Agency (DARPA) provided a definition and vision for the MAV. It would be smaller than six inches (15 cm) in total wingspan, be easily deployable, and utilize autonomous navigation [20]. Primarily as a

reconnaissance and sensing device, the vehicle would need to be as stable and adaptable to adverse flight conditions as possible [21], [22]. Thus, after one hundred years of technological development of human flight (even spaceflight), the field of aerodynamics was pursuing extensive knowledge/designs in the envelope where nature had pioneered flight for millennia [23]. The challenge would be met by many research institutions and governments worldwide and over a period of ten or so years, through intuition and mostly ad hoc methods, capable MAVs were created [24]–[26]. This excerpt from an early MAV designer describes the difficult and iterative nature of the design/test processes while creating a working vehicle:

“In order to conduct a free flight test the plane would be turned on, the controls checked, and then the MAV would be launched into the air by hand. The pilot would then attempt to keep the MAV in the air. All present parties would keep strict attention on the plane in order to diagnose any problems. Most free flight tests only last 2 seconds. Free flights were a very iterative process [27].”

As MAV development evolved, bio-inspired systems were created using lightweight composite materials with flexible wing frames and latex membranes as part of the lifting surface, pioneered at the University of Florida [28], [29]. In addition to being extremely light, it was discovered that the use of flexible frames and membrane wings produced benefits like gust alleviation, adaptive washout, adaptive camber, geometric twisting, and delayed stall [1], [2]. Through detailed study of low Re aeroelastic FSI, efficient and stable vehicles or wings could be designed smarter, specifically tailored, and more robustly so.

### **Research Background**

Work by Smith and Shyy (1996) investigated flexible membrane airfoil behavior built upon the earlier works of Thwaites, Nielsen, and others [30]–[33]. This led to the

definition of membrane aeroelastic stiffness parameters  $\pi_1$  and  $\pi_2$ , which account for the relation of membrane ‘stiffness’ to dynamic pressure. Defined in Eqs. 1-1 and 1-2,  $\pi_1$  is used with untensioned membranes, while  $\pi_2$  accounts for pre-tension [34]. In these equations, E is the elastic modulus,  $^0S$  is the membrane pre-stress, nominal pre-tension is:  $T_0 = (^0S + E\varepsilon)$ , while  $\varepsilon$  is % pre-strain, t is the membrane thickness, b’ represents the membrane cell span, and  $q_\infty$  is the dynamic pressure based on freestream velocity.

$$\Pi_1 = \left( \frac{Et}{q_\infty b'} \right)^{1/3} \quad (1-1)$$

$$\Pi_2 = \left( \frac{{}^0St}{q_\infty b'} \right) \quad (1-2)$$

In 2003, Lian, Shyy and coworkers produced a seminal paper laying the foundation for coupled flow and structure computational solvers and utilized Proper Orthogonal Decomposition (POD) techniques to identify flow structures from the numerical results. They noted the “self-initiated vibration” of membrane wings that would be a subject of much further investigation [1]. A group from Brown University including Song, Tian, Swartz, Bishop, and Breuer (et al.) focused specifically on biological membrane flyers/gliders such as bats, flying-squirrels, and sugar gliders; noting the extremely high angles of attack (aoa;  $\alpha$ ) often observed ( $\alpha > 30$ ) and associated delay in stall exhibited by membrane wings. Their work has also focused on the importance of Weber number (We), which they define as the ratio of aerodynamic forces to membrane stiffness, as in Eq. 1-3, and appears very similar in form to the inverse of Smith and Shyy’s:  $\pi_1$  &  $\pi_2$  parameters from Eqs. 1-1 & 1-2, incorporating coefficient of lift,  $C_l$ . In some of their work pre-strain was shown to improve aerodynamic efficiency, pre-stall. It was theorized that the articulating joints connected to flight surfaces of flying-squirrels

and bats, which allowed altered membrane tension or LE shape during flight, were morphological adaptations to take full advantage of such effects. [9], [11], [35]–[37].

$$We = \left( \frac{C_l * 0.5\rho U_\infty^2 c}{Et} \right) \quad (1-3)$$

Once fully understood, in-flight (or pre-flight) alterations to membrane tension or shape, in addition to the passive control, could optimize the performance of manmade systems. Arbos-Torrent et al. showed that small changes in LE and TE shape (flat, round) or size can significantly affect the maximum camber and wake shedding or deficit characteristics for compliant wings. Small flat geometry seemed optimal over the tested  $\text{aoa}$ 's (0-22°) [38].

Much of the work on membrane wings has been divided into two groups, depending on whether the membrane is secured to framing on all edges (perimeter-reinforcement, PR) or if it has batten support and a free trailing-edge (batten-reinforcement, BR). While much of the FSI and physics will be similar for any vibrating membrane configuration, planform lift and drag coefficients can differ, vibration modes will differ, and the system dynamics can be affected by attachment type.

### **Perimeter-Reinforced Membranes**

Rojratsirikul, Wang, and Gursul have performed a series of studies on two dimensional, then low AR latex membrane airfoils; attaching the membranes to rigid leading and trailing edges. They used force data and high-speed PIV to try and characterize the unsteady FSI varying  $\text{Re}$  (53, 80, 106 k) and  $\text{aoa}$  (9-30°), also using laser reflection and independent DIC to study membrane shapes and modes. Notable conclusions included that the membrane's unsteady oscillations provided a form of passive flow control, delaying stall compared with rigid airfoils cambered to the time-

averaged membrane shape, and that oscillations coupled with unsteady behavior in the shear layer as well as possibly with wake vortex shedding [5], [39]. Another of their investigations included 2D membranes with pre-strain ( $\varepsilon = 0, 2.5, 5\%$ ) and excess length factors ( $\delta = 0, 2.5, 5\%$ ), where excess length is the opposite of pre-strain; reporting that pre-strain showed behavior similar to that of a rigid model, while excess length could reduce the amount of flow separation, and induce vortex roll-up [40]. Gordnier and Visbal used a 6<sup>th</sup> order Implicit LES aerodynamic solver coupled to a nonlinear finite element (membrane displacement) solver to numerically model the FSI for the same membrane as in the Gursul studies at 8° and 14° aoa. They reported reasonable qualitative correspondence with the experimental results when sufficient grid resolution was used, capturing vortex shedding from the leading edge, vortex roll-up in the shear layer, and coupling of shedding with the structural vibration behavior [41]. Additional coupled, viscous flow numerical solvers were performed by Tiomkin, Raveh, and Arieli for 2D membrane with parameters of pre-tension, Re, and membrane slack. They found that pre-tension, excess length (slack), and elasticity did not have a major effect on the Strouhal number (St) of shedding but pre-tension and aoa did significantly affect the amount of camber and location of maximal camber [42].

A recent work by Gordnier and Attar detailing aeroelastic simulations of an AR = 2 flexible membrane wing with 3D effects at 16° aoa, (corresponding to the low AR experiments of Gursul et al.) showed enhanced lift and reduced separation but overall the aerodynamic efficiency (L/D) was less for the membrane wing than for the rigid wing [43]. Although there has been reasonable agreement between experimental work and simulations, additional experiments are necessary as parameters such as Re, sharp vs.

rounded LE, and AR in addition to attachment style all show significant impact on the FSI behavior. A final recent study by Tregidgo, Wang, and Gursul (2011) at University of Bath employed independent force measurements, DIC, and PIV to further study low AR membrane wings at low Re (46 k) through an  $\alpha$ -sweep (0-25° by 1°). They reported strong tip effects, which perhaps caused enhanced lift coefficients. Fourier analysis of the membrane oscillations revealed regimes of specific modal vibration characteristics and a low frequency spanwise beating existed at high aoa, which was speculated to possibly cause roll instability. The beating may have been associated with wingtip vorticity impingement [44]. A common theme amongst PR membrane wings is modal and beating vibration behavior, a 1D relation might be standing waves and nodes for a string fixed at both ends; while the effects on control and stability are topics of further research.

### **Batten-Reinforced Membranes**

Tamai, Murphy, and Hu of Iowa State University (2008) did a study of the FSI for BR membrane wings (free TE) in the low Re regime, utilizing PIV. The study investigated the effects of batten spacing (1, 2, 3, and 10 battens, fixed span). Like other studies, they found that membrane models out-performed the rigid model in L/D by passive shape adaption changing the effective aoa, relieving the APG on the model top surface, and resisting separation while delaying stall. It was noted that membrane stiffness and batten spacing are significant parameters for performance because high flexibility was needed for optimal benefits, but an overly slack free trailing edge would 'flutter' at low aoa. This TE flutter, also known as TE flip, lufting, and flapping, when occurring, would cause increased drag and reduced lift, degrading aerodynamic performance [45].

## Free trailing-edge behavior

Some discussion is needed about the vibration behavior of a BR membrane which has a free TE. Starting with the basic physics, the membrane will have a resting tension value (pre-tensioned or not) that should be roughly symmetric in the spanwise direction, while higher near the LE attachment and lower at the free TE in the chordwise direction. This creates an area of lowest tension at the TE. When in a flow, the aerodynamic pressure forces will act on the membrane surfaces and if strong enough will cause distention, which increases the tension and causes an elastic response. The membrane response velocity carries inertial forces which interact further with the unsteady pressure forces and tension; therefore a vibration pattern sets up. Vibrations were found to be small below an onset velocity, after which, a self-sustained instability occurs due to underdamping in the system. At this point oscillation spectral energy increases by two orders, studied by Scott and Hubner et al. [46] but was not a focus of this research.

The oscillations after onset are wave-like in nature and nearly periodic. The 1D relation might be close to a vibrating string with a free end, while this would fail to account for the nonlinearities in the system and dynamic (pressure) driving forces. These motions were described as “self-initiated vibration” in the early work of Lian and Shyy (2003), and later described as Hopf-Bifurcation into Limit Cycle Oscillations (LCOs) in the works by Johnston, Romberg, Attar, Parthasarathy, and Gordnier (2010, 2011) [47], [48], explicitly studying the motions for varying pre-strains ( $\epsilon = 2, 5, 7, 10\%$ ) and fixed geometry.

If the membrane trailing-edge is not highly pre-tensioned, it easily yields to pressure and inertial forces and an out-of-phase and chaotic behavior can exist. These flapping, whip-like motions at the TE, described as “TE flip” by Johnston et al. and “TE

flutter phenomena” by Tamai and Hu, hinder aerodynamic performance. In this work the phenomena will be called ‘lufting’ and is portrayed in Figure 1-2.

### **Precursor studies**

There has been a direct line of studies leading to this work, which were performed by researchers at the University of Alabama (UA) and the University of Florida (UF). Mastramico and Hubner used hot-wire anemometry to investigate the wake characteristics (width, momentum deficit, spectral energy) of thin, flat and cambered plates with high AR and repeating membrane cells, BR and PR versions. PR models often showed broadest wakes while both BR and PR models had larger drag coefficients than the baseline at most  $\alpha$ 's. The wake profiles with narrowest and least deficit velocity, as to minimize drag, were seen for those models that had batten-reinforced and scalloped membranes (BR-S) [49]. Scalloping the free TE (similar to bat wings, Figure 1-1C) removes the lowest tensioned portion of the membrane cells and reduces or eliminates the deleterious lufting, discussed previously. Hubner and Hicks performed a study on scalloping depth (12.5, 25, 37.5% of cell span) as well as membrane cell size (cell AR = 1, 0.75, 0.5), to find which showed the most aerodynamically efficient lift to drag characteristics, for high aspect ratio flat-plate membrane wings at low Re (<61,000). Of the tested geometries, efficiency was best for membrane cells of AR = 1, with a 25% of cell span scallop [50]. While much was learned from flow visualization, force measurements, and the pointwise techniques of hotwire and laser-vibrometry (Figure 1-2), more expansive understanding required further detailed investigation.

## The Present Research

This effort will seek to gain more insight into the FSI by expanding to full-field, time-resolved, and synchronized flow and membrane measurements. The flow data will be obtained by high-speed PIV and simultaneously, the spatially and temporally resolved 3D motions of the membrane will be captured by DIC. Synchronization of the two systems was a major aim to directly visualize, study, and correlate membrane and flow behavior. The steady and unsteady FSI of flow surrounding membranes; and how structural vibrations permeate to, interact with, or otherwise influence the flow in a time-dependent nature will be discussed.

Overall, an experimental investigation to characterize the flow and structure behavior, including time-averaged and dynamic responses, for batten-reinforced scalloped membrane wings of varying pre-tension is presented with comparisons to a baseline flat-plate. Wings were created with improved membrane material (silicone) and aerodynamically beneficial geometries derived from precursor studies [46], [49], [50]. Reliable pre-tensioning of the silicone membranes is prescribed through a heating technique [51]. A method is developed for successful acquisition of synchronized high-speed PIV and DIC systems.

Chapter 2 will discuss the experimental facilities and equipment used; processing details, synchronization methods; along with various aspects of the specific experiments performed. Results of flow field measurements, structural behavior, and the fluid-structure interactions will be discussed and presented in Chapter 3. Ultimately, Chapter 4 will draw some conclusions and include a discussion of future directions for this research.

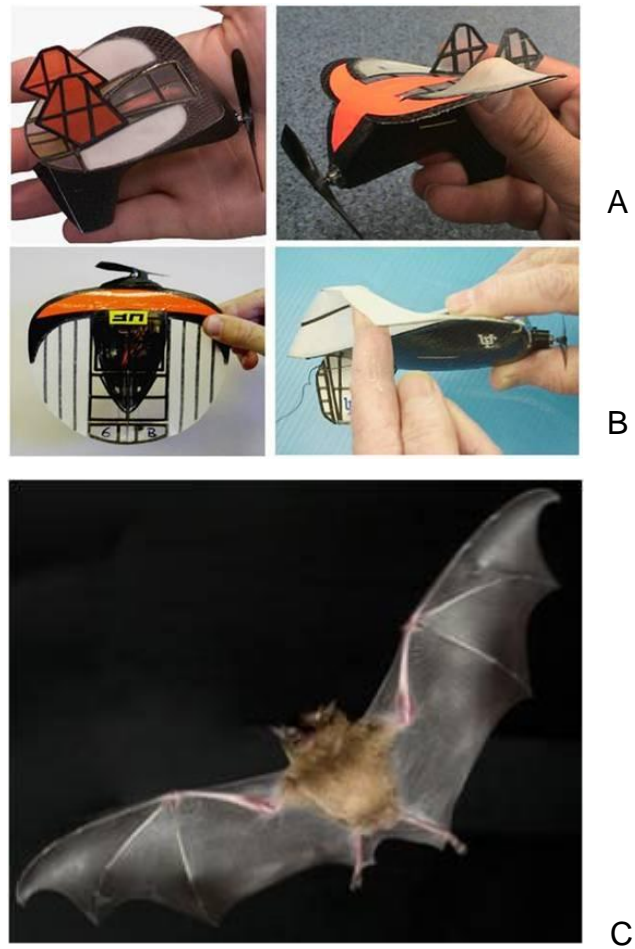


Figure 1-1. Low Re membrane wing flyers. A) PR-MAV. B) BR-MAV. C) Bat.  
 (Sources: A,B: [2],  
 C:<http://www.aaas.org/news/releases/2007/0510bats.shtml>)

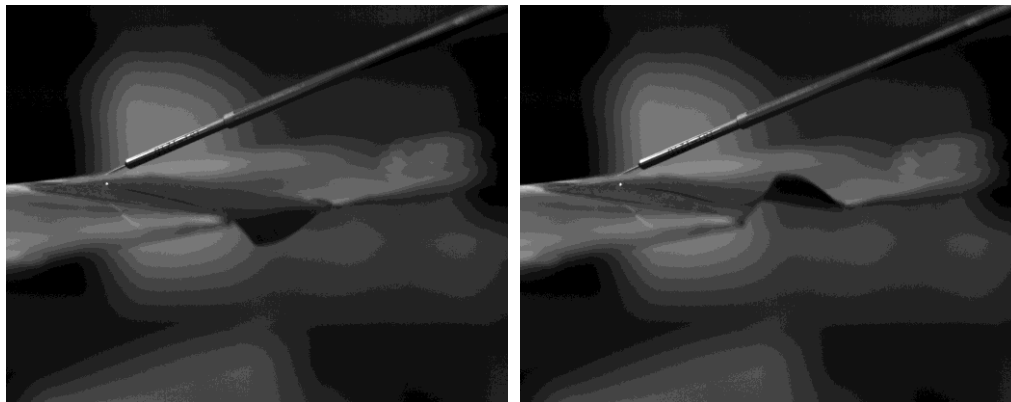


Figure 1-2. Example of luffing during LV and hotwire tests performed at UF in collaboration with UA.

## CHAPTER 2 EXPERIMENTS

The following chapter provides details of the experimental facilities, testing equipment, models tested, experiments conducted, and processing. It shall describe precisely how experiments were set up and performed. A description of the experimental facilities and testing equipment utilized, along with details of how data was processed is included. There will also be a discussion of how models used for testing were created, their geometric details, and in which experiments each was involved.

### **Facilities and Instrumentation**

The experiments for this study were performed in the University of Florida's Aerodynamic Characterization Facility (ACF) which is a wind tunnel specifically designed for the study of low Reynolds number fluid-structure interaction problems.

#### **Aerodynamic Characterization Facility**

The ACF is a suction-style wind tunnel with an open jet test section and an open return air path. It is designed specifically to create a low turbulence environment with steady flow in the range of approximately 1 to 20 m/s, ideal for low Re research. The air is driven by a 37.3 kW, 1.52 m diameter axial blower combined with a variable frequency drive. Turbulence is minimized by straightening the flow after it passes through the bell mouth entrance with a metal honeycomb and multiple settling screens. After conditioning the flow there is a settling chamber and then the flow passes through an 8:1 area ratio contraction. Once contracted, the flow enters the open jet test section as a 1.07 m by 1.07 m square jet and the test section itself is 3.05 m in length. The jet test section is housed in an enclosure (3.7 m by 4.6 m by 3.4 m, w x l x h). Photographs of the ACF are included in Figure 2-1. At the working velocity of 10 m/s, and near to the

jet inlet, the flow has been characterized with a potential core of 90% of the inlet contracted exit area and with a turbulence intensity,  $\frac{|u'|}{U}$ , of 0.16%. Albertani et al. provides a more thorough analysis of the ACF [52].

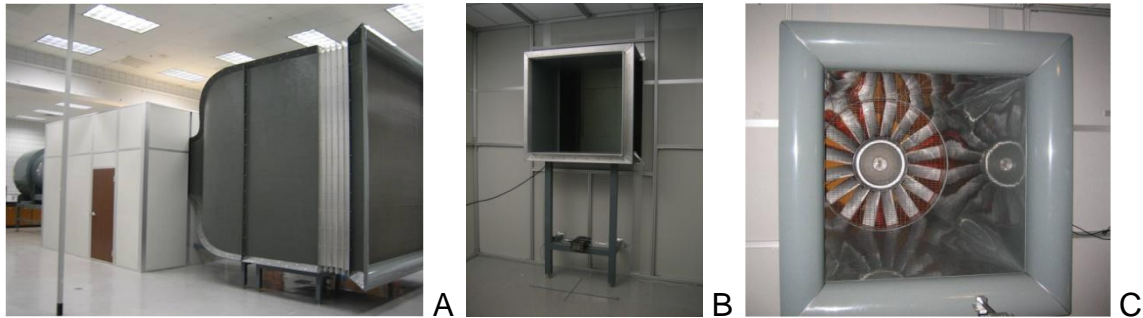


Figure 2-1. ACF, low speed wind tunnel. A) External View. B) Jet Exhaust. C) Diffuser/Blower.

### PIV System and Processing Details

A *Dantec Dynamics* time-resolved (TR) particle image velocimetry system was used to acquire the flow field measurements during experiments. Images were obtained by a pair of *IDT XS-5* high-speed CMOS cameras (Figure 2-2A) each equipped with *Sigma EX* 105 mm f-length macro lenses set to  $f/\#$  2.8, and 2GB of onboard memory. The PIV system also consisted of a *Lee Laser Series 800* double-cavity Nd:YAG laser set to a wavelength of 532 nm. The laser has 6kW of power, providing 1.35 mJ/pulse. In general, the PIV system could sample double-frames at a rate from 500 to 1000 Hz, limited by the speed of the cameras and at what pixel resolution the images were set to. *Dantec Dynamics'* *Dynamic Studio v3.10* software was used to operate and control the system as well as to process the images.

### PIV processing

Vector fields were generated through a multi-step process. The raw images were first acquired; then a noise background image was created by sampling 50 images with

the lens caps on and taking the average. The background image was then subtracted from each image of the data sets. This helped reduce the CMOS sensor noise generated by sampling near the cameras' maximum frame rates. New noise background images were created as needed to adjust for the cameras' sensitivity to temperature over time. The image sets (with noise background removed) were then processed by a four-step, adaptive-windowing correlation technique; each refinement using 2 passes and reducing the interrogation area (IA) size. The IA's went from 128 by 128 pixels to a final step of 16 by 16 pixels. The algorithm utilized a central difference IA offset scheme and 25% region overlap.

### **Camera arrangement**

The cameras were set up such that two fields of view (FOV's) were utilized in 2D-PIV fashion. One camera using a slightly smaller FOV, was focused over the membrane/model for improved detail and accuracy near the model surface. The second camera with a slightly larger FOV, was focused on the model near-wake; also slightly overlapping the first camera's view. The processing methods and camera FOV's provided vector spatial resolutions of: 1.24 vectors/mm for the model camera and 0.92 vectors/mm for the wake camera. Figure 2-3 portrays the cameras' fields of view during acquisition, including two separate experiments; one performed later, in which the seeding technique was improved.

### **Flow seeding**

The seed particles used to track the flow were generated by an ATI Technologies tda-4B aerosol generator. The Laskin nozzles housed within the generator atomized olive oil into particles of diameter 1-5  $\mu\text{m}$ ,  $d_p$ , as quoted by ATI. Using Stoke's flow assumption for very small diameter spheres where  $\rho_p \gg \rho_f$ , ( $\rho_f$  represents fluid density,

for air  $\rho_f \approx 1.20 \text{ kg/m}^3$ , while  $\rho_p$  is the particle density,  $\rho_p \approx 970 \text{ kg/m}^3$ , the relaxation time of these olive oil particles can be defined as Eq. 2-1 [53]. Relaxation time defines how quickly the particles can respond to changes in the flow. Using  $\mu = 1.75\text{E}^{-5} \text{ kg/m}\cdot\text{s}$  for air (70 °C),  $\tau_r$ , is found as  $2.8\text{E}^{-5} \text{ s}$  (order of kHz), which agrees well with Strömungsmechanik [54]. This means these small particles respond to the flow tendencies well and satisfactory for flow scales under investigation.

$$\tau_r = d_p^2 \frac{\rho_p}{18\mu} \quad (2-1)$$

When using very small particles the particle diameter at the image plane (effective particle size,  $d_e$ ) is important. Diffraction will cause the reflected light to spread as an Airy disk and this diffraction limited particle size,  $d_s$ , is defined as in Eq. 2-2. The effective particle size,  $d_e$ , can be found as Eq. 2-3 [55], where M was the lens magnification (0.16 on average for these experiments).

$$d_s = 2.44(1 + M)f_{\#}\lambda \quad (2-2)$$

$$d_e = (M^2 d_p^2 + d_s^2)^{0.5} \quad (2-3)$$

In these experiments the diffraction limited spot-size dominated ( $d_e \approx d_s$ ) and was calculated by Eqs. 2-2 and 2-3 as  $4.3 \mu\text{m}$ , approximately 1/3 the size of a pixel ( $12 \mu\text{m}$ ). The low lens  $f/\#$  of 2.8 could not be avoided as to allow enough light to the sensors, while actual PIV images showed particle sizes generally on the order of 1-2 pixels.

The PIV acquisition required relatively dense seeding to obtain effective light intensity with the time-resolved system, and to allow for the desired 16 by 16 pixels IA's. In one set of experiments the seed issued from a 3.81 cm diameter tube creating the necessarily dense seeding, although the seed volume was found that it could sway partially in the wake cameras FOV. In a later experiment, a seed disperser was created (30.5 cm by 30.5 cm) with patterned exit ports spaced throughout PVC tube framing to

improve the dispersion (Figure 2-2B). The disperser created more uniform and still dense enough seeding over a larger volume.

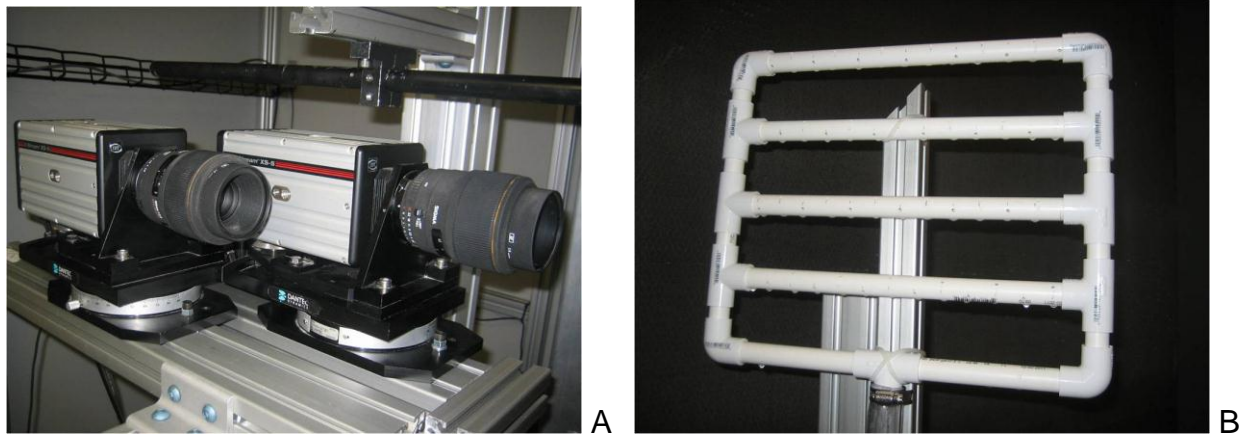


Figure 2-2. PIV dual camera setup and seed disperser. A) High-speed PIV cameras oriented in 2D fashion, camera 1 is focused over the membrane/model, while camera 2 is focused on the near-wake. B) Seed disperser for larger volume of more uniform seeding.

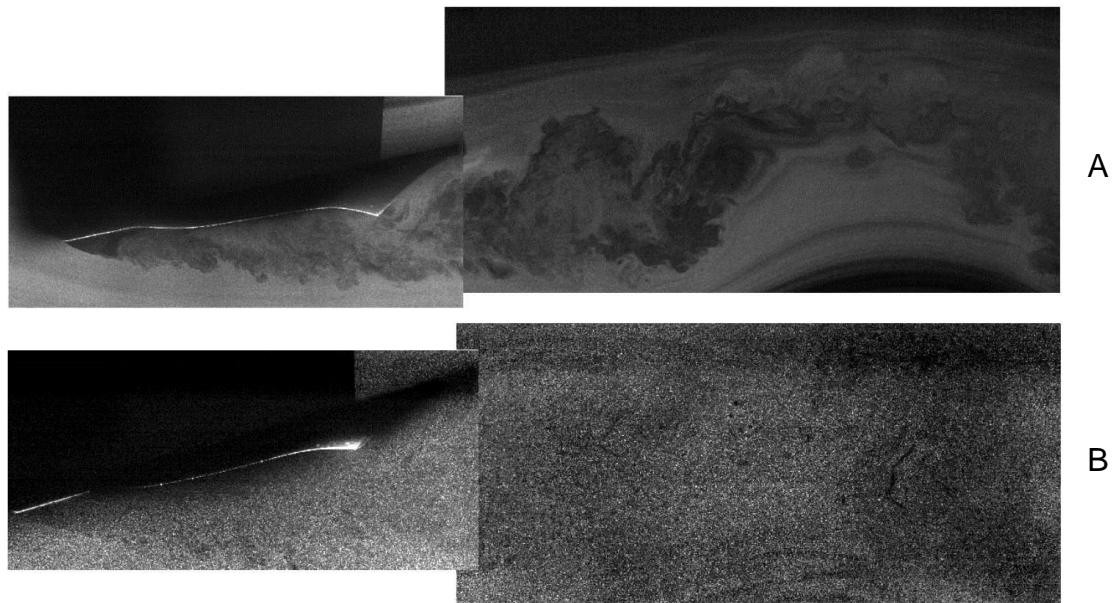


Figure 2-3. PIV images showing combined FOV's: membrane/model camera and wake camera. A) 1.3 $\epsilon$  model (inverted) at 12° aoa, denser seed. B) 2.8 $\epsilon$  model (inverted) at 16° aoa, dispersed seed.

## **Stereo DIC System and Processing Details**

The method of Digital Image Correlation was used to capture the 3D membrane deformation measurements. The DIC system was provided by *Correlated Solutions* and consisted of cameras and computer software to acquire and process images. Images were acquired by two *VisionResearch* high-speed Phantom v7.1 SR-CMOS cameras, which were oriented in stereo fashion each focusing on the same FOV from opposing angles. The Phantom cameras had a maximum frame rate of 4800 Hz at the full resolution of 800 pixels x 600 pixels and were equipped with *Tamron* aspherical 28-300 mm f-length macro lenses set to *f/#* 5.6. The *Correlated Solutions'* Vic-3D 2006 software, along with Vic-Snap and Phantom Camera Control v675.2 were used to acquire images, calibrate, and process.

## **Procedure and lighting**

Stereo calibrations were performed by taking ~100 images of a spatial calibration target of known dimensions while it was rotated, translated, and maneuvered in the field of view. The calibration images were processed with the Vic-3D software to discover the triangulation parameters needed such that three-dimensional membrane displacements could be resolved.

To perform the DIC, a small amount of paint was used to create a random speckle pattern on the membrane surfaces of interest (Figure 2-4B). Light reflected from the speckled patterns is ultimately used for gray-scale correlation analysis and therefore, proper lighting was an important aspect of obtaining DIC data. For these experiments, a high-powered (250W) halogen light was shown onto the membrane surfaces to provide sufficient reflection back to the camera sensors. During testing, the *aoa* of the models were changed, which would also affect how light was reflected. Therefore, the cameras

were refocused and recalibrated as was necessary to obtain reliable data for desired aoa sweeps. Figure 2-4A provides a view of the system as used for independent DIC tests in the ACF.

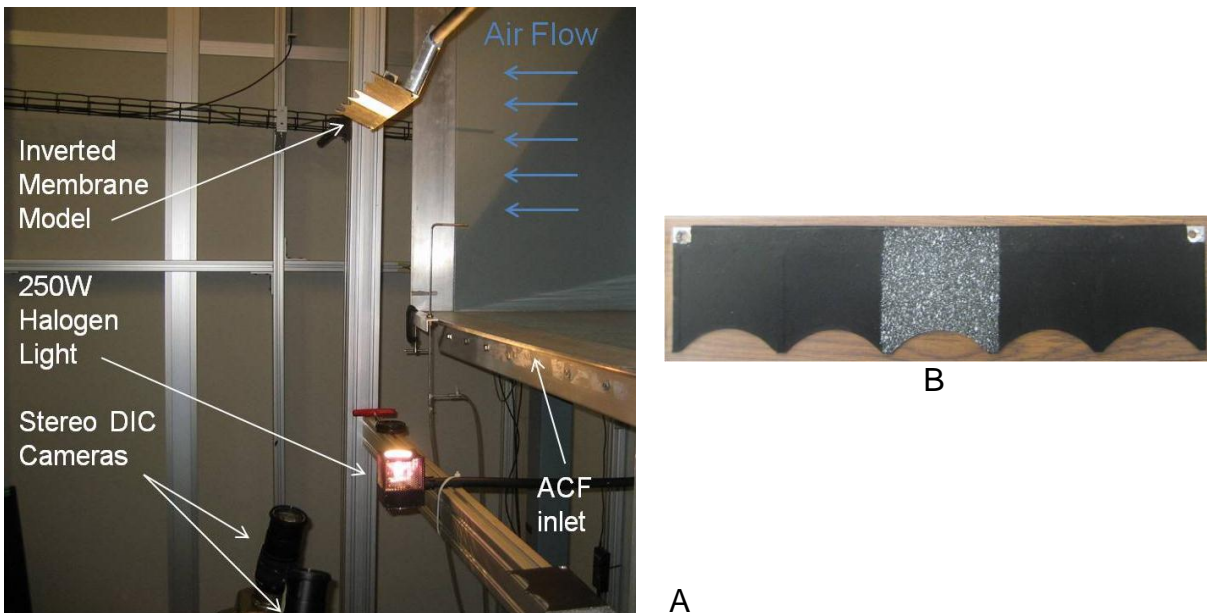


Figure 2-4. Installed DIC system and speckled model. A) DIC system in ACF.  
B) Random speckle pattern on model center cell.

### DIC processing

The algorithm involved grey-scale cross correlation analysis between images of the deformed membrane taken at a high frame rate while it vibrated in the flow, to a reference image acquired for each test case (aoa), when the membrane was motionless. Sub-pixel accuracy was achieved through cubic B-spline interpolation, while normalized sum of squared differences (NSSD) correlation criterion was used for its insensitivity to scales in lighting. The membrane region was divided into subsets of 25 by 25 pixels and a 5 pixel step size was used during processing. Using the full camera resolution to focus on just the membrane cell of interest (center cell), the spatial resolution in x and z (stream and spanwise directions, Figure 2-5) of the data was 0.64

mm between data points. In the deformation direction,  $y$ , membrane displacement calculations were accurate to  $\pm 0.1$  mm based on static displacement tests.

Membrane displacements were calculated normal to a reference plane, which was automatically generated by the software, passing through the geometric center of the membrane based on the reference image. If the membrane sagged (for the low tension model) then this reference plane might have been created at some small angle to the solid framing surface. In these cases, post-processing techniques were implemented to set the reference plane parallel with and flush to the model surface to correct small deviations. Once the reference plane was set flush, computed displacements were then normal to the model surface. As an independent system altogether, data generated from the DIC system did not inherently fit the PIV reference frame for combined plotting. However, knowledge of where the DIC membrane data began as  $x$  location, the model angle of attack, and a 2D rotation matrix were used to rotate and translate the DIC membrane data into the correct position for combined plotting in the PIV reference frame, as in Figure 2-5.

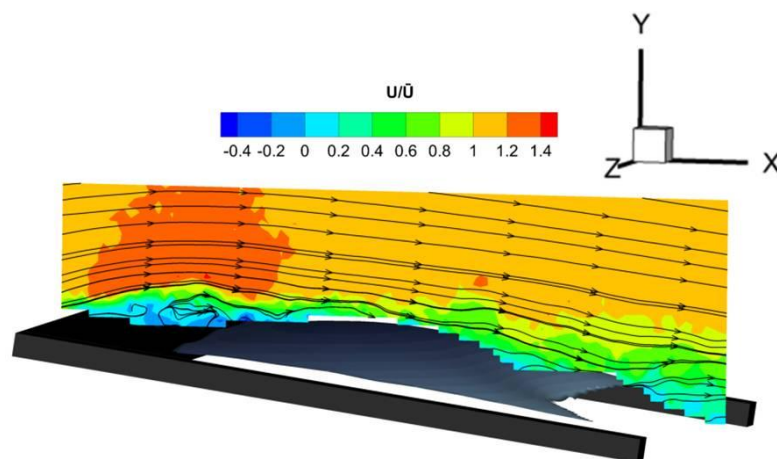


Figure 2-5. Cartesian coordinate system used with both PIV and DIC data results.

## Synchronization of PIV and DIC Systems

One major goal of this research project was to successfully acquire PIV and DIC data synchronously, which would allow for a better understanding of the time-dependent nature of the FSI. A sophisticated timing box controlled the complex timing of the PIV system, which included all the necessary triggers to successfully charge and fire the double cavity laser in tune with the double-frame imaging. For these reasons, the pulses generated were very short and weak, while the Phantom (DIC) cameras required a 5V square pulse to trigger and ideally would only fire on the first frame of the PIV imaging. It was discovered that the sync-out of the PIV cameras triggered only on the first image frame and as a 3V short spike. To synchronize the timing, this PIV sync-out signal was sent through a Tektronix type-114 pulse Generator which was set to reshape the signal into the 5V square wave that would fire the DIC cameras with negligible time delay. This method was implemented with success to obtain synchronous PIV and DIC data for an  $\alpha$ -sweep with one of the membrane models, and comparisons of the membrane positions from the laser plane showed good relation between the two systems, as discussed below.

One obstacle to overcome with the synchronized acquisition was the interference that the light from the PIV laser caused on the DIC measurements. The reflection of intense laser light would be captured by the DIC images and essentially cause large gaps in the membrane DIC calculated displacements (Figure 2-6C). To eliminate this interference, HOYA multi-coated (HMC) high-pass optical filters (wavelength >600 nm) were fitted on the DIC camera lenses. The filters allowed 90% or better transmittance of light greater than 640 nm in wavelength and zero transmittance of the 532 nm

wavelength laser light (Figure 2-6A,B). The synchronized setup of both systems in the ACF is depicted in Figure 2-7.

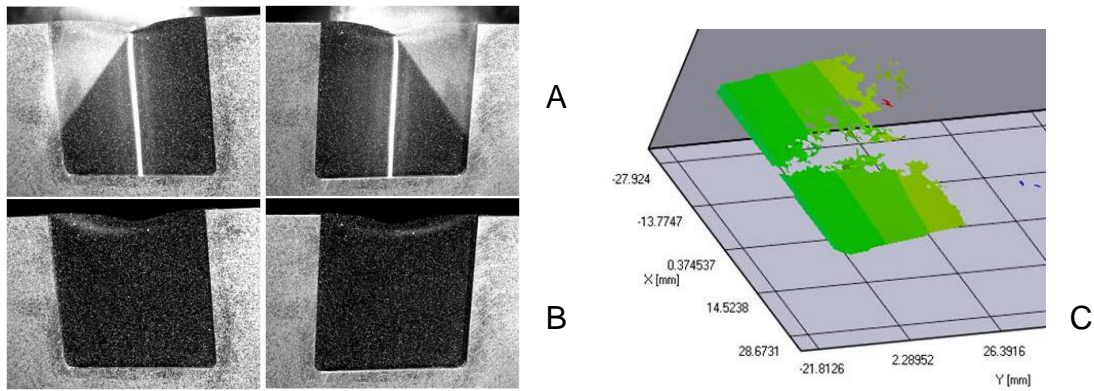


Figure 2-6. DIC images and PIV laser interference. A) DIC images synced with PIV, no optical filters. B) DIC images synced with PIV, with optical filters. C) Processed DIC data with laser interference.

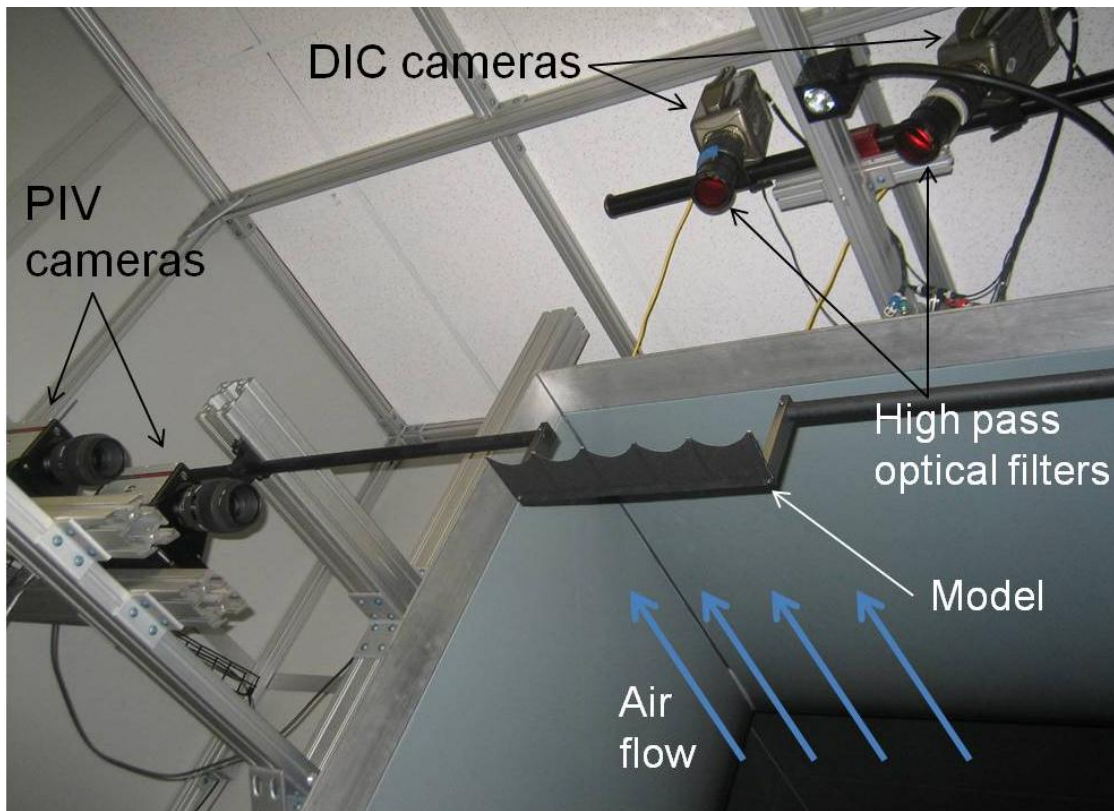


Figure 2-7. TR-PIV & DIC systems with model installed for synchronized data acquisition in ACF test section.

## Membrane Models

As mentioned in the introduction, the membrane models used for this study were created with many characteristics found to be aerodynamically beneficial from an evolution of earlier studies [46], [49], [50]. As a baseline, a rectangular rigid flat-plate of equal dimensions was also examined.

The investigation involved three membrane wing models, each one with five scalloped silicone membrane cells. Each also had a different average spanwise pre-strain value (also pre-tension by model creation in valid Hooke's Law range), denoted by  $\epsilon$  (%), and pictured in Figure 2-8. One key component of these models was the material change from latex (previous works) to matte-black silicone. While both materials share similar (untensioned)  $\pi_1$  values ( $\sim 3.3$ ), the matte-black color minimized laser bloom, therefore was pertinent in obtaining PIV data near the membrane surface.

The models were all of similar geometry, symmetric about center span; each with a 20% of chord,  $c$ , solid leading edge and with five square membrane cell regions, 80% of  $c$  on a side. The membrane cells were scalloped to a depth,  $s$ , equal to 25% of the cell span,  $b'$ . The geometric dimensions can be seen in Figure 2-9 while the values are listed in Table 2-1.

The silicone material itself played an important role in the creation of these models. Silicone's high heat-resistance allowed for a unique pre-tensioning method. In this method the silicone was heated to specific temperatures on a hot-plate before the 7075-T6 aluminum frames were adhered directly on the plate. Due to the silicone's isotropic and large coefficient of thermal expansion, once cooled, the membranes contained a measurable spanwise pre-strain ( $\epsilon$ ). This repeatable method was developed and performed at the University of Florida MAV Lab and Abudaram et al.

provides further details [51]. The material properties of the silicone are listed in Table 2-2, while the model creation temperatures, pre-strain values, and aeroelastic parameters ( $\pi_2$ ) are tabulated in Table 2-3. The silicone sheets were also pretreated by heating and cooling to prevent hysteresis effects, and that the average pre-strain values were computed on the center cell by DIC upon model creation. Finally, the linear relation between creation temperature and calculated pre-strain is displayed in Figure 2-10, where the slope was found as 0.0214% strain per degree Celsius [ $\epsilon/^\circ\text{C}$ ].



Figure 2-8. BR Silicone membrane wing models with scalloped trailing edges. A) 80x80\_1.3 $\epsilon$ . B) 80x80\_2.8 $\epsilon$ . C) 80x80\_4.2 $\epsilon$ .

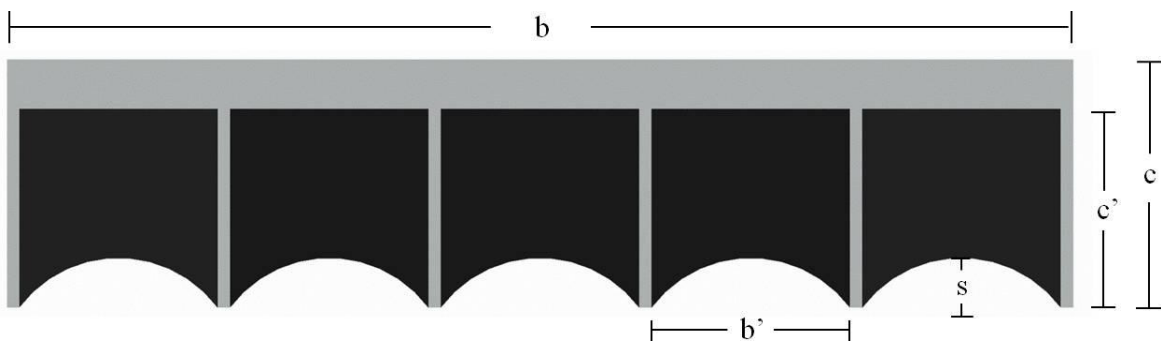


Figure 2-9. Model schematic with dimensions.

Table 2-1. Model dimension values.

Chord, c [mm]	Span, b [mm]	Cell chord/span c', b' [mm]	Aspect Ratio	Scallop Depth, s [mm]	Frame thickness, t, [mm]
76.8	327.7	61.4	4.27	15.4	2.8

Table 2-2. Silicone material properties.

Material	Thickness, $t_m$ [mm]	Durometer Hardness Test	Elastic Modulus, E [kPa]	Temp. Range [°C]	Tensile Strength [MPa]	Calculated Density, $\rho_m$ [kg/m <sup>3</sup> ]
Silicone Rubber	0.34±0.01	20A – soft	385	-62 to 218	5.52	1090±15%

Table 2-3. Membrane model properties.

Model Designation	Temperature of Creation [°C]	Measured average spanwise pre-strain, $\epsilon$ , [%] ± 0.1	$\Pi_2$
80x80_1.3 $\epsilon$	60	1.3	0.46
80x80_2.8 $\epsilon$	130	2.8	0.99
80x80_4.2 $\epsilon$	200	4.2	1.49

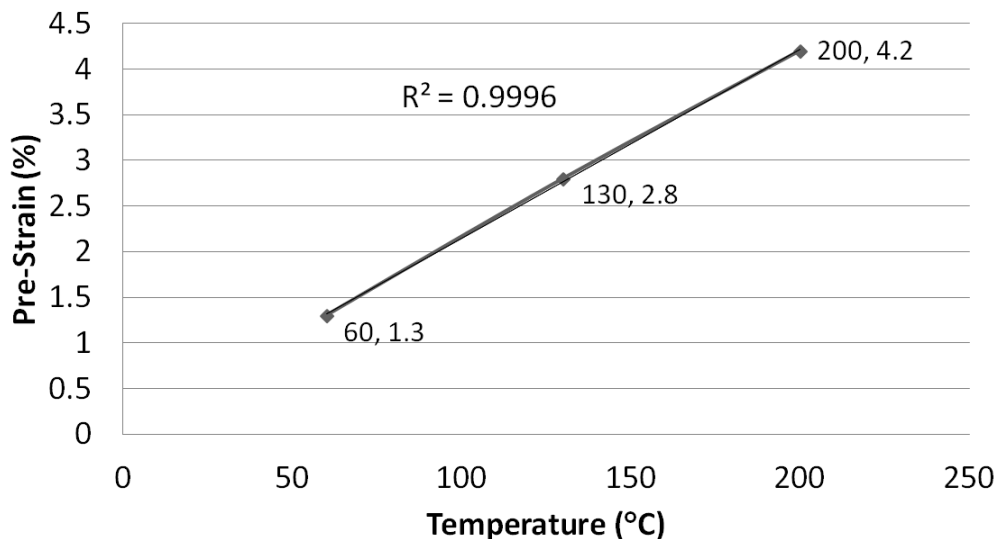


Figure 2-10. Measured pre-strain vs. creation temperature.

## Experiments Performed

Data obtained and analyzed for this study was gathered in several sets of experiments. A major contribution of study was the synchronous acquisition of DIC and PIV data, which was done successfully for an  $\alpha$ -sweep with the 80x80\_1.3 $\epsilon$  (low pre-tension) model. Additionally an experiment involving PIV of the rigid flat-plate baseline was performed at this time. Once models of higher pre-tension were obtained, independent DIC measurements were performed for all three models to compare vibration and pre-tension relationships. In a parallel study and with collaboration from the University of Alabama, force measurements for the varying pre-tension models were gathered, analyzed, and provided. Finally, PIV data was taken for a range of  $\alpha$  with the 80x80\_2.8 $\epsilon$  model utilizing improved seeding. In all tests the freestream velocity,  $U_\infty$ , was set at  $10 \pm 0.1$  m/s and angles of attack were set manually with a digital inclinometer to  $\alpha \pm 0.2^\circ$ . The Reynolds number, as defined in Eq. 2-4, based on model chord and freestream velocity was calculated as 52,660 (~50,000) and was fixed for all tests. Table 2-4 outlines the types of data acquired with each model.

$$Re_c = \frac{\rho_f U_\infty c}{\mu} \quad (2-4)$$

Table 2-4. Data types acquired for each model.

Model Designation	PIV obtained	DIC obtained	Synchronized
80x80_1.3 $\epsilon$ (low pre-tension)	x	x	x
80x80_2.8 $\epsilon$ (medium pre-tension)	x	x	
80x80_4.2 $\epsilon$ (high pre-tension)		x	
Rigid Plate (baseline)	x		

## Synchronized PIV and DIC Tests

Preliminary high-speed imagery showed that membrane vibrations were on the order of 50-100 Hz. It was decided to sample as fast as the PIV system allowed in order to not just minimize temporally aliasing the membrane motions, but also to provide identification of many membrane shapes, and to try and capture cause and effect events in the FSI. Therefore the sampling rate was set at 800 Hz by reducing the PIV cameras' resolution from 1280 by 1024 pixels (w x h) to 1280 by 600 pixels.

In these tests data were gathered for an  $\alpha$ -sweep of  $0^\circ$ ,  $4^\circ$ ,  $6^\circ$ ,  $8^\circ$ ,  $12^\circ$ ,  $16^\circ$ , and  $24^\circ$  aoa. For the largest angle of attack case of  $\alpha = 24^\circ$ , a larger shear layer existed and required larger camera fields of view; therefore full camera resolution was used adding to the height of view without further adjusting the camera calibrations or settings. However, this necessarily reduced the sampling rate to 450 Hz and lowered the maximum sample count to 814 samples based on camera memory.

As such, for  $\alpha < 24^\circ$ , 1024 samples were gathered for each case. The 1024 sample count was ideal for fast Fourier transforms (FFT's) to be utilized in calculating power spectral densities (PSD's) of velocity and membrane fluctuating signals. Also, convergence tests were performed and even the 814 sample count proved sufficient to converge first and second order velocity statistics to  $\pm 2\%$ , while for the majority of cases ( $\alpha < 24^\circ$ ) 1024 samples were used. An example of convergence of U-mean and Urms velocities from data of the 80x80\_1.3 $\epsilon$  model at  $\alpha = 12^\circ$  is provided in Figure 2-11.

A photograph of the wind tunnel setup for synchronized acquisition performed with the 80x80\_1.3 $\epsilon$  model is provided in Figure 2-12. For these tests, the model was inverted and centered in the ACF test section with the LE set approximately 0.3 m back from the inlet exit. The model inversion was necessary to capture PIV data over the top

membrane surface due to the PIV laser probe being constrained to issue from below the test section. The stereo DIC system was therefore placed above the test

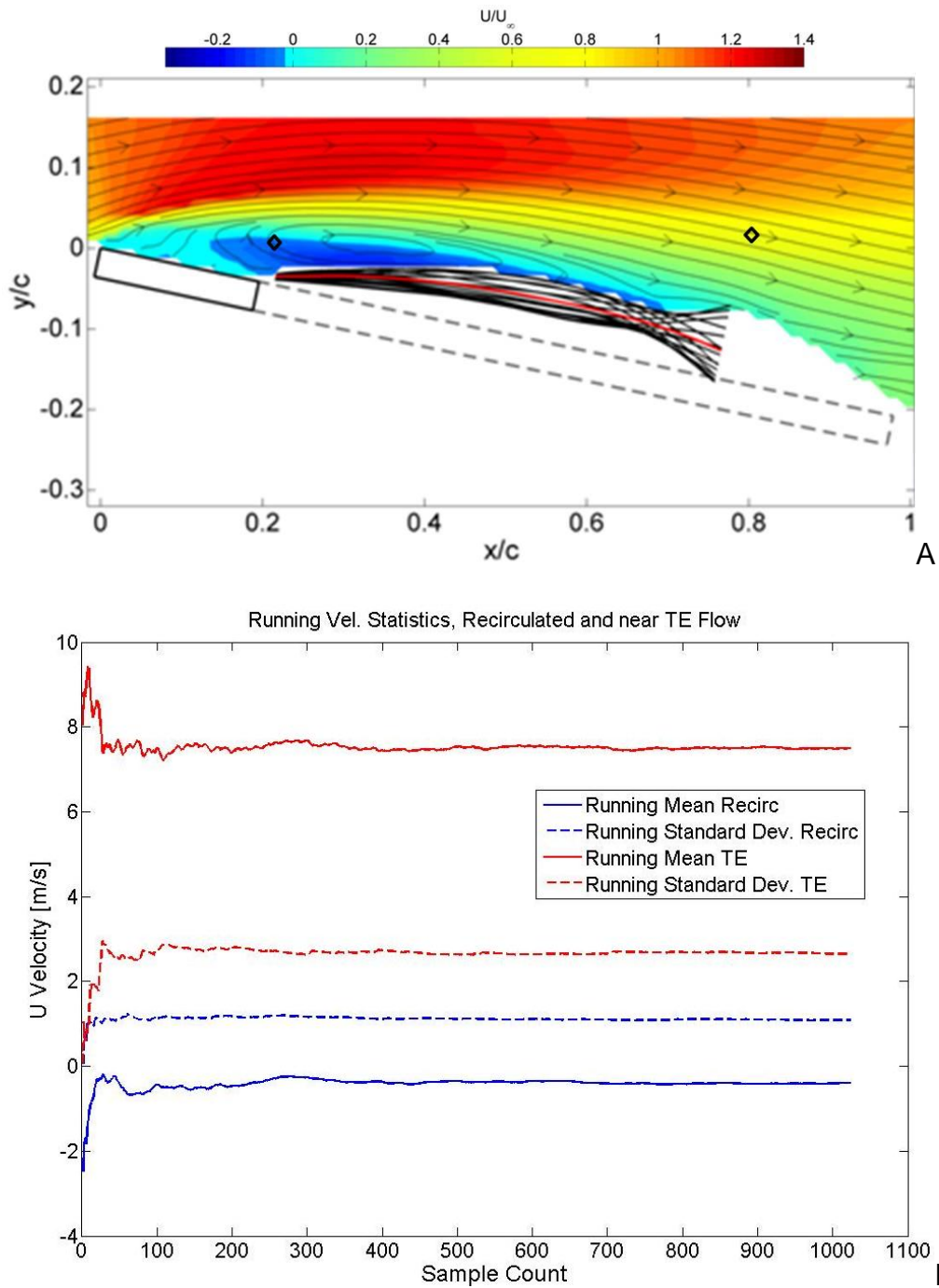


Figure 2-11. Convergence of PIV statistics vs. sample count. A) 80x80\_1.3ε at 12° aoa, u-component mean flow contours, diamonds indicate tested convergence location. B) Running U-mean and Urms for recirculated and near TE flow.

section to focus down at the model's lower surface center membrane cell, speckled for these tests. In these and other tests, DIC was obtained only for the central membrane cell, while 2D PIV was obtained at the model center span. These regions are portrayed on the model schematic in orange and green outline, respectively (Figure 2-12).

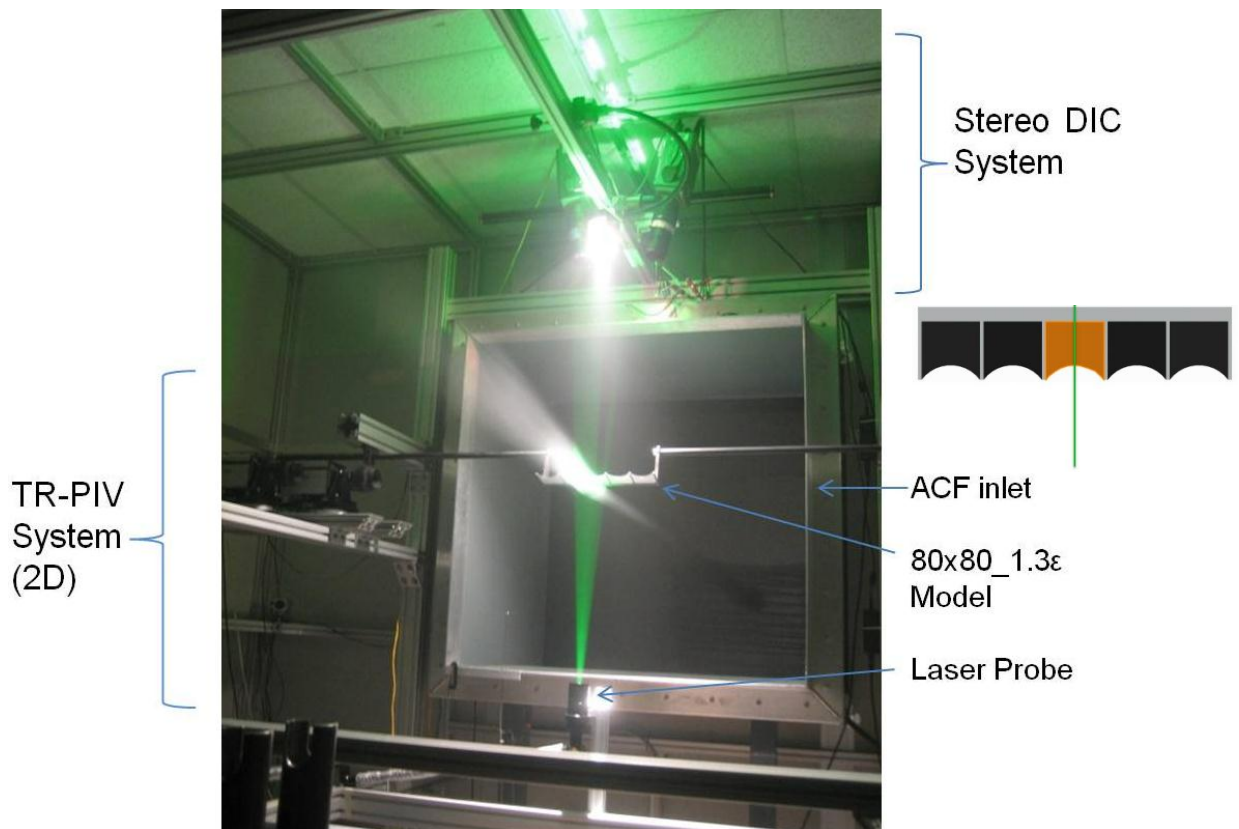


Figure 2-12. Synchronous acquisition of PIV and DIC data; schematic highlighting where data was obtained.

### Independent DIC Measurements

To compare frequency and vibration details between the membrane models of varying pre-tension, a set of tests were conducted where only DIC measurements were acquired. In these tests the models were installed (inverted) in the ACF in similar fashion to the combined acquisition. However, the DIC cameras were set up on a tripod below the test section for easier access (Figure 2-4A). Therefore in these tests, the top

surface was speckled for the central membrane cell (region of interest). The  $\alpha$ -sweep for these tests was expanded from the synched tests to include  $10^\circ$  and  $30^\circ$ . This meant the low pre-tension model was tested with again to obtain these missing angles. The total sweep was therefore:  $\alpha = 0^\circ, 4^\circ, 6^\circ, 8^\circ, 10^\circ, 12^\circ, 16^\circ, 24^\circ,$  and  $30^\circ$ . At each aoa, 1600 samples were gathered at 800 Hz. At this time, rectangular standoff mounts were replaced with symmetric airfoil mounts to help minimize structural vibration and any aerodynamic interference, as depicted below in Figure 2-13.



Figure 2-13. Symmetric airfoil standoff mounts with 80x80\_2.8 $\epsilon$  model.

### **PIV Measurements of 80x80\_2.8 $\epsilon$ Wing**

A final set of PIV tests were performed with the medium pre-tension model (80x80\_2.8 $\epsilon$ ). The selection of this level of pre-tension was based on force data that had been obtained and analyzed in collaboration with UA on identical membrane wings, discussed in Zhang et al. [56]. Among the findings, it was seen that the lowest pre-tension model was most aerodynamically efficient, while the medium pre-tension model was found least efficient as L/D. Each produced about equal lift, more than that of the baseline plate and particularly at higher aoa. Drag was found to be larger for the

membrane wings but L/D was comparable (at higher lift values) than the baseline. As such, PIV data was acquired for the medium pre-tension model to compare with the low pre-tension and baseline wings. Similarly for these tests, 800 Hz was chosen for the sampling rate, used to gather two sets of 1024 samples at each aoa. The same field of view constraint applied at high aoa, so two sets of 814 samples were obtained at 450 Hz for  $\alpha = 24^\circ$ . The aoa's tested in this set of experiments were  $0^\circ$ ,  $4^\circ$ ,  $8^\circ$ ,  $12^\circ$ ,  $16^\circ$ , and  $24^\circ$ . Additionally, this set of experiments utilized the aerodynamic mounts and the revised seed disperser previously described (Figures [2-13](#), [2-2B](#)).

### **Post Processing/Analysis**

Additional methods were utilized to improve the PIV velocity fields including vector validation, dynamic image masking, and outlier rejection. Vector validation was provided by the Dynamic Studio software and checked for very large or backward facing velocity gradients when comparing each vector to neighbors in a 3x3 kernel [[57](#)]. If a spurious vector was detected it was replaced with a local median vector. A dynamic masking algorithm was created to improve flow statistics and deal with complex membrane shapes such that instantaneous PIV snapshots could be studied. After the dynamic masks is applied, mean and fluctuating flow statistics are only presented outside of the regions where vibrations occurred to ensure conditional flow statistics are not presented. Typically 160 convection times are averaged over and approximately 70 membrane vibration cycles, depending on vibration frequency.

### **Dynamic Masking Algorithm**

One challenge of performing PIV with the repeated membrane cell wings was that both the in-PIV-plane membrane (center cell), as well as out-of-plane membranes (side cells), could vibrate significantly in the field of view of the model camera. This would

create a constantly changing region where PIV data was invalid. Therefore, the 2<sup>nd</sup> frame of each sampled image was analyzed to create a dynamic mask, and then applied to the instantaneous PIV vector fields. The masks were created by first using Sobel edge detection [58] to track bright pixels (laser reflection) indicating the surface of the in-plane membrane. After some spatial filtering to remove bright pixels associated with seed particles, a high order polynomial was fitted those remaining, which fit intricate membrane shapes. From the fitted polynomial, a geometric mask could be generated 'below' the 2D projected membrane surface and the curve was stored as a 2D membrane outline.

This outline was used to check for good correspondence with DIC calculated displacements of the center span (PIV plane) membrane shapes, once the DIC data was properly placed in the PIV reference frame. The average absolute difference between DIC generated membrane shapes and the pixel-line generated shapes was computed across all cases as 0.091 mm (0.12%  $c$ , 27%  $t_m$ ), and the average root-mean-square difference was computed as 0.122 mm (0.16%  $c$ , 36%  $t_m$ ).

Figure 2-14 shows examples of how instantaneous DIC calculated membrane shapes from the center span compared with the bright-pixel generated line. Note that there was roughly a 2 mm border around membrane edges where DIC deformation data could not be calculated due to the lack of necessary subset overlap during processing. Also the bright pixel tracking method had limitations, unable to accurately track the membrane when it deflected below the model surface or when there were large gaps in between bright pixels. The DIC computations were deemed much more reliable and are used for subsequent analysis.

To mask when an out-of-plane membrane was deflected up, causing a shadow or dark region, images were convolved with a 7x7 mean filter to smooth light gradients, then significantly dark regions were detected by an Ostu gray-value threshold method [59] and masked. This method was also used to detect dark regions in the wake when the stream tube of dense seeding swayed in the camera FOV. Masking of wake data was not found necessary when the seed disperser was used. Some examples of the dynamic masking methods are portrayed in the [APPENDIX](#).

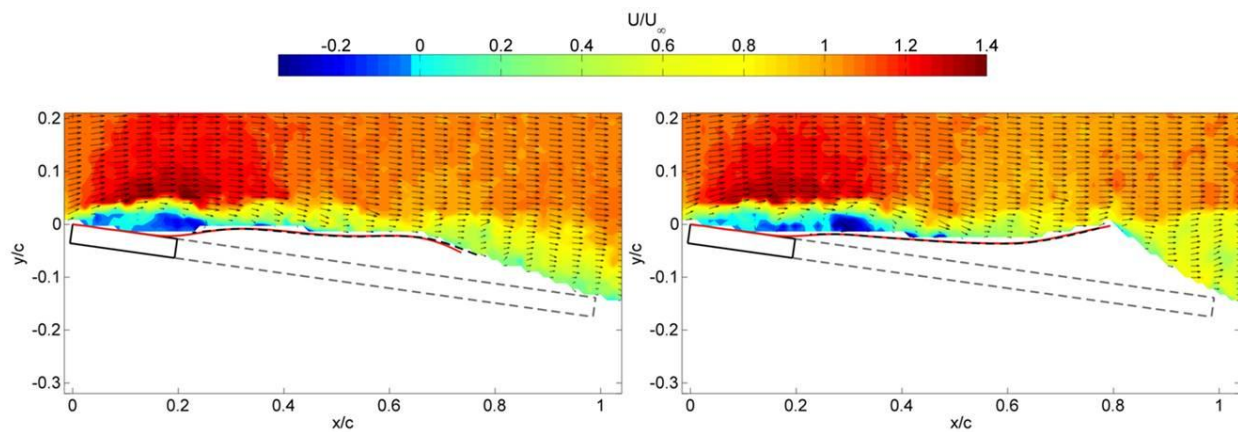


Figure 2-14. Combined instantaneous PIV and DIC at center span, compare DIC calculated (black dashed line) & bright-pixel generated (solid red line) membrane shapes.

## CHAPTER 3 RESULTS

In the following chapter the results supporting this investigation into the interactions between a membrane wing and the flow at moderately low Reynolds number will be demonstrated. Details of the flow field features, including time-averaged and fluctuating quantities will be analyzed. This will be followed by presentation and analysis of membrane oscillation characteristics and behaviors. Details and interpretation of the instantaneous FSI and how the combined flow and membrane behaviors interact, as well as correlations between the two will be presented and discussed in the final section.

### **Velocity Measurements**

Plots of the flow field results are shown throughout this thesis as normalized quantities and in the normalized spatial coordinate system:  $x/c$ ,  $y/c$ , and  $z/c$ . As reference,  $c$  is the full chord length and  $c = 76.8$  mm, while the freestream velocity,  $U_\infty$ , was 10 m/s. The measurement plane was set at  $z/c = 0$ . Model region and wake velocity data are combined for analysis of the mean flow fields and fluctuating velocities to see how they develop with changing incidence, as well as comparing the rigid baseline with the compliant membrane wings. Key flow traits are highlighted or expanded upon and some significant structural vibration attributes will be discussed as pertaining to flow behavior.

Along with the velocity contours, plots contain model geometry from the PIV plane, outlined in black. For membrane models, the out-of-plane batten portion is represented by a dashed line. Flow fields in this section are computed statistically over all membrane positions (>50 membrane cycles occurred per sampling set). To show the volume of

vibration, roughly one cycle of membrane oscillations is included as thin black lines. The time-averaged membrane position is indicated as a solid red line. From the chord length and freestream velocity, a typical convective time,  $\tau_c$ , is computed as 0.00768 s,  $\sim 130$  Hz. Thus, statistical flow quantities are computed over 160 convective times for  $\alpha < 24^\circ$  and due to the sampling alterations when  $\alpha = 24^\circ$ , closer to 230 convective times passed.

### **Time-Averaged Velocity Fields**

Analysis of the mean streamwise velocity ( $U_{\text{mean}}$ ) revealed insight into how compliant membrane surfaces included in planforms can manipulate the flow at low Re to possible aerodynamic benefit. Seen in the overall flow characteristics is a shift in behavior from low angle of attack ( $\alpha \leq 8^\circ$ ) to high angle attack ( $\alpha \geq 12^\circ$ ), which occurs through  $\alpha = 12^\circ$ . Figures 3-1, 3-2, and 3-3 provide the mean flow fields with streamlines for RP, 1.3 $\epsilon$  membrane wing, and 2.8 $\epsilon$  membrane wing, respectively. In these plots, dark blue indicates reversed flow, orange represents near freestream velocity, while enhanced or accelerated flow regions are contoured in red. The discussion that follows will be split up into a section on low aoa and high aoa as they have a different behavior once the flow is massively separated.

### **Streamwise velocity at low aoa**

The baseline rigid plate (RP) shows the development of the leading-edge separation bubble caused by the sharp leading edge which growing to cover 85% of the plate by  $\alpha = 8^\circ$ . The reattachment point is defined as where  $(x/c)$  reversed flow begins on the plate surface, however since the measurements did not go all the way to the wall this is an approximation. Above the bubble is a thin shear layer and then an accelerated region, up to  $1.3U_\infty$ , as flow curves around the recirculation area. The low

momentum oncoming flow cannot withstand the sharp turning and shearing at the LE. The recirculation zone existing on top of the model will adversely affect lift generation if the pressure is high. Comparing the membrane wings at  $\alpha = 8^\circ$ , there seems to be an interaction of the developing recirculation with the membrane motions that greatly reduces the size of the bubble on average and contains it mostly forward of the membrane. Additionally, streamlines show a tighter curvature above the shortened bubble and contours show higher flow acceleration, up to  $1.4U_\infty$ , occurring nearer to the model surface. The  $2.8\varepsilon$  model particularly shows these effects.

Another important aspect to study is how the near wake of the models compares, since drag can typically be related to steady wake momentum deficit for incompressible flows as in Panton [60]. It can be seen that the membrane wings have a broader wake deficit ( $\pm y/c$ ), caused by the membrane oscillations, while the wake seems narrower for the medium tension  $2.8\varepsilon$  model, with tighter vibration volume. However, the RP seems to cause larger wake velocity deficits. The membrane models allowed fluid to pass from under the membrane as it oscillates, adding momentum to the wake.

In Figure 3-4 velocity slices from each model at  $x/c = 0.2, 1.4$  locations for  $\alpha = 4^\circ$  and  $8^\circ$  more precisely compare the flows in these regions. For  $\alpha = 4^\circ$ , the plots show very similar velocity around the LE ( $x/c = 0.2$ ), while the RP shows a stronger but narrower wake deficit. At  $\alpha = 8^\circ$ , reduced recirculation, greater velocity increase, and  $\sim 1.5$  mm thinning of the shear layer height by the membrane wings at  $x/c = 0.2$  can be seen. From the near wake location ( $x/c = 1.4$ ),  $\alpha = 8^\circ$  the RP has a wake deficit of  $0.5U_\infty$ , much greater than the membrane models, followed next by the  $1.3\varepsilon$  model at

0.76  $U_\infty$  and then the  $2.8\varepsilon$  at  $0.81U_\infty$ , while the full wakes are not captured (Figure 3-4B).

Force data showed that L/D max occurs in the low  $\alpha$  range ( $4-8^\circ$ ) with membrane wings showing higher efficiency by as much as 26% [56], however, by flow analysis at low aoa, the  $2.8\varepsilon$  model appears to show the most beneficial mean flow, which is in contrast to the force data showing low tension ( $1.3\varepsilon$ ) with best L/D. Instantaneous flow analysis revealed a rush of velocity from under the membrane with each cycle which acts to keep the mean wake flow higher and will be discussed in a later section.

### **Streamwise velocity at high aoa**

Contours of  $U_{\text{mean}}$  at high angle of attack show the membrane wings resisting flow separation and recirculation. For the baseline RP at  $\alpha = 12^\circ$ , the recirculation bubble extends past the TE of the model and bursts into wake, which is in stark contrast to the mean flow of the membrane wings, which remain attached at  $12^\circ$  due to the extension of the membrane. This evidence of the rigid flat-plate separating at the center span location between  $8$  and  $12^\circ$  coincides well with many load studies for flat-plates at low Re, where a shift in the  $Cl_\alpha$  slope to a lower value occurs near  $10^\circ$  (separation bubble breaches TE) [18], [50], [56], [61]. After  $12^\circ$ , the baseline is seen with massive separation for increasing incidence with recirculated flow extending 1.5 and 2.1 chord lengths into the wake at  $16^\circ$  and  $24^\circ$ , respectively (Figure 3-1). This is in contrast with the membrane wings showing much less recirculation as well as greater velocities in the accelerated flow regions. There is also a greater downward bending of the wake flow at  $\alpha = 24^\circ$  for the membrane wings (Figures 3-2, 3-3), which may be linked to lift generation from a momentum balance point of view. This is backed up by force data showing  $Cl_{\text{max}}$  near  $\alpha=25^\circ$  and  $\sim 22-25\%$  improvement in  $C_l$  with comparable L/D

between membrane wings and the baseline here. Interestingly, there are some similarities in the mean flow streamlines and recirculation patterns very near the TE, as well as vibration shapes comparing the low tension ( $1.3\varepsilon$ ) at  $24^\circ$  to that of the medium tension ( $2.8\varepsilon$ ) at  $16^\circ$ , possibly indicating similar average tension between these cases.

High aoa velocity slices are provided in Figure 3-5 comparing at  $x/c = 0.3, 1.4$  locations. The slices for  $x/c = 0.3$  show that the membrane wings continue to develop greater accelerated velocities and less recirculation in the forward part of the model, also slightly thinning the shear layer as indicated by steeper velocity gradient. More prominent are the wake differences and development of reversed flow,  $-0.3U_\infty$  for the RP at  $x/c = 1.4$ , whereas the wake never reverses for the membrane wings at this location. In addition to suffering a greater deficit, the RP wake is seen to become as broad or broader than the wake of the membrane wings which differs from low aoa. These conditions would imply that the membrane wings show increasing benefit at higher aoa, which was confirmed by the force data [56]. While the flows of the membrane wings are generally very comparable to each other, velocity slices at high aoa also predict that the  $2.8\varepsilon$  medium pre-tension model should perform best aerodynamically for this  $Re$ , contrasting with the force data.

There are steady and unsteady membrane behaviors that lead to the more favorable time-averaged flows. In brief, the membranes are seen to distend into a time-averaged camber shape, allowing the flow to more easily negotiate turning over the wing. This 'camber' also passively adapts its shape for varying dynamic pressure at different angles of attack. Additionally, the TE vibrations allow jets of air to pass from

under the membrane and interact with the low momentum shear layer. This causes enhanced turbulent mixing and momentum transfer, discussed in the next sections.

### Root-Mean-Square Velocity Fluctuations

A Reynolds decomposition is applied to the flow fields:  $\tilde{U} = \bar{U} + u'$  and  $\tilde{V} = \bar{V} + v'$ , where  $\tilde{U}$  is the instantaneous streamwise velocity component,  $\bar{U}$  is the mean and  $u'$  is the deviation, same for vertical components. Utilizing the  $U_{rms}$ ,  $V_{rms}$  nomenclature for the square root of the mean-squared velocity fluctuations of U and V components, i.e.,  $U_{rms} = \sqrt{\langle u'^2 \rangle}$  and  $V_{rms} = \sqrt{\langle v'^2 \rangle}$ , the statistical fluctuating flow fields are discussed.  $U_{rms}$  and  $V_{rms}$  are the resolvable (from this data) components of the turbulent kinetic energy (TKE) existing in the flow fields. Insight into where the flow turbulent energy resides is important to gain a better understanding of flows over low Re wings and to investigate what influence or affect the membrane planforms create. This is particularly true since flow over low Re wings are highly unsteady and have demonstrated rapid transition to turbulence [15].

### Streamwise velocity fluctuations

Figure 3-6 compares normalized  $U_{rms}$  contours at low  $\alpha$ ,  $\alpha \leq 8^\circ$ , for the three tested models. At very low incidences the membrane wings are seen having an impact on the near wake causing slightly larger  $U_{rms}$  values than the baseline and causing a *letter V* shape spreading into the wake. The baseline at  $\alpha = 6$  and  $8^\circ$  shows growing  $U_{rms}$  over top of the model, which is attributed to the developing and growing shear layer emanating from the LE. For the membrane wings the shear layer appears to impinge on and interact with the membrane vibrations for this  $\alpha$ -range. It may be significant that force data showed the membrane wings had maximum L/D in this range.

The motions of the membranes will, by no penetration condition (viscous interactions), necessarily impart v momentum to the unsteady shear layer, often reported as shear layer excitement in various studies [5], [44]. Discussed in the next section on membrane behavior, over this  $\alpha$ -range the vibration frequency is increasing with  $\alpha$ , possibly connected to shear layer interactions. The tighter vibration pattern of the  $2.8\epsilon$  wing appears to reduce the area of turbulent influence on the wake compared with the  $1.3\epsilon$  wing, while magnitudes are similar.

In Figure 3-7, high angle of attack Urms contours are presented for comparison. At  $\alpha = 12^\circ$  it can be seen that the membrane wings begin to show a strong influence on the topside shear layer, with it being pulled close to the TE fluctuations. The baseline RP at  $12^\circ$  has begun to separate and shows its shear layer lifting away from the surface and intensifying in the wake. As incidence is increased further to  $\alpha = 16^\circ$  and  $24^\circ$  the RP shows a regular pattern of larger, more intense, and further away shear layer development from both the leading and trailing edges, as the flow separates over the model and transitions to turbulence in the wake.

In contrast, the membranes show a change in behavior where a region of high Urms begins to build just downstream of the membrane TE. This phenomenon has some tension dependency, with higher magnitudes generated, as large as  $0.5U_\infty$ , by the medium pre-tension model. The patterns of Urms are very similar between  $1.3\epsilon$  and  $2.8\epsilon$  overall and more a function of angle of attack than vibration amplitude or shape.

The enhanced Urms near the membrane wings is representative of the flow's steady kinetic energy supply ( $\sim 0.5\rho U_\infty^2$ ) being partially converted to turbulent kinetic energy (Urms), in part through work of the membrane motions. This occurs much more

for the membrane wings than for the rigid baseline. The membrane oscillations may therefore absorb turbulent energy present in gusty flight conditions, dissipating it as vibrations like a damper for the dynamic system. This adds stability to the low Re flyer in a turbulent environment.

### **Vertical velocity fluctuations**

The vertical fluctuations,  $V_{rms}$ , are also considered. In Figure 3-8, plots of normalized  $V_{rms}$  are shown for low  $\alpha$ . There is less  $V_{rms}$  occurring in the shear layer at low angle of attack than  $U_{rms}$  across all models. Compare for example,  $\alpha = 8^\circ$ , where  $U_{rms}$  values of 0.27 were common among models, while  $V_{rms}$  peaks around 0.17 in this case. Albeit smaller in magnitude, the models all show very similar behavior for  $V_{rms}$  at these low  $\alpha$  cases compared with  $U_{rms}$ . The vertical fluctuations in this  $\alpha$ -range associated with the attached shear layer, growing in size for the RP with  $\alpha$  and impinging on the membrane and spreading in the wake for compliant wing models.

Investigating the higher  $\alpha$  cases, plotted in Figure 3-9, unique  $V_{rms}$  behavior is seen. At  $\alpha = 12^\circ$ , the aforementioned behavior shift is realized. For the RP, the TE is seen to cause a shear layer from the flow passing under model and bending up into the wake, a stronger  $V_{rms}$  exists here than  $U_{rms}$ . This may be associated with the bent reversed mean flow caused by the separation bubble bursting into the wake (Figure 3-1) and affecting flow passing from below the model in a more direct way, acceleration from around the TE can be seen in the  $U_{mean}$  contours. The membrane models appear to have very similar  $V_{rms}$  to each other at  $12^\circ$ , broader for the  $1.3\epsilon$  wing, and increased by 10% in intensity from  $\alpha = 8^\circ$ .

For the RP at  $16^\circ$  the lower shear layer still shows the peak of vertical fluctuations, but the overall separation and shear layer created at the LE and rising from the model is

evident as from Urms. At 24°, the wake of the rigid plate is near equal in turbulence intensity, U and V components ( $\sim 0.3$  to  $0.35U_\infty$ ), far from the model.

The membrane wings show very unique behavior with high angle of attack. At 16° aoa, Vrms is around  $0.28U_\infty$  and fairly evenly distributed in the bulk of the wake (more compact and slightly higher magnitude for  $2.8\epsilon$  wing). When  $\alpha = 24^\circ$ , there is a very large spike in the Vrms, where it jumps in magnitude to  $0.49U_\infty$  for  $1.3\epsilon$  and  $0.53U_\infty$  for  $2.8\epsilon$ . This occurs over a much larger region than the peak in Urms and also centered slightly further downstream, at  $x/c = 1.3$ , not 1.1. The oblong shape of heavy vertical influence is also seen extending farther into the wake, beyond a full chord length from the model TE ( $x/c > 2.2$ ), while the Urms peak extended about 0.7 chord lengths from the batten TE. Since the shape and pattern is very similar between membrane wings, it is deemed a function of angle of attack over vibration frequency (equivalent for each model at 16 and 24°, to be discussed in following section) or amplitude, but there is some tension dependence, as the medium tension wing shows a trend of increased magnitude for Urms and Vrms. This is an indication that the membrane presence, either through altering the pressure, viscous interaction, or both, is causing the flow which has no original V component to deviate in  $\pm y$  by 50% of the freestream. This is a significant transfer of unsteady momentum occurring in the near wake and is an indication of the complex influence the membrane imparts on the flow, while also being excited by it.

### **Reynolds Shear Stress**

Defining the Reynolds Averaged Navier-Stokes (RANS) equation as Eq. 3-1 (Eq. 4.21 from Pope [62]), it is seen that there is an apparent stress term on the right hand side composed of the deviation velocity squared tensor:  $-\rho\langle u'_i u'_j \rangle$ . This is the Reynolds

Shear Stress (RSS), which acts on the flow in balance with the pressure and viscous forces. For highly unsteady flows such as the ones of this study, the RSS can be a significant term governing flow behavior and is associated with turbulent momentum transfer.

$$\rho \frac{\overline{D}\langle U_j \rangle}{\overline{D}t} = \frac{\partial}{\partial x_i} \left[ \mu \left( \frac{\partial \langle U_i \rangle}{\partial x_j} + \frac{\partial \langle U_j \rangle}{\partial x_i} \right) - \langle p \rangle \delta_{ij} - \rho \langle u'_i u'_j \rangle \right] \quad (3-1)$$

From the data in this research, the resolvable term of the RSS tensor, with density dropped (incompressible), is:  $-\langle u'v' \rangle$ , note the negative sign (-) is retained in this definition. Therefore it is noted that when  $u'$  and  $v'$  deviate of the same sign on average, the defined RSS will be negative, and when  $u'$ ,  $v'$  deviate oppositely on average, the RSS at that point will be positive. A quick reference for the discussion of contours:

Same Sign Deviations (-) | Opposite Sign Deviations (+)

First focusing on the RSS development and behavior at low aoa as shown in Figure 3-10, it is evident that the RP begins to generate momentum transfer of opposite sign deviations, or positive RSS, in the shear layer sitting above the model. At the same time, the LE and TE begin to cause same sign deviations as negative RSS. The membrane wings show very similar behavior between them, and at  $\alpha \leq 6^\circ$ , the wake shows somewhat symmetric (about the axis passing through the model aoa) positive and negative RSS, the sign most likely associated with positive and negative  $v'$  values depending on if the membrane is influencing flow above or below it. At  $\alpha = 8^\circ$ , there is stronger RSS developed by the RP, while the membranes influence is heavier in the wake. The wider volume of membrane oscillation for the 1.3ε membrane wing causes a larger wake influence than that of the 2.8ε wing.

Regarding the RSS developed at higher aoa, as seen in Figure 3-11, the interesting case of  $\alpha = 12^\circ$  again highlights the impact the membrane wings have when the plate has just shifted to separated flow in this plane. Membrane motions interacting with the low momentum shear layer were shown in previous sections. What the RSS shows is a largely positive region over the TE fluctuations for this case. This is momentum transference from U to V through the  $u'$  and  $v'$  opposite sign fluctuations at any given point in the flow (on average) where (+) RSS appears. Since the  $v'$  fluctuations should be associated with the membrane motions up and down ( $\pm y$ ) by viscous interaction, it is seen that the membrane oscillations impart a v component to further away, higher momentum fluid and bring it to mix with the low u-momentum fluid passing near the surface. The added momentum helps resist separation in an adverse pressure gradient, if present.

The RP at  $12^\circ$  shows the continued development of a pattern of positive RSS over the top of the model and negative RSS from around the TE. Most likely both regions are very similar in nature and associated with random deviations pertaining to shearing and the development of turbulence. This pattern remains the same at  $\alpha = 16$  and  $24^\circ$ , only more intensified and pushed further into the wake.

From the membrane's RSS's at  $16^\circ$ , the  $1.3\varepsilon$  wing and  $2.8\varepsilon$  wing show the new development of positive RSS from directly behind the membrane TE, now equal in magnitude to the positive RSS above it, which is different from  $12^\circ$ . In this case, there is an apparent dependence on vibration amplitude, as the lower tension model has larger RSS regions in the wake of similar pattern to the medium tension, both pulling the momentum flux close to membrane TE.

Finally at  $\alpha = 24^\circ$  for the membrane wings, there is significantly different behavior and complex RSS patterns generated by them, similar between the two. A relatively large region of approximately double the magnitude from all previous cases, negative RSS ( $\sim -0.12$ ) develops downstream of the tightly vibrating TE. Above that, a strong positive RSS is seen. The interactions near to the TE are also stronger than for other cases and a tightly packed pattern of positive, negative, positive alternating RSS near the TE indicates flow structures being developed there, to be shown in the section on FSI. Instantaneous analysis of the deviation velocities showed the same sign fluctuations producing the strong (-) RSS, as jets of air passing over and under the membrane caused deviations of up and forward ( $+v'$  and  $+u'$ ) or down and reversed ( $-v'$  and  $-u'$ ), in tune with vibrations.

The shape of the region comes from  $v'$  fluctuations convecting straight back in the stream direction and  $u'$  fluctuations tending to convect back along the axis through the model angle of attack. Fourier analysis showed the deviations occurring at the membrane oscillation frequency and will be discussed further in the following section. Overall, the enhanced momentum transport generated by the membrane wings and pulled in to the TE is a sign of increased work and energy transference between the flow and model through membrane interactions. While similar patterns were found amongst the membrane wings, there was stronger RSS generated by the medium tension wing, as with the  $U_{rms}$  and  $V_{rms}$  turbulence components.

### **Membrane Oscillation Behavior**

Time-resolved DIC measurements allowed for in-depth analysis of the membrane dynamics across all three pre-tensions, bringing the  $4.2\epsilon$  high tension wing into the discussion. As discussed in the introduction, the membrane motions are a combined

effect of dynamic pressure forces, tensions restoring forces, and inertial forces associated with the mass which may include gravitational effects. The ‘stiffness’ of the membrane is computed as the product of Young’s modulus,  $E$ , and the membrane thickness,  $t_m$ , giving units of N/m, to compare with bending stiffness  $E \cdot I$  for 3D structures (units of  $N \cdot m^2$ ). For the silicone material used,  $E$  was calculated from DIC of load tests as 385 kPa [51] and  $t_m$  was measured as  $0.34 \pm 0.01$  mm. Therefore,  $E \cdot t_m$  is found as 130.9 N/m. Modeling the membrane behavior as a simple dynamic system, the natural frequency (Hz) should be estimated as in Eq. 3-2, a property of the proportionality constant,  $K$ , and the mass.  $K$  has the units of N/m and will be considered as the ‘stiffness’,  $K = E t_m$ ,  $K = 130.9$  N/m. Introducing the scalloped chord length,  $c_s$ ,  $c_s = 0.6c = 46.1$  mm. Mass can be estimated as  $c_s \cdot b' \cdot t_m \cdot \rho_m$ , which gives  $m \approx 0.001$  kg.

$$f_n = \frac{1}{2\pi} \sqrt{\frac{K}{m}} \quad (3-2)$$

Finally, computing the natural frequency from Eq. 3-2 it is found as  $\sim 57.6$  Hz. Using Hooke’s linear relation and including pre-tension in the  $K$  term gives  $K = 132.6$ ,  $134.6$ , and  $136.4$ , respectively for  $1.3\varepsilon$ ,  $2.8\varepsilon$ , and  $4.2\varepsilon$ . The natural frequency estimations are then 58.0, 58.4, and 58.8 Hz (Table 3-1). These estimations do not account for nonlinearities, system complexity, or damping and will be compared with actual vibration frequencies obtained during experiments.

### Full-Field Mean and RMS Properties

The full-field membrane displacements are time-averaged to find the mean shapes and fluctuations are quantified by the root-mean-square technique. These values are normalized by the chord,  $c$ . In Figure 3-12, contours of mean membrane displacements for each membrane wing are shown for  $\alpha = 8^\circ$ ,  $12^\circ$ . Note that the  $1.3\varepsilon$  data from

synchronized PIV-DIC tests was obtained from lower membrane surface, so a 2mm border of membrane edges is missing, whereas portions of the solid frame were included during independent DIC tests to capture the entire cell and more easily orient the data. Both acquisition methods showed very agreeable data with no noticeable differences. Some of the common membrane trends are noticeable, such as that there is a clear reliance on pre-tension for maximum mean distention, with lower tension allowing larger distention. Also, each membrane shows that the time-averaged position is maximal near the membrane geometric centers. Finally, it can be seen that high angle of attack will increase the mean displacement. These trends were found to hold across all angles of attack. In Figure 3-13, for the same  $\alpha$ 's (8, 12°), contours of the normalized RMS displacements are shown, as  $y/c$ , are shown. From these plots it is shown that the TE has the largest fluctuation behavior, and that there is typically nodal behavior between the geometric center (midpoint) and the TE. The shape of the RMS comes from the primary vibration behavior as a wave of distention that emanates from near the membrane LE and travels to the free TE growing in amplitude, which repeats nearly periodically with unsteady driving (pressure) forces, and therefore possibly a limit cycle oscillation as discussed by Johnston et. al [47], [48]. However, the behavior becomes less periodic under higher tensions and for high  $\alpha$ . There are less clear overall trends for RMS, with each pre-tension showing unique angle's of attack of maximum TE vibration. Spanwise waves were not apparent in the RMS behavior. Figure 3-14 provides an indication of where much of the following analysis occurs with each pre-tension, i.e., the Mid Point at the geometric center ( $z/c = 0, x/c = 0$ ), the Side

Point near one side and at  $x/c = 0$ , and the TE Point at  $z/c = 0$  and near the membrane TE. Note that the Mid Point and TE Point lie in the PIV laser plane.

### **Pointwise mean and rms properties**

To better understand the mean and RMS properties of the membranes across all tested  $\alpha$ 's, and with knowledge of the roughly uniform (symmetric spanwise) deformation characteristics, much information can be learned from the Mid Point and the TE Point. Figure 3-15 gives the mean deformations with RMS plotted as bars of the Mid Points for the full  $\alpha$ -sweep. In this manner it can be seen that the lower tension will always distend further on average and shows larger RMS at low angle of attack. The average distention increases vs.  $\alpha$  with larger gradient from  $\alpha = 0$  to  $12^\circ$  than after that point, even though average dynamic pressure force is linear with angle of attack by frontal area  $\propto c \cdot \sin(\alpha)$ . This implies that the average membrane position is a function of the flow state (separation) and average pressure felt.

A similar plot is shown for the TE points vs.  $\alpha$ , each pre-tension in Figure 3-16. Although each pre-tensions shows unique behavior, from the RMS fluctuations, it is clear that at lower  $\alpha$  the fluctuations are much higher before a behavior shift when the fluctuations steady out around  $\alpha = 16^\circ$ . This coincides well with when the flow was found to impinge with the membrane more directly through attached shear layer, discussed in the previous section. At  $24^\circ$   $\alpha$ , the low and medium pre-tension ( $1.3\epsilon$ ,  $2.8\epsilon$ ) wings show some excitement (RMS) but the highest tension does not, possibly already having reached a material limit being under high average force (pressure + tension). By  $\alpha = 30^\circ$ , all the models show very little RMS behavior and the same trend of larger average displacement for lower tension. There is the apparent shift in RMS after separation conditions at  $12^\circ$ , where the membrane becomes much steadier.

Each wing shows a different angle where TE fluctuations are greatest, with the trend of higher  $\alpha$  for higher tension. That is the  $1.3\varepsilon$  wing RMS peaked at  $4^\circ$ , the  $2.8\varepsilon$  at  $8^\circ$ , and the  $4.2\varepsilon$  at  $10^\circ$ , while a link of this showing possible aerodynamic benefit could not be created from the force data. The maximum statistical displacement achieved through mean or fluctuation was for the  $1.3\varepsilon$  wing, at  $0.068 y/c$  or  $\sim 5.2\text{mm}$ , while up to  $10\text{ mm}$  was seen in instantaneous positions.

### **Time-averaged camber effect**

As noticed in the previous flow section, the membranes exhibit a steady effect of a time-averaged cambered shape. Since a true camber is fixed by the relation of the rigid airfoil shape it cannot adapt for changing flow conditions or  $\alpha$ . The membrane mean shape, however, adapts to changing pressure condition. Figure 3-17 shows how the membrane produces a camber as the difference in mean displacements at the Mid and TE points, for the low and high pre-tension cases. In the plot, dashed lines represent the mean TE Point positions at each  $\alpha$ , while the mean Mid Point positions are in solid lines. The difference between the Mid and TE points estimates the time-averaged camber and it can be seen that it exists for both the high and low pre-tension models across the full  $\alpha$ -range. The phenomena is particularly shown for low pre-tension at  $\alpha < 16^\circ$ ,  $\sim 2.4$  times that of the high pre-tension model in this range. The low tension model also showed max L/D (among all models) from the force data at  $\alpha = 6^\circ$ , where the effect is most prominent. This implies a possible connection between this steady effect and average aerodynamic loads.

### **Membrane Frequency Content**

The membrane deviation displacements denoted as  $m'$  here, where by similar decomposition from the previous section,  $\tilde{M} = \bar{M} + m'$ , are used to compute spectra by

FFT or discrete Fourier transforms (DFT). The finite-range Fourier transform defined as Eq. 3-3 (Bendat and Piersol [63]), is used on signals of length  $N$ , where  $N=1024$  samples ( $1.3\varepsilon$  synched test),  $N = 814$  ( $\alpha = 24^\circ$ , synched), or  $N = 800$ , using two ensembles from 1600 sample sized independent DIC tests, incorporating DFTs. The bin width,  $\Delta f$ , is determined as  $\Delta f = 1/T$ , thereby for  $\alpha \leq 16^\circ$ ,  $\Delta f = 0.781 \text{ Hz}$  and for  $\alpha = 24^\circ$ ,  $\Delta f = 0.553 \text{ Hz}$ . This provided sufficient frequency resolution to identify peak frequencies in the membrane vibrations. Ultimately, the Welch method was utilized to compute one-sided Power Spectral Densities (PSD) as in Eq. 3-4 [63], using a rectangular window with 50% overlapping due to the nearly periodic behavior of the membrane cycle oscillations.

$$X(f, T) = \int_0^T x(t) e^{-j2\pi ft} dt \quad (3-3)$$

$$xx(f) = \frac{2}{T} E[|Xf, T|^2] \quad (3-4)$$

Computing the PSD at the Mid, Side, and TE Points indicated in Figure 3-14 revealed that the membranes showed a peak frequency at each angle of attack. Often, many harmonics were present as in the examples for  $1.3\varepsilon$  at  $\alpha = 8^\circ$  and  $2.8\varepsilon$  at  $\alpha = 24^\circ$  shown in Figure 3-18. These spectra curves are representative of other aoa cases for the low and medium pre-tension wings. The harmonics are due to the nearly periodic wave behavior and nonlinearities in the system, with the silicone material as a possible cause. It should also be noted that the Side Point showed the same frequency content as the Mid and TE Points, indication of minimal spanwise oscillation behavior, which was also not detected visually. The power of the spectra revealed that the TE > Mid >

Side, which was expected based on the RMS behavior and was found to be consistent across models and angle of attacks.

The high tension (4.2ε wing) showed a unique behavior at 16° aoa. Assumingly under higher average combined pressure and tension forces than other membranes here, the membrane hit an apparent resonance, where two modes were seen in the RMS plot and spectra showed a 90 Hz peak, much higher frequency than for all other cases (Figure 3-19A). Additionally, the spectra captured a change in oscillation behavior for this wing for  $\alpha > 16^\circ$ , post resonance. For these cases, spectra showed broad lower frequency peaks as dominant, with the wave frequency emerging as 2<sup>nd</sup> or 3<sup>rd</sup> peaks (Figure 3-19B,C), this more complex post resonance behavior was not seen for the lower tension models. The RMS plots for this wing at high aoa are shown in Figure 3-20.

From all the dominant peaks associated with the membranes' PSD's, the peak vibration frequencies are plotted vs. aoa in Figure 3-21. From the plot it is clear that higher pre-tension leads to higher vibration frequencies and that there is a dependence on angle of attack. The behavior is very similar up to  $\alpha = 12^\circ$ , with frequency increasing slowly at lowest  $\alpha$ , then quickly over 6-12°. After 12°, the low and medium tension models taper toward a limit of approximately 60 Hz, while the high tension model hit the resonance discussed previously at 16°. Then the dominant peaks were much lower (perhaps beating behavior), while the wave-nature was still noticed visibly, and showed similar planning out as lower tension models, stabling at ~89 Hz for high aoa. These frequency trends are very similar to those found by Tregidgo for perimeter-reinforced membranes [44].

As for comparing the estimated resonant frequencies to actual frequencies obtained, there is very reasonable agreement. Before the divergent behavior at higher  $\alpha$ , the average vibration frequencies by model ( $\alpha = 0$  to  $12^\circ$ ) are 51, 56, and 66 Hz, low, medium, high pre-tension, respectively, the overall average being 57.7 Hz. The estimated natural frequency for an untensioned baseline from Eq. 3-2 was found as 57.6 Hz, but this does not explain the differences for varying pre-tension and may be coincidence; however the correct approximate frequency range was predicted, without accounting for nonlinear or resonant effects. From averages over  $\alpha$ , it can be stated that increasing the pre-strain will increase the vibration frequency by approximately 5.5 or 6.9 Hz per % strain [Hz/ $\epsilon$ ], the difference being accounting for the apparent resonance or not.

### **Fluid Structure Interactions**

Utilizing the synchronized membrane and flow information for the  $1.3\epsilon$  membrane wing, further insight into the time-dependent fluid-structure interactions can be gained. From the time-averaged and statistical flow properties, there was particular evidence of interactions at the membrane TE for high angles of attack ( $\alpha \geq 12^\circ$ ). This will be investigated by analyzing time-dependent streamlines and vorticity. FFT's will also be performed on the time-resolved deviation velocity signals to show relevant flow frequencies and how they correspond with membrane oscillation frequencies. Finally, correlations between membrane and flow unsteady signals will be shown and discussed.

### **Trailing-Edge Vorticity Interaction**

Vorticity is formed by flow interacting with physical boundaries; therefore a significant interaction between the membrane and the flow will typically involve generation of

vorticity, a measure of rotation in the flow field. If vortices are created, they can advect in and affect surrounding flow, transferring momentum and energy. For this study, vorticity is calculated as defined in Eq. 3-5 [64], which is the component resolvable from the acquired 2D PIV data, and shows twice the ‘solid body’ rotation about the z-axis. As defined, negative vorticity spins clockwise (-) and positive vorticity spins counter-clockwise (+). Vorticity values are further normalized by  $c$  and  $U_\infty$  as defined in Eq. 3-6.

$$\vec{\omega}_z = \left( \frac{\partial v}{\partial x} - \frac{\partial u}{\partial y} \right) \quad (3-5)$$

$$\omega^* = \vec{\omega}_z \cdot \frac{c}{U_\infty} \quad (3-6)$$

The normalized instantaneous vorticity,  $\omega^*$ , is combined with instantaneous membrane positions and model geometry (of just the center cell) to analyze TE phenomena in Figures 3-22 to 3-25. Since membrane cycles were seen as not truly periodic, the convective time,  $\tau_c$ , defined previously as the transit time for a particle moving at the freestream velocity to travel the chord length ( $\tau_c = 0.00768$  s), is used to introduce a normalized time for use with the time-resolved data as  $\tau_n = t/\tau_c$ . The real time passed in the sequence is  $t$ . Information plotted is only a small sample in time but will represent what is seen to repeat often within the vibration cycles at each  $\alpha$ .

In Figure 3-22,  $\omega^*$  is plotted for a short time series for the model at  $\alpha = 8^\circ$ , in which the membrane begins maximally distended up and heads downward during its cycle. At this angle of attack, it is seen that there is no significant vorticity generated at the membrane TE as the flow protrudes up from under the membrane smoothly and joins the flow from over the top surface. However, there is strong vorticity generated by shearing at the LE (shear layer) present and it is seen impinging on the membrane in its up position and then allowed to advect over the surface somewhat as the membrane

moves down. It is not known whether vorticity interacting with the membrane at low aoa is associated with the increase in vibration frequency with aoa, found during this range.

Similar plots of  $\omega^*$  for  $\alpha = 12^\circ$  can be seen for consecutive samples of a time sequence in Figure 3-23. At this angle of attack the membrane is vibrating at its highest overall frequency for the  $1.3\varepsilon$  wing (62 Hz) and (+) opposite deviation RSS being generated near the membrane TE (Figure 3-11). In the current vorticity plots, at  $\tau_n = 0.000$  the membrane is passing down and the highly unsteady shear layer shows some larger vortex rollup over the membrane surface, similar to those discussed by Rojratsirikul et al. at similar Re with PR models [5], [40]. As the membrane decelerates at the bottom of its cycle, stops, and just begins to move up ( $\tau_n = 0.651, 0.814$ ), a rush of fluid from under the membrane shoots up and creates a counter-clockwise spinning vorticity (+) as it mixes with the unsteady fluid pulled down by the membrane, as well as the freestream fluid. This swirling structure pulls streamlines from higher momentum fluid farther above the membrane as it advects downstream, which helps keep the low momentum fluid from separating as easily. Even as the vortical structure has passed out of the frame ( $\tau_n = 1.302$ ), the influence of its presence is still seen in the bent streamlines around the trailing-edge.

For the next case of  $\alpha = 16^\circ$ ,  $\omega^*$  is plotted in Figure 3-24. In this series, at  $\tau_n = 0.000$ , the membrane is just about to reach the top of its cycle and briefly stop before accelerating back in the other direction. As soon as it begins its descending motion, the air rushing from under it ( $\tau_n = 0.163$ ) immediately interacts with the fluid pulled down by the TE and again a counter-clockwise vorticity structure forms ( $\tau_n = 0.326$ ). Possibly due to stronger pressure forces, the structure appears larger than for similar ones at  $12^\circ$  and

is seen interacting with the shear layer (negative vorticity) reaching back from the LE, protruding higher over the model surface than at lower aoa ( $\tau_n = 0.488$ ). A complex behavior that sends streamlines toward the descending membrane is seen ( $\tau_n = 0.651$  to  $0.977$ ). The membrane reaches the bottom of its cycle at  $\tau_n = 1.139$  and stream lines continue to pass down under the membrane influenced by its passage and the receding vorticity structure.

Addressing plots of  $\omega^*$  for  $\alpha = 24^\circ$  plotted in Figure 3-25, at  $\tau_n = 0.000$ , the membrane has just reached the bottom of its cycle and is about to pass upward. Recall that the sampling frequency for this case was 450 Hz so approximately 44% more time passes between frames. The flow is seen as very unsteady with a large shear layer and some reversed flow at  $\tau_n = 0.000$ . As the membrane TE begins to deflect up ( $\tau_n = 0.579$ ) a rush of fluid passes from under the membrane and initially into the recirculated flow as well as up into the shear layer. As soon as the membrane hits the top of its cycle and snaps back down again, the flow immediately rolls up as a counter-clockwise vortical structure ( $\tau_n = 0.868$ ). At  $\tau_n = 1.157$ , the structure has dispersed but persists and interacts with separated flow still influencing high momentum fluid to pull down into the unsteady region ( $\tau_n = 1.447$ ). It can be implied from the RSS plots of  $\alpha = 24^\circ$  in Figure 3-11, that the counter-clockwise vortical structures here are shed into the wake and intensify causing increased turbulent transport and hence the large negative RSS, as the bottom right side of the structure would be a positive  $u'$  and  $v'$  deviation and in the right location.

## **Flow and Membrane Coupled Behaviors**

Through much of the investigation, there is obvious evidence of the interactions and inter-dependence between the membrane and flow behaviors. Spectral analysis and correlations are employed to try and quantify how and where the flow and membrane interactions are most coupled.

### **Spectral analysis applied to flows**

In the same manner as described in the previous section with fluctuating membrane signals, velocity power spectra are used to find the dominant frequencies in the fluctuating flow. By investigating many locations throughout the flow fields, it is found that the membrane peak vibration frequency also emanates to the flow, giving it the same spectral peaks. In other words, the membrane oscillations are felt throughout the flow field as the dominant resolvable frequency content, even upstream of the membrane. There is a dependence of proximity, particularly to where the membrane fluctuations are high like at the TE, causing a more power in the PSD peak. Only within the recirculated region or near the LE in the shear layer were membrane frequencies sometimes not found, while in these cases, broadband spectra was seen, without peaks.

In Figure 3-26, an example is provided showing PSD's computed at indicated flow location from the 1.3 $\epsilon$  wing at  $\alpha = 8^\circ$  overlaid by the PSD of the membrane TE location at that angle of attack. The information here shows that at the flow locations,  $u'$  deviation signals share the same peak frequency of 52 Hz and even some of the harmonics associated with the membrane oscillations. Note also that the wake locations show larger power, this is because the magnitudes of the fluctuating velocity are greater in the wake. The overall trend seen for this model and aoa as well as others, is that the

TE frequency will be seen in the flow and that the power will generally be associated with proximity moving forward from the membrane TE or downstream from it; with wake locations showing stronger peaks dependent upon velocity deviations. With the power associated with the membrane frequency dominating by many orders other resolvable flow frequency content, it is interpreted that the membrane driving the flow around it and in the wake, though also initially excited by it.

### Correlation analysis

Correlations between the membrane and the flow are computed for specific locations on the membrane (center span PIV plane) with the entire fluctuating flow component variables for further insight. The correlations are calculated as linear correlation coefficient with zero time-lag, defined by Eq. 3-7. In this equation  $m'$  represents the fluctuating membrane displacements while  $u'$  represents the fluctuating velocity component i.e.,  $u'$  or  $v'$ . These correlations were computed with data from the  $1.3\epsilon$  wing synchronized acquisition sets.

$$\rho(\tau_0) = \frac{1}{N} \sum_{i=1}^N (m'_i u'_i) / (\sigma_{m'} \sigma_{u'}) \quad (3-7)$$

To check for the significance of the correlation values the Pearson's  $r$  correlation criterion is used. At 100 degrees of freedom (sample count) an  $r$  of 0.254, where  $r$  is defined the same as Eq. 3-7 above, can be considered significant at a level of 0.01. Considering that 1024 samples were used for these cases (1024 degrees of freedom) and that  $p$  values were seen often reaching  $\pm 0.8$  to 0.9, the correlations are considered very high and statistically significant with 99% confidence.

The positive and negative correlation values were seen to oscillate at the peak membrane frequency of whichever case was investigated. Figure 3-27 contains

contours of the correlation coefficient between  $m'$  fluctuations at the TE point of the membrane, indicated with a green diamond in the plots, with  $u'$  fluctuating velocity components for  $\alpha = 8, 12, 16^\circ$ . Figure 3-28 shows the same cases of  $\alpha = 8, 12, 16^\circ$  for  $m'$  fluctuations from at the TE correlated with  $v'$  deviation velocities. The TE location is chosen because of the power in the signal at this location and from the flow spectra's proximity power trend.

From the  $u'$  correlations, there is a clear dependence on  $\alpha$  for strength of correlation, which is most likely a function of the power (variance) or amplitude of the TE vibrations, which is seen diminishing with increasing  $\alpha$ . However, unique patterns are seen and notably strong negative correlations dominate near the TE Point, while the wake shows regions of positive and negative correlation. When the correlations are interpreted physically, it seems logical that the flow would decelerate locally, i.e., deviate below its mean value ( $-u'$ ) when the membrane TE distended above its mean value ( $+m'$ ), leading to the strong negative correlations. The positive region downstream could be flow that accelerated from a cambered shape (TE down) that has advected there from an earlier time, making it difficult to interpret. To this point, the full cross correlation function is plotted from one location ( $x/c = 0.8, y/c = 0.1, \alpha = 8^\circ$ ) to show how the locations' correlation values are oscillating (+) and (-) in time at the peak membrane frequency (while also advecting in space) and that the zero time-lag value may not be near the maximum (Figure 3-29).

The  $v'$  correlation contours show the opposite trend near the membrane TE. A large positive correlation region near and above the TE exists. Similar to  $u'$ , strength of correlation diminishes overall for higher  $\alpha$ . The wake is characterized with a more

uniform region of correlation as the flow shifts  $\pm$  in  $y$ . The large region of strong positive correlation at  $8^\circ$  is a sign of the flow locally accelerating up ( $+v'$ ) to navigate the distended up membrane TE ( $+m'$ ), a local  $V$  acceleration at the expense of  $U$  where correlation was negative. The oscillatory nature of the correlations from Figure 3-29, imply that the fluid in this region is pulled down ( $-v'$ ) at a later time when the membrane passes down. These correlations suggest that the membrane fluctuations are most significant at low  $\alpha$ , that there is a limit to the extent of influence upstream of the membrane, and that the whole flow fields (and wakes),  $U$ - and  $V$ -components are oscillating with the membrane peak frequency, a significant presence.

Table 3-1. Estimated proportionality constant and natural frequency.

Model pre-strain $\epsilon$	Estimated $K$ [N/m]	Estimated $f_n$ [Hz]
1.3 (%)	132.6	58.0
2.8 (%)	134.6	58.4
4.2 (%)	136.4	58.8

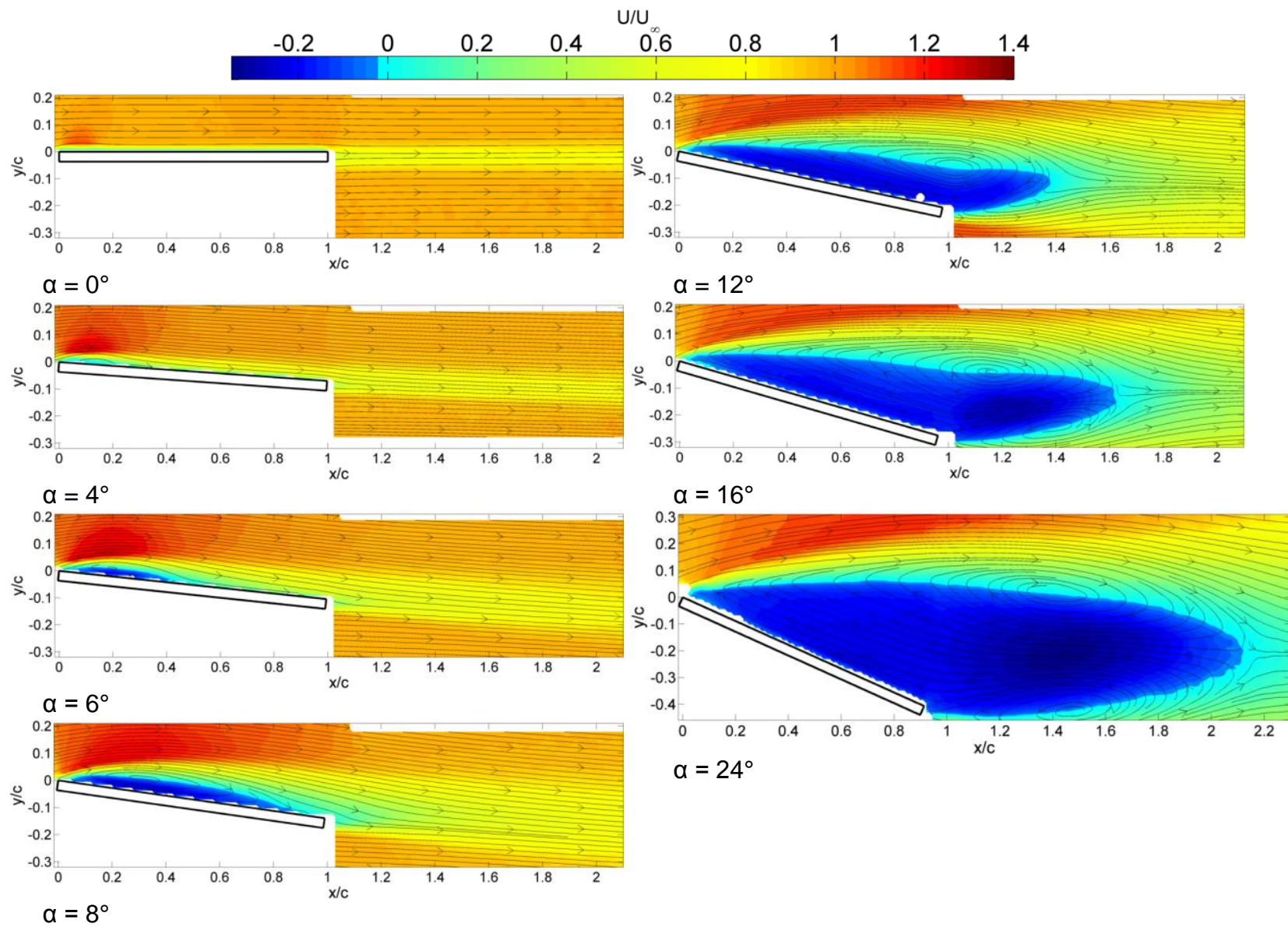


Figure 3-1.  $U_{\text{mean}}/U_{\infty}$  contours with streamlines for baseline rigid plate.

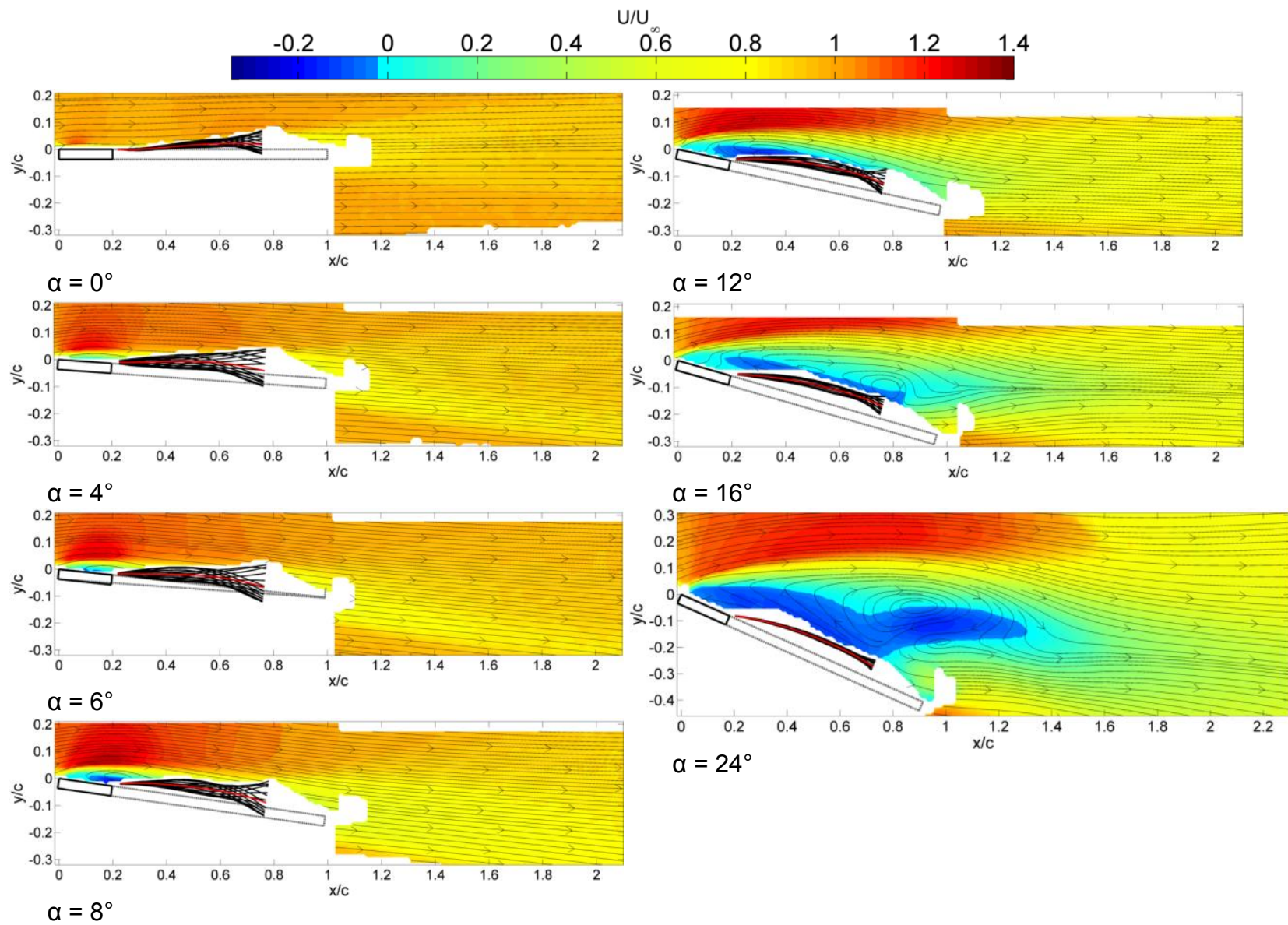


Figure 3-2.  $U_{\text{mean}}/U_{\infty}$  contours with streamlines for 1.3ε membrane wing.

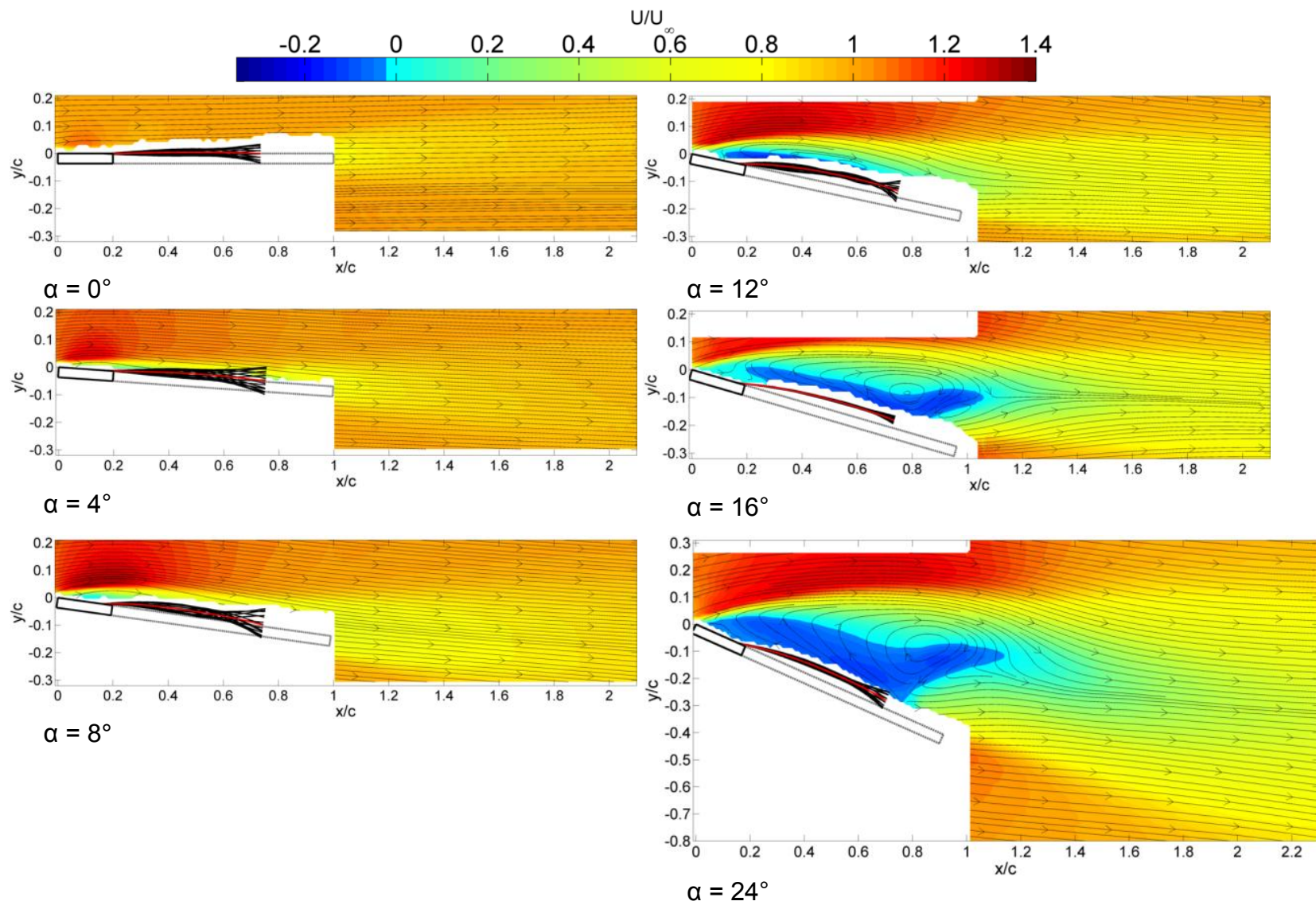


Figure 3-3.  $U_{mean}/U_\infty$  contours with streamlines for  $2.8\epsilon$  membrane wing.

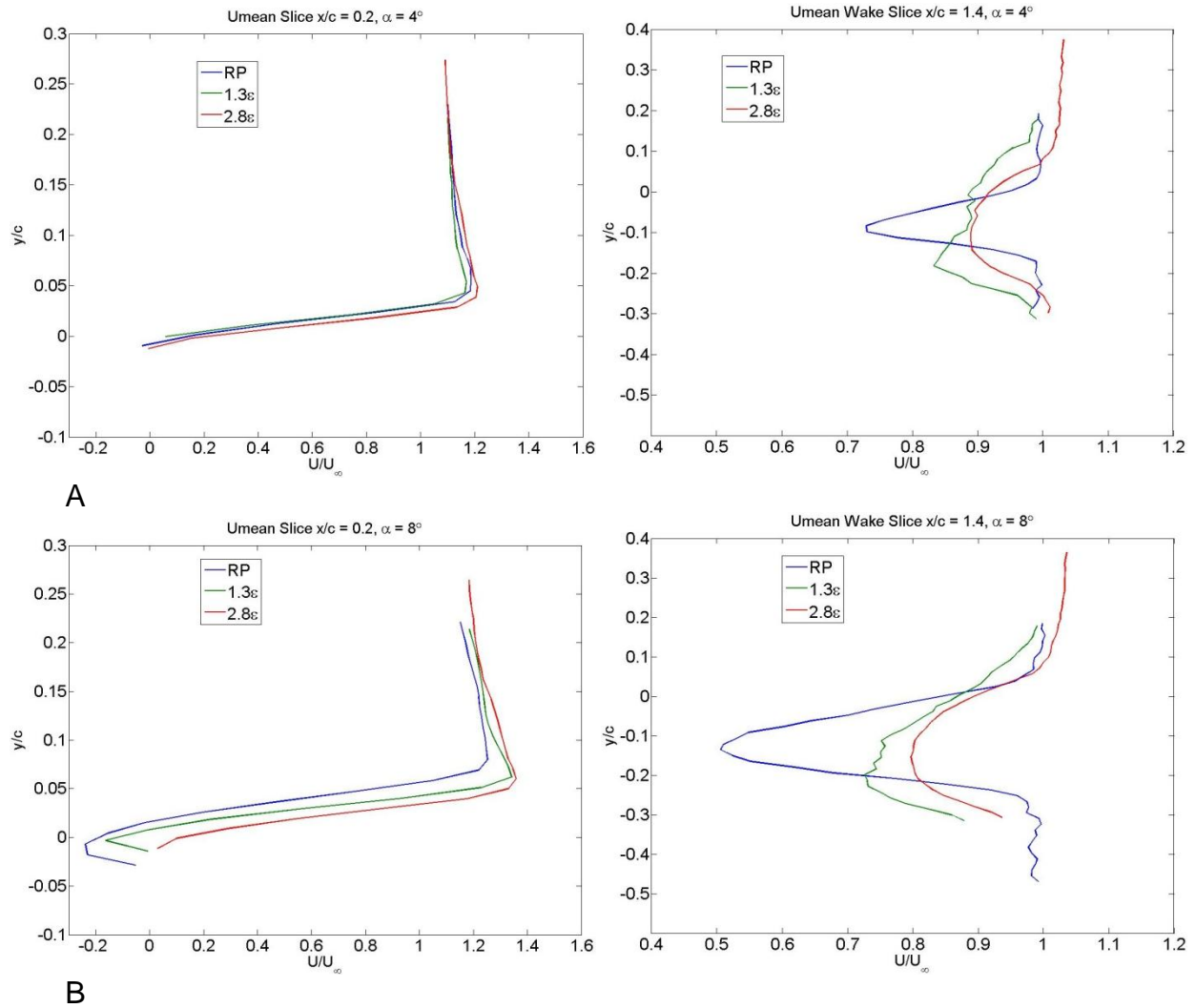


Figure 3-4. Umean/ $U_\infty$  slice plots at  $x/c = 0.2, 1.4$  for low aoa. RP in blue,  $1.3\varepsilon$  in green,  $2.8\varepsilon$  in red. A)  $\alpha = 4^\circ$ . B)  $\alpha = 8^\circ$ .

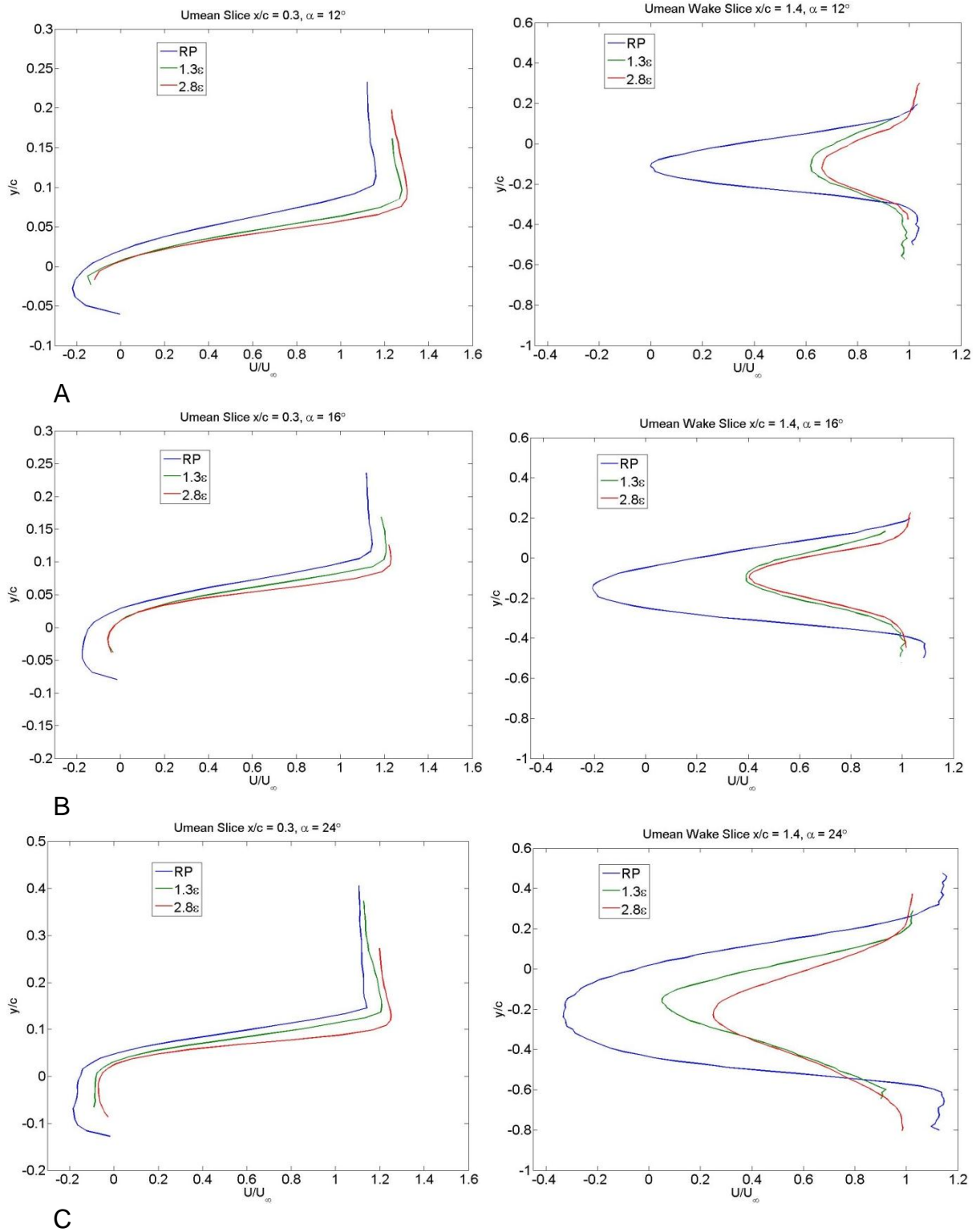


Figure 3-5. Umean/U $\infty$  slice plots at  $x/c = 0.3, 1.4$  for high aoa. RP in blue,  $1.3\varepsilon$  in green,  $2.8\varepsilon$  in red. A)  $\alpha = 12^\circ$ . B)  $\alpha = 16^\circ$ . C)  $\alpha = 24^\circ$ .

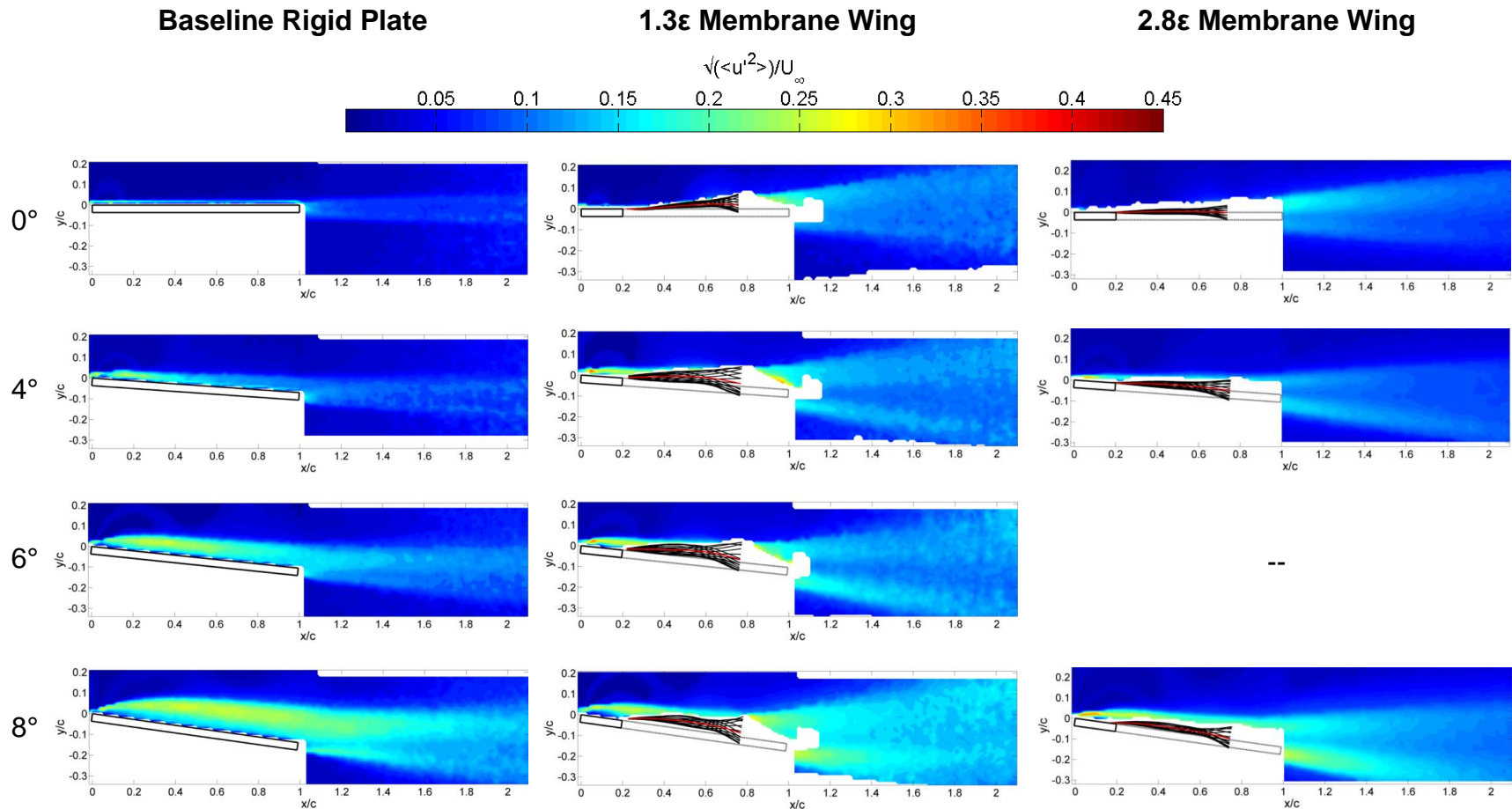


Figure 3-6.  $U_{rms}/U_\infty$  contours comparing baseline RP, 1.3 $\epsilon$  wing, and 2.8 $\epsilon$  wing at low  $\alpha$ .

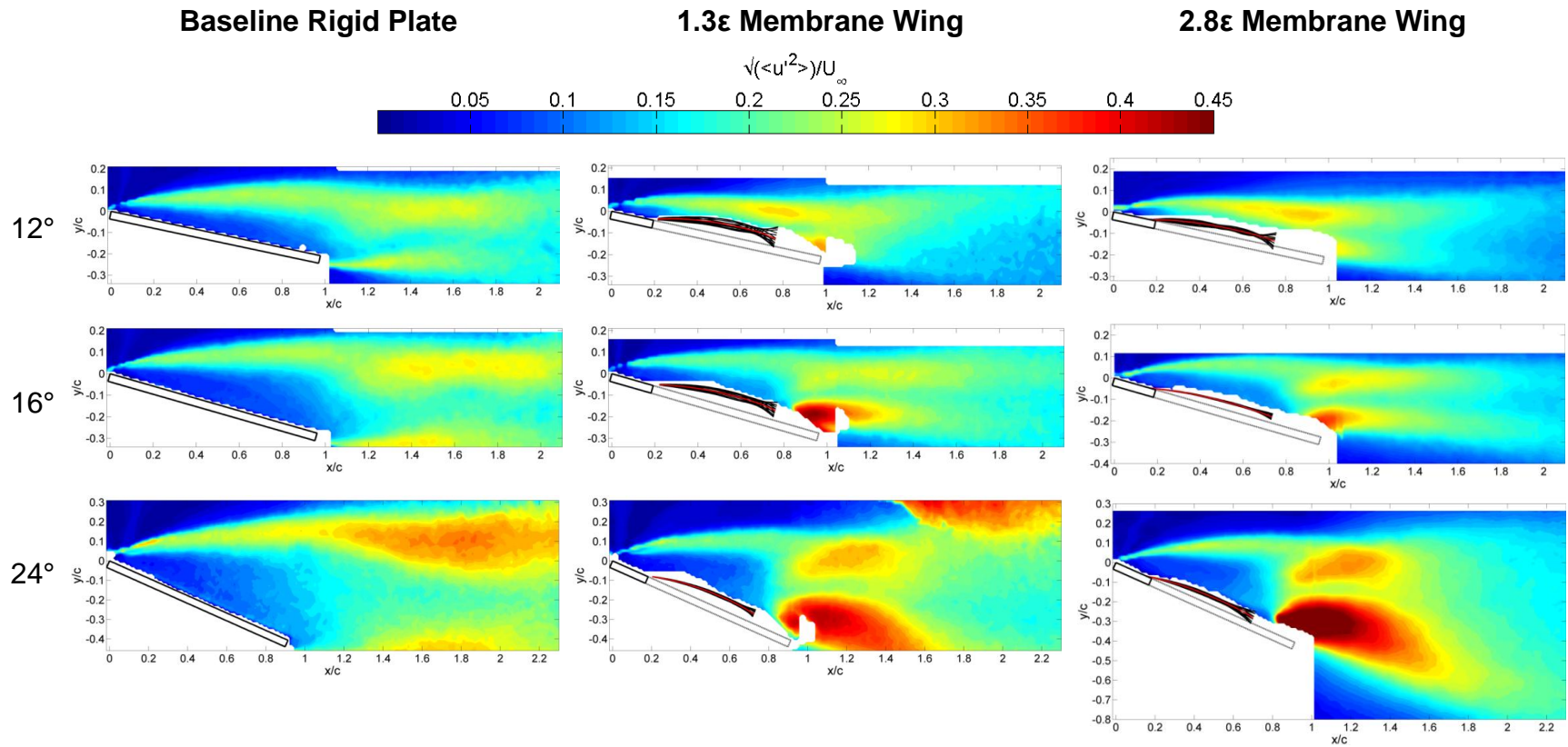


Figure 3-7.  $U_{rms}/U_\infty$  contours comparing baseline RP, 1.3 $\epsilon$  wing, and 2.8 $\epsilon$  wing at high aoa.

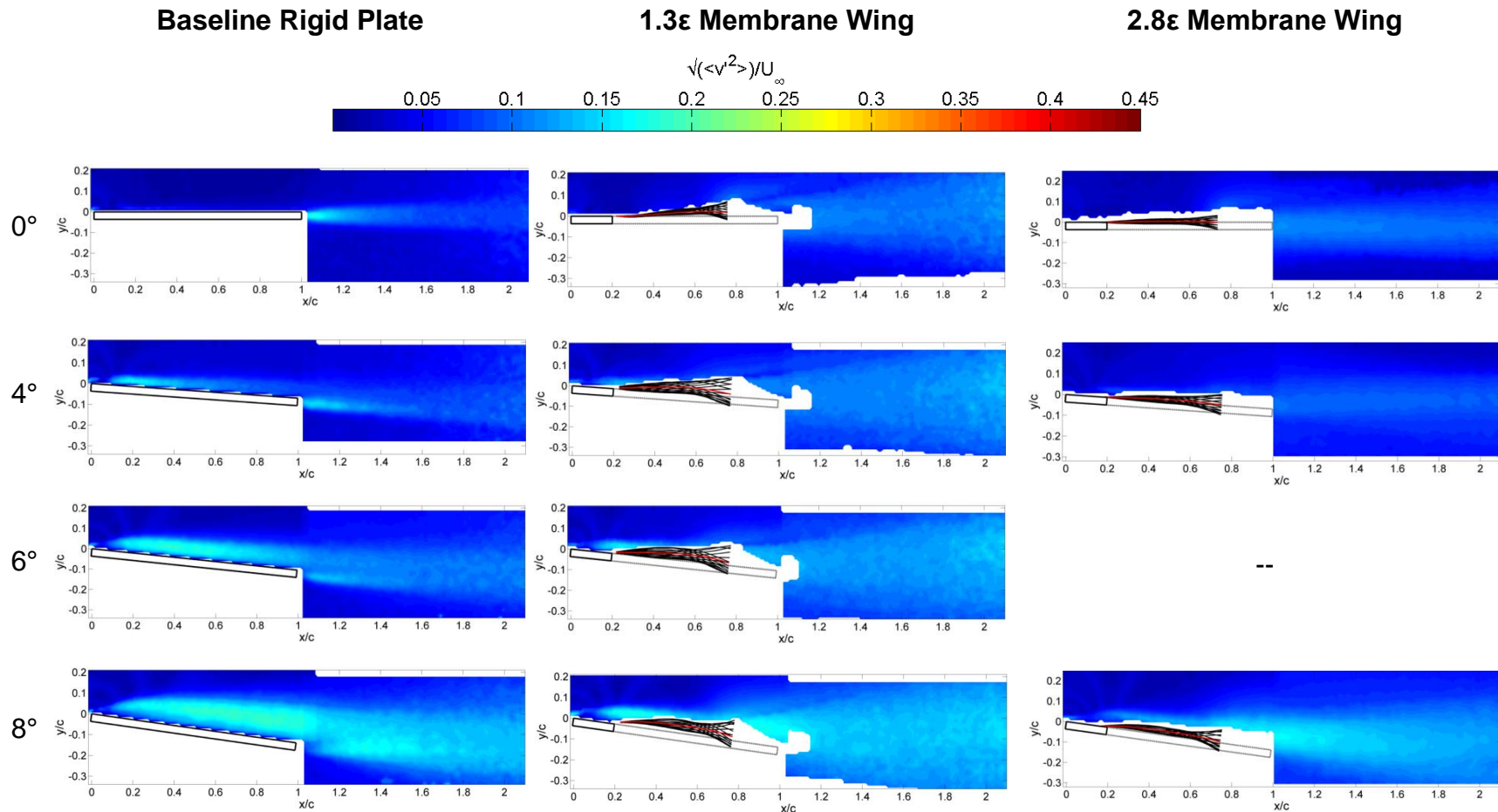


Figure 3-8.  $V_{rms}/U_\infty$  contours comparing baseline RP, 1.3ε wing, and 2.8ε wing at low aoa.

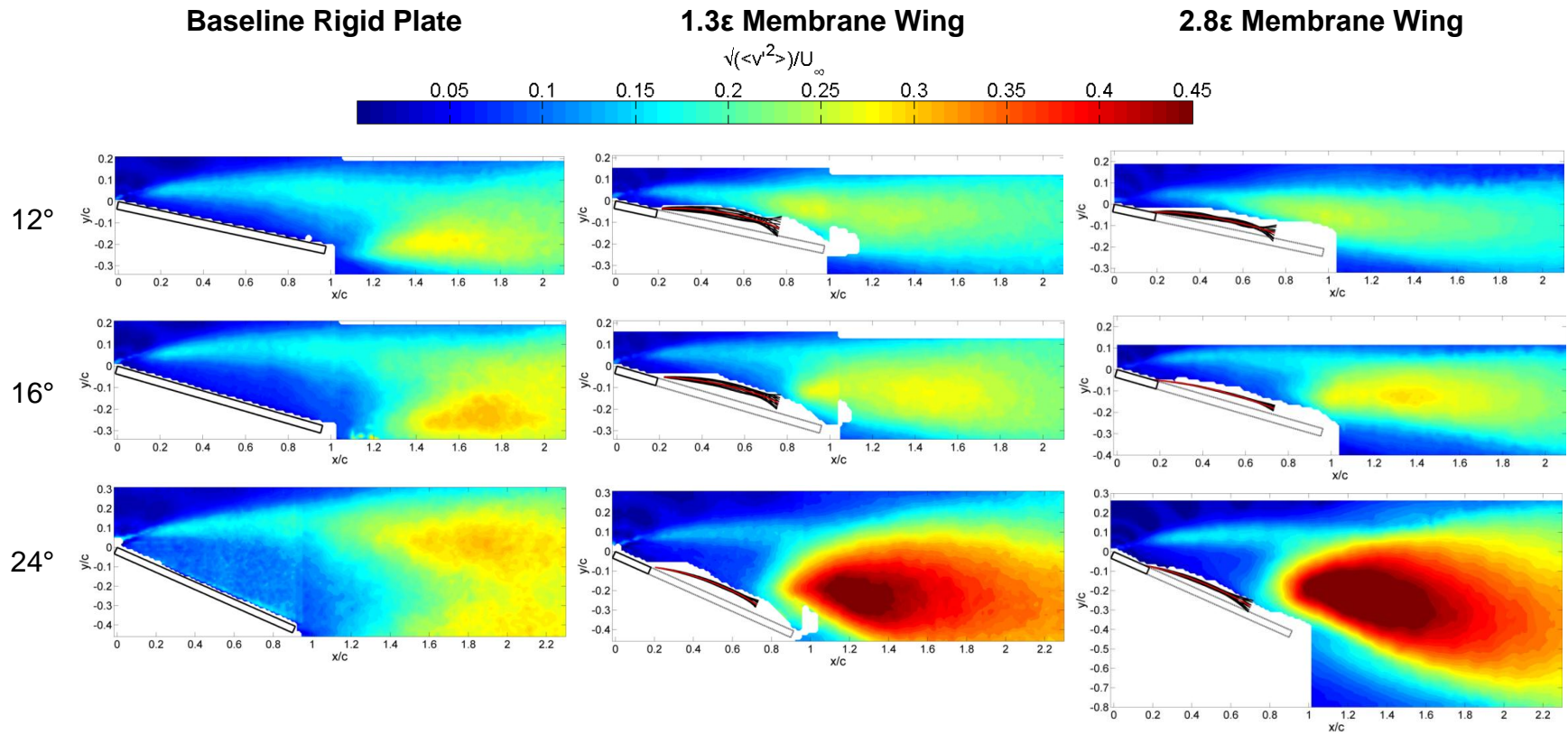


Figure 3-9.  $V_{rms}/U_\infty$  contours comparing baseline RP, 1.3 $\epsilon$  wing, and 2.8 $\epsilon$  wing at high aoa.

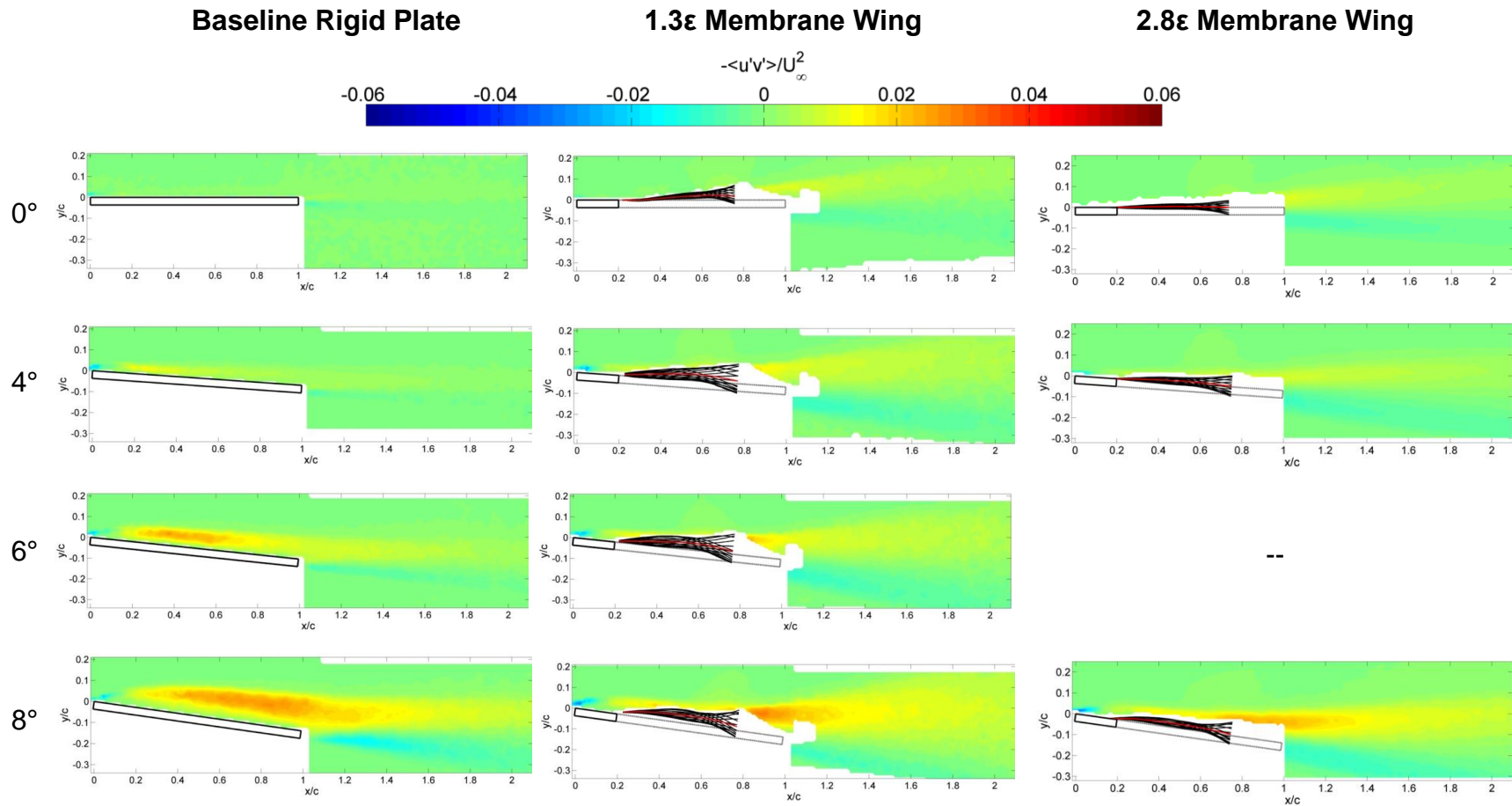


Figure 3-10.  $RSS/U_\infty^2$  contours comparing baseline RP, 1.3 $\varepsilon$  wing, and 2.8 $\varepsilon$  wing at low aoa.

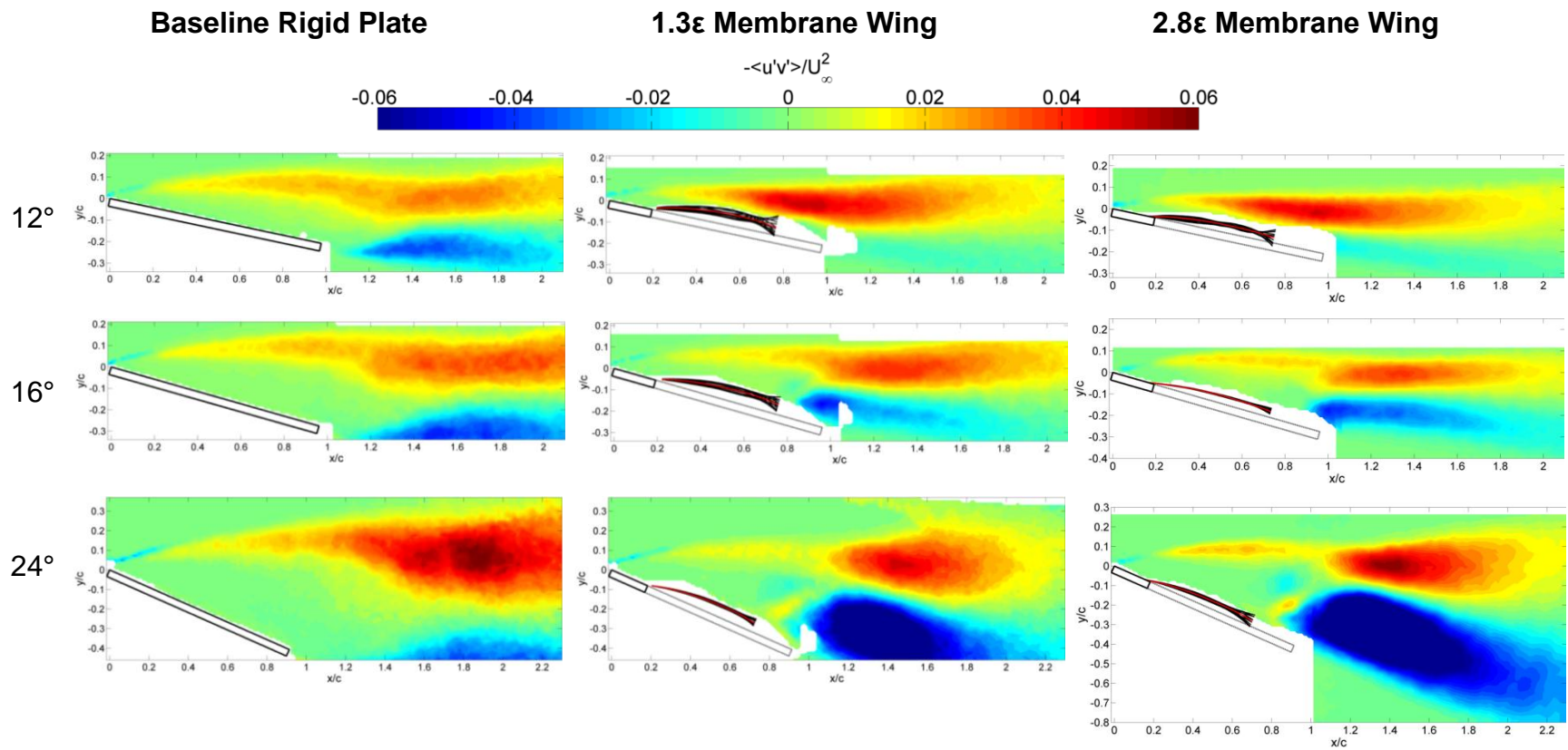


Figure 3-11. RSS/ $U_\infty^2$  contours comparing baseline RP, 1.3 $\varepsilon$  wing, and 2.8 $\varepsilon$  wing at high  $\alpha$ .

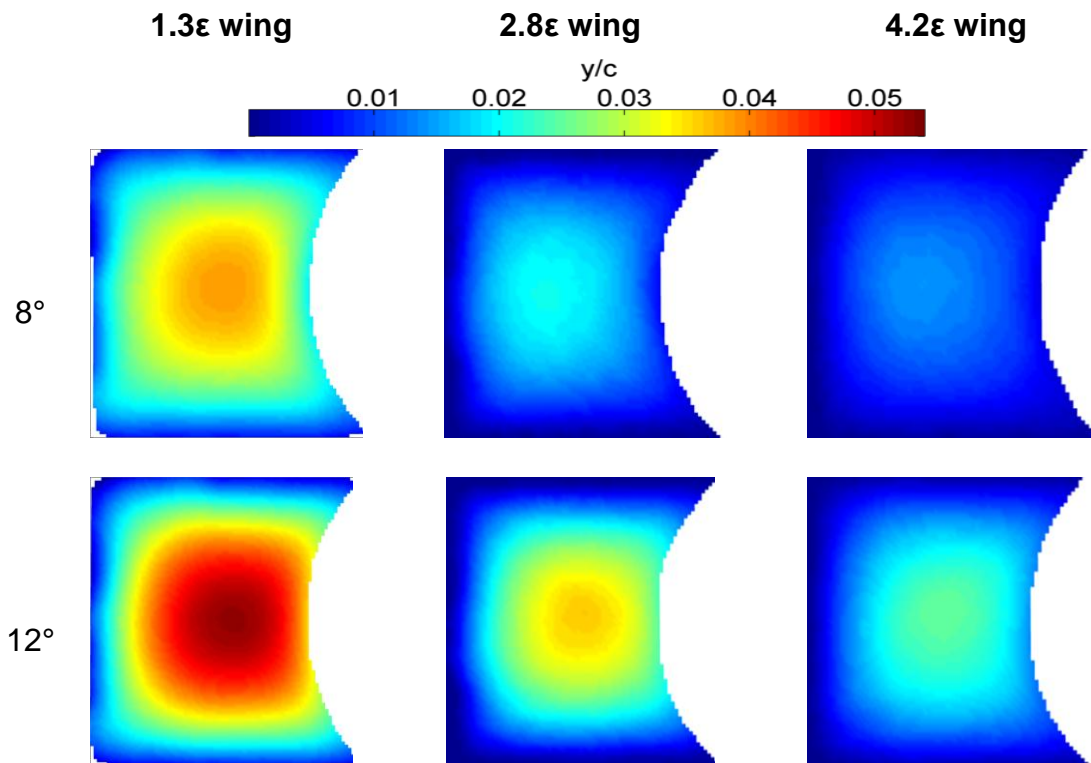


Figure 3-12. Mean membrane displacements  $y/c$ , for  $1.3\varepsilon$ ,  $2.8\varepsilon$ , and  $4.2\varepsilon$  wings.

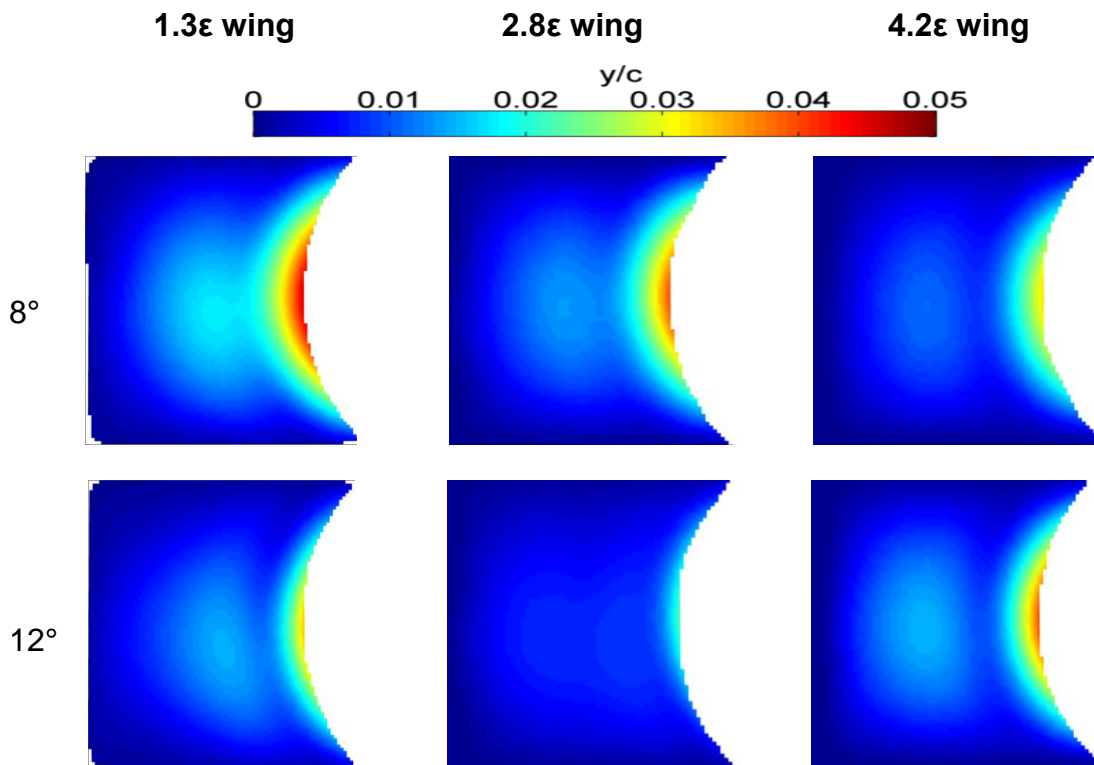


Figure 3-13. RMS membrane displacements  $y/c$ , for  $1.3\varepsilon$ ,  $2.8\varepsilon$ , and  $4.2\varepsilon$  wings.

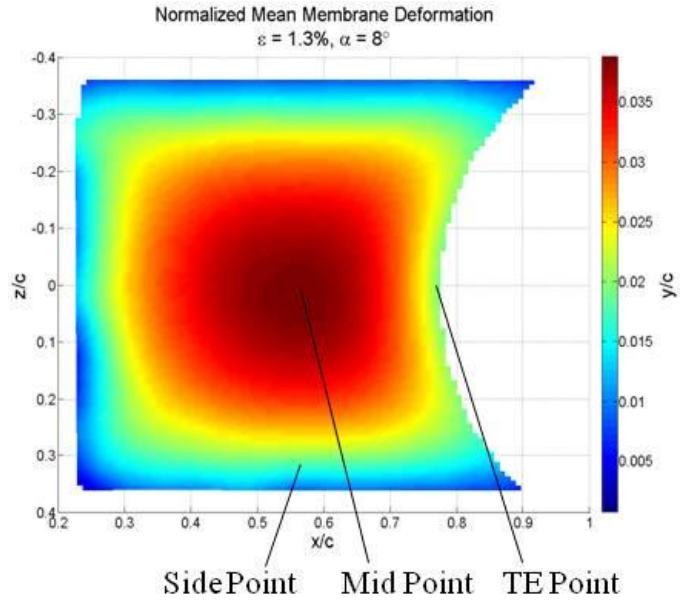


Figure 3-14. Indication of mid point, side point, and TE point on  $1.3\varepsilon$ ,  $\alpha=8^\circ$ , mean plot.

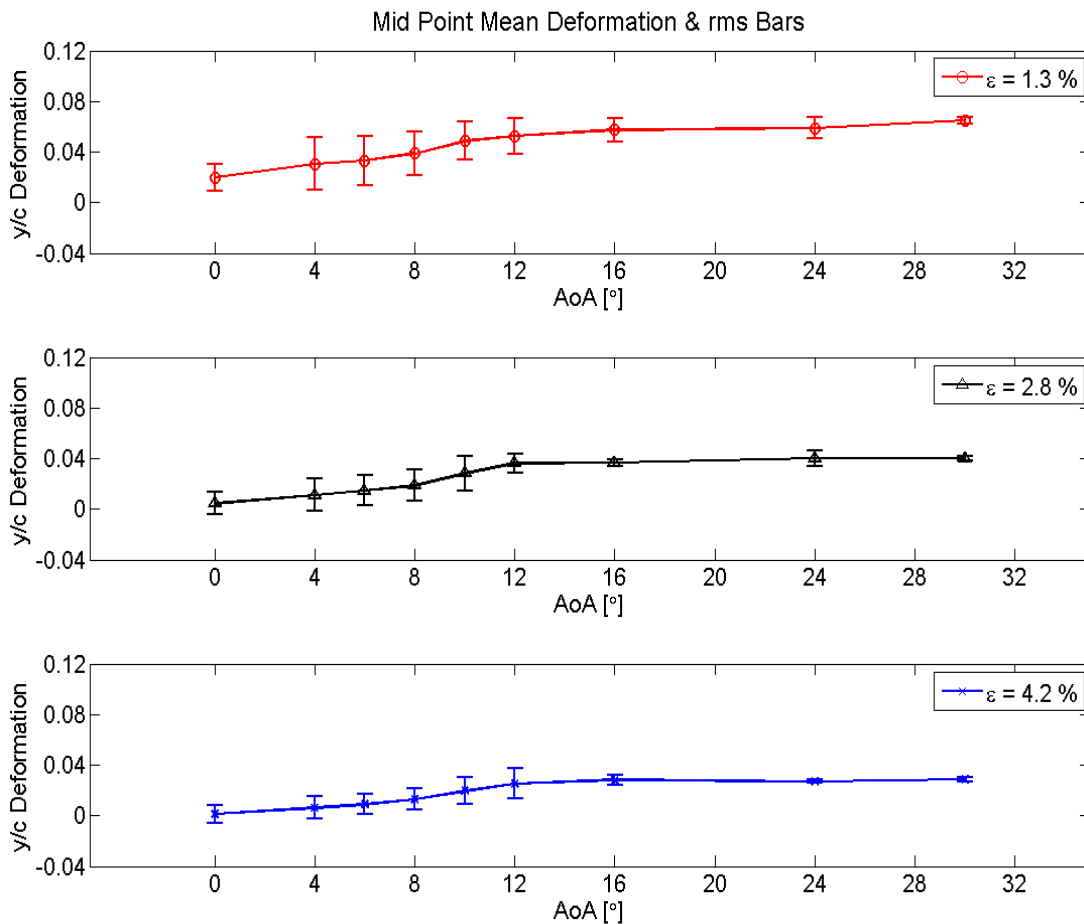


Figure 3-15. Mid Point mean and RMS deformation behavior vs. aoa,  $1.3\varepsilon$  red,  $2.8\varepsilon$  black, and  $4.2\varepsilon$  in blue.

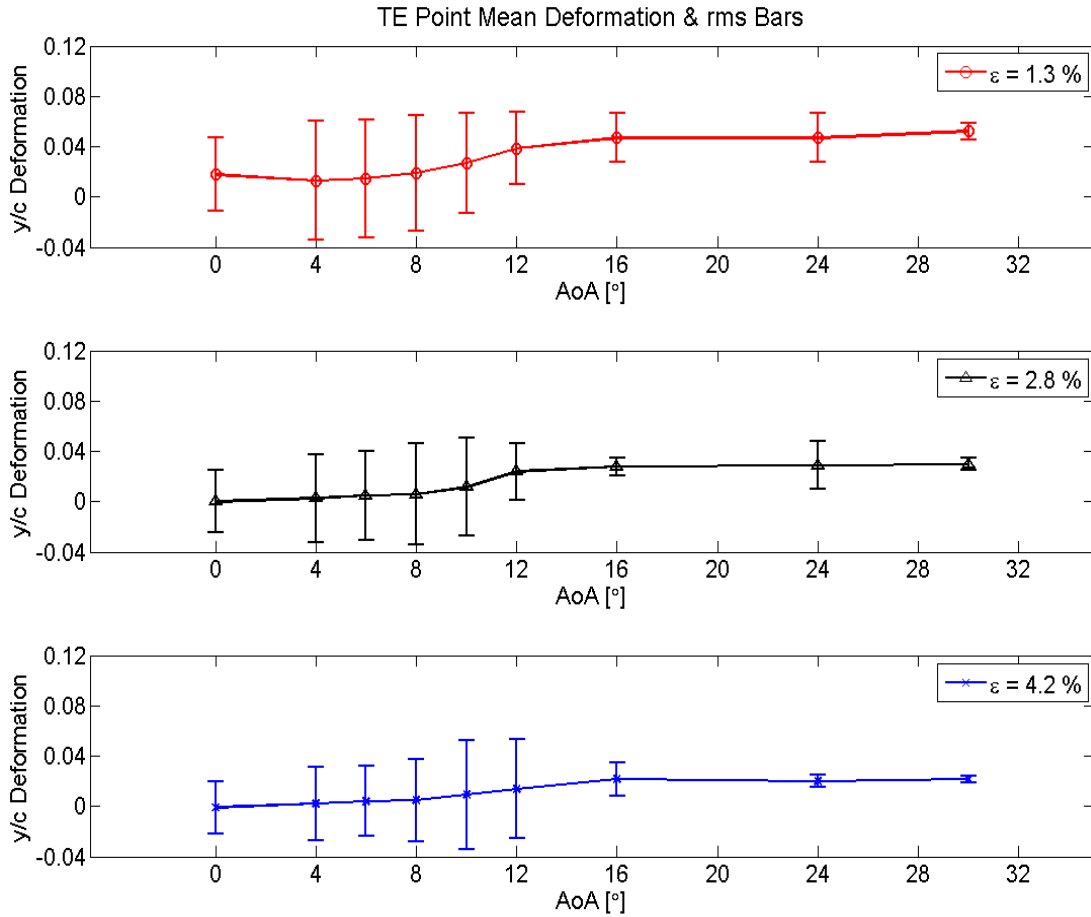


Figure 3-16. TE Point mean and RMS deformation behavior vs. aoa, 1.3 $\epsilon$  red, 2.8 $\epsilon$  black, and 4.2 $\epsilon$  in blue.

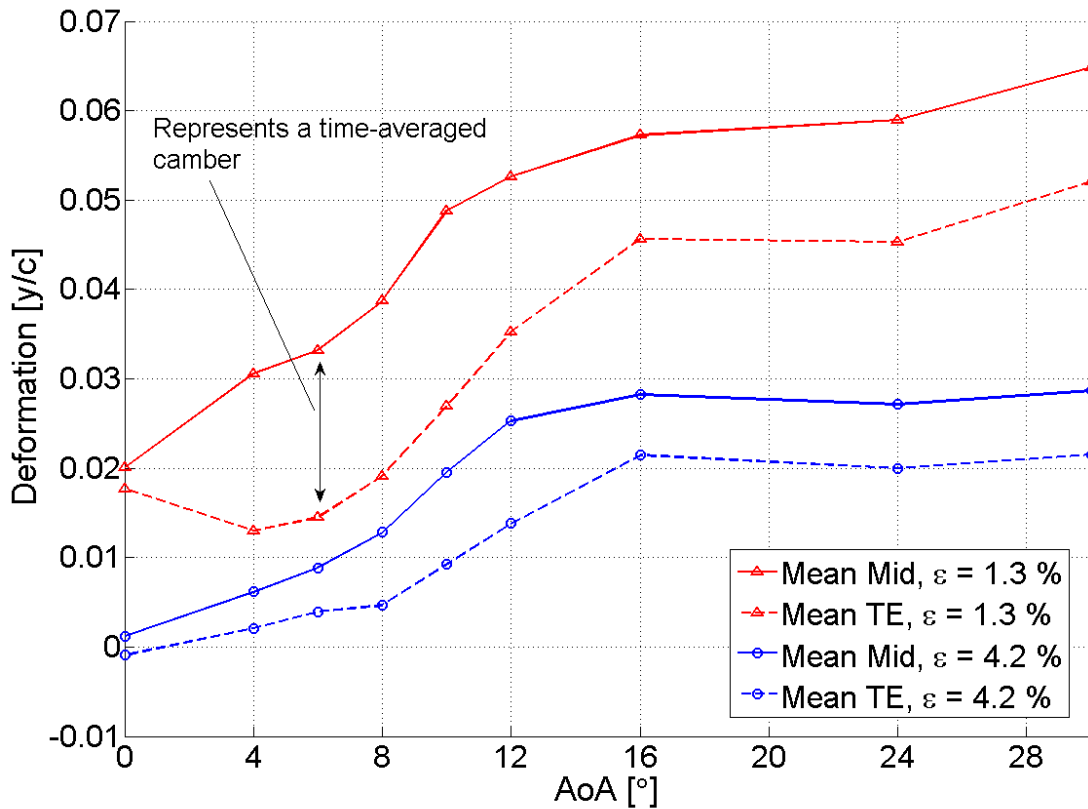


Figure 3-17. Time-averaged displacements (camber) of mid and TE points, full  $\alpha$ -sweep, comparing low and high pre-tension,  $1.3\epsilon$  and  $4.2\epsilon$  wings.

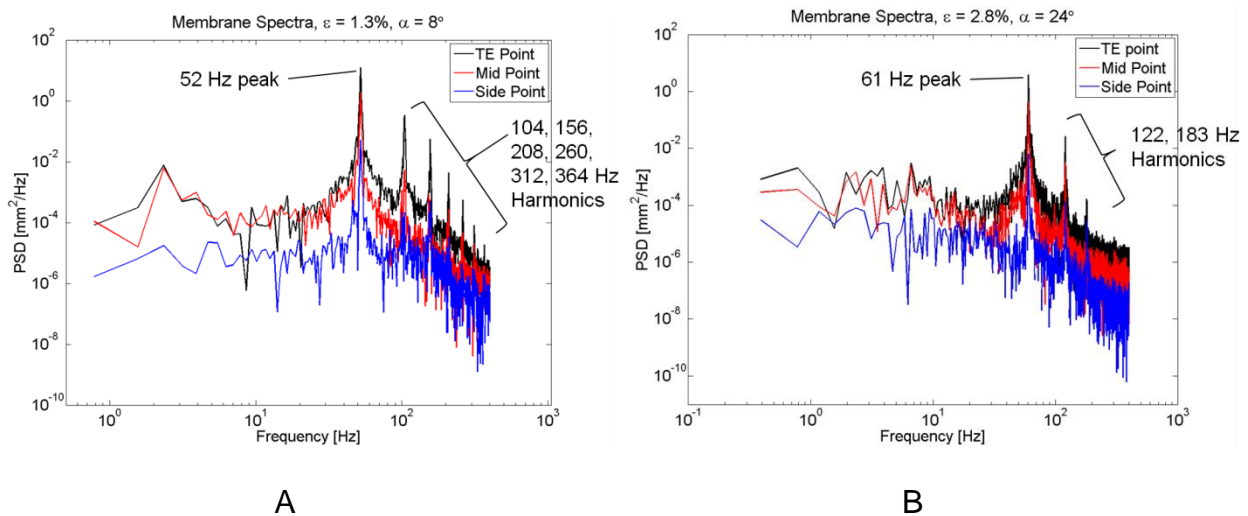


Figure 3-18. PSD computed from membrane Mid, Side, and TE Points showing peak vibration and harmonics. A)  $1.3\epsilon$  wing at  $8^\circ$ . B)  $4.2\epsilon$  wing at  $16^\circ$ .

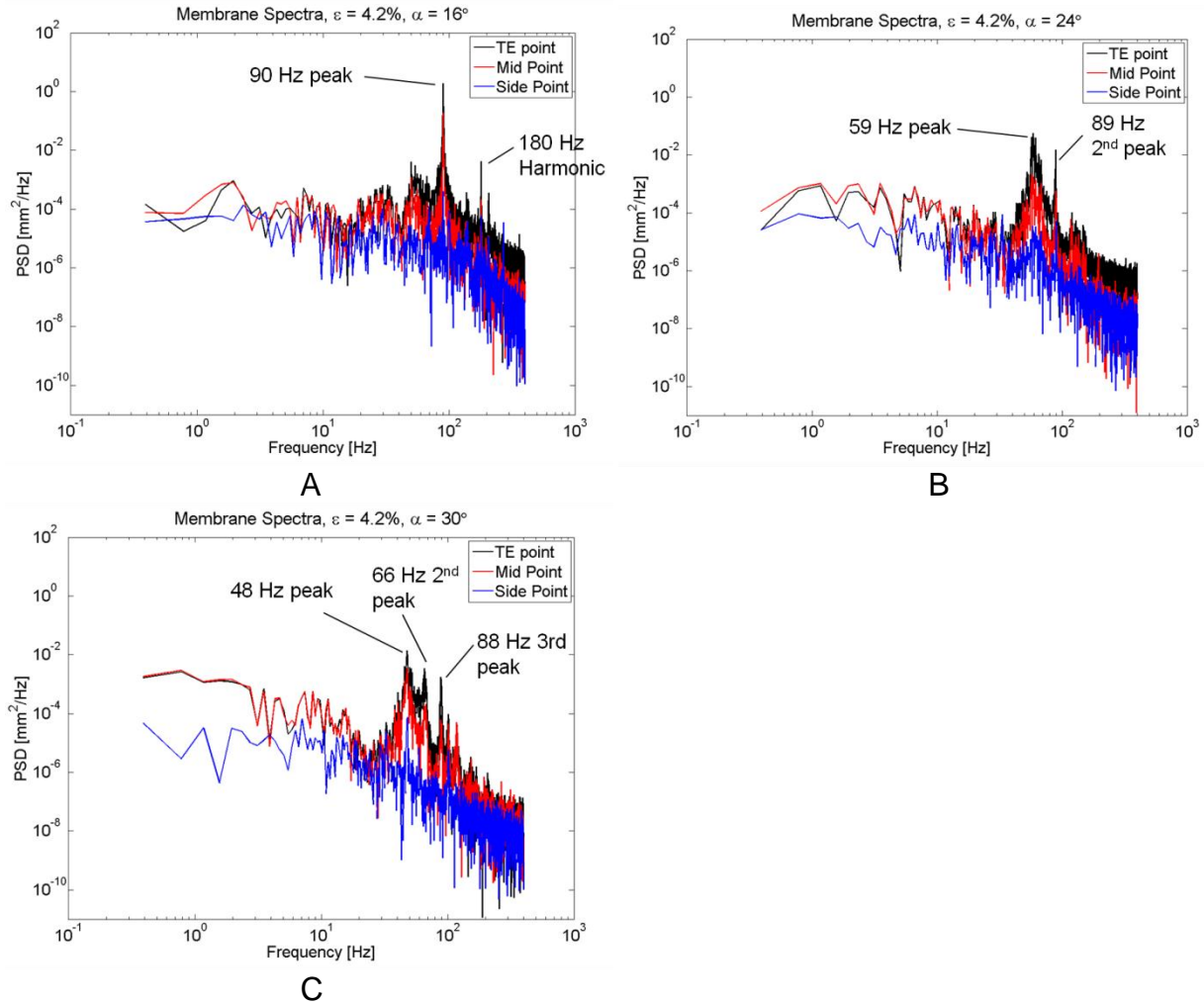


Figure 3-19. Spectral content portraying unique behavior of high pre-tension  $4.2\epsilon$  wing. A)  $\alpha = 16^\circ$ , high frequency (resonant) peak and harmonic. B)  $\alpha = 24^\circ$ , low frequency peak dominant. C)  $\alpha = 30^\circ$ , three peaks present, low is dominant.

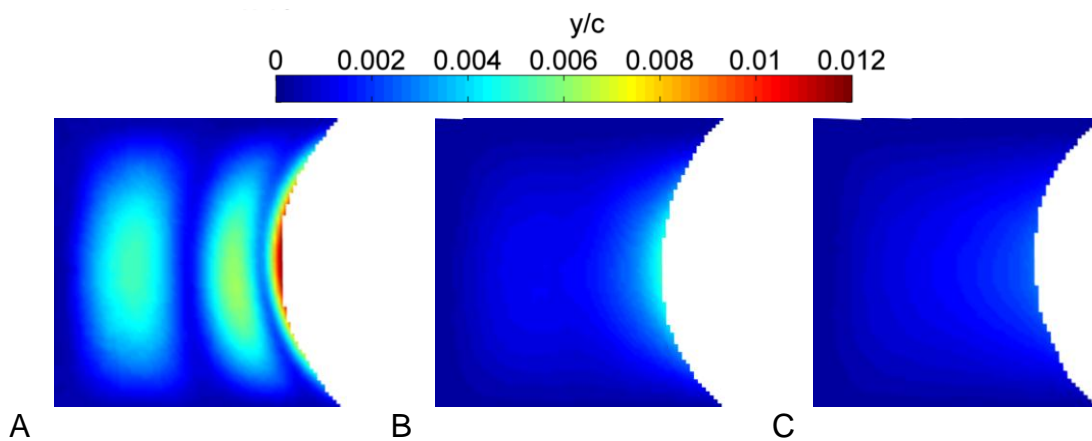


Figure 3-20. RMS properties for  $4.2\epsilon$  wing at high aoa. A)  $\alpha = 16^\circ$ . B)  $\alpha = 24^\circ$ . C)  $\alpha = 30^\circ$ .

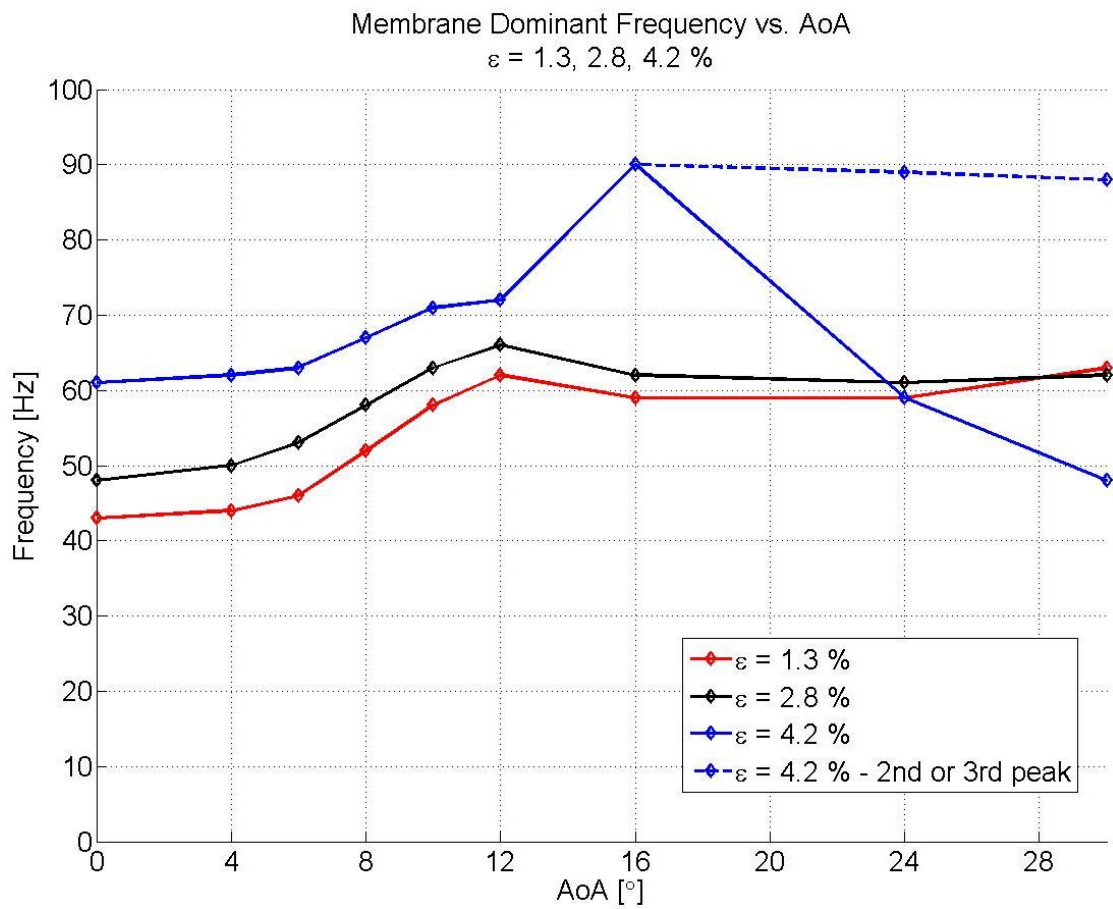


Figure 3-21. Vibration frequency vs. aoa for 1.3 $\varepsilon$ , 2.8 $\varepsilon$ , and 4.2 $\varepsilon$  membrane wings.

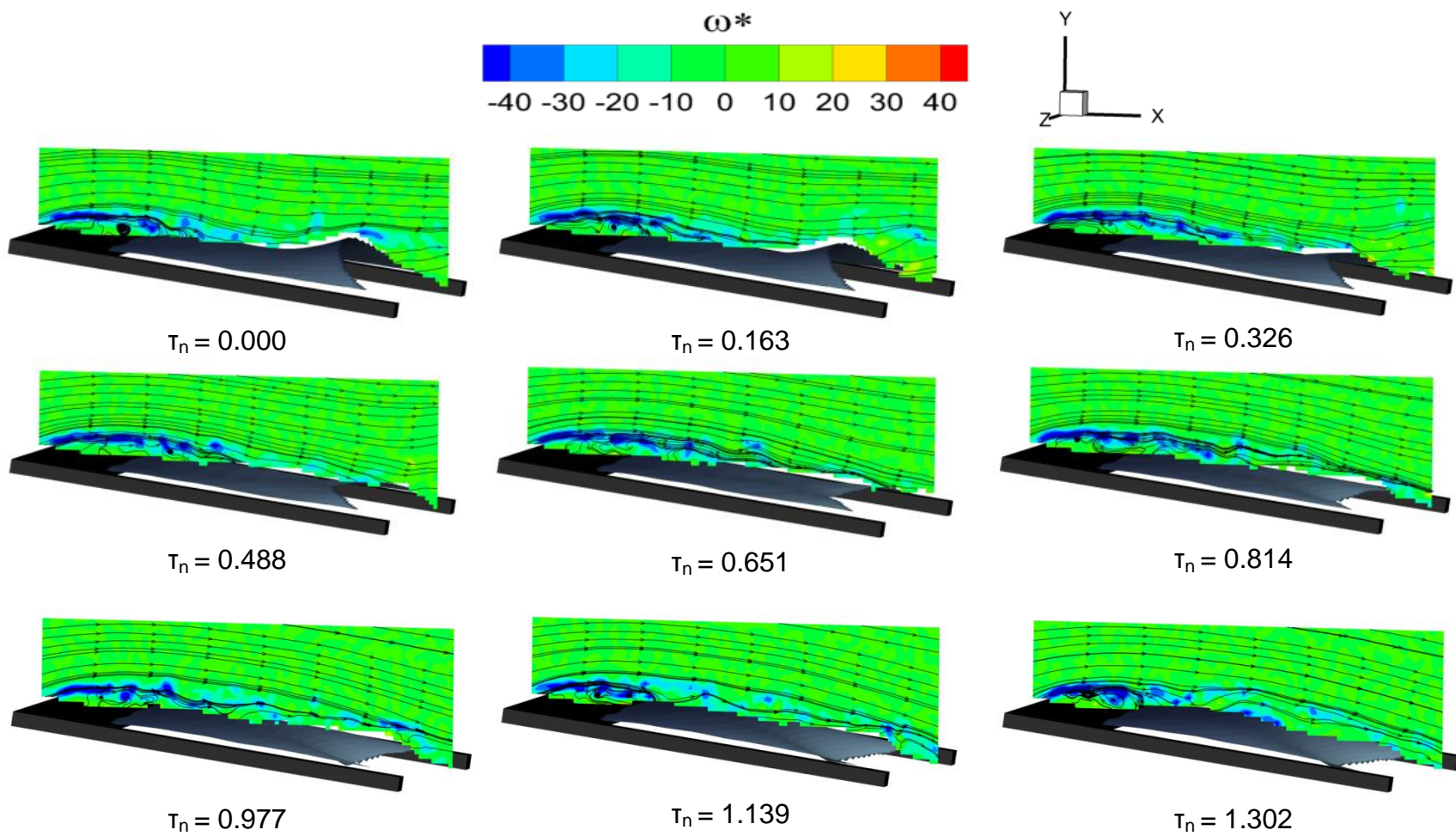


Figure 3-22. Normalized instantaneous vorticity,  $\omega^*$ , with streamlines for  $1.3\epsilon$  wing at  $\alpha = 8^\circ$ .

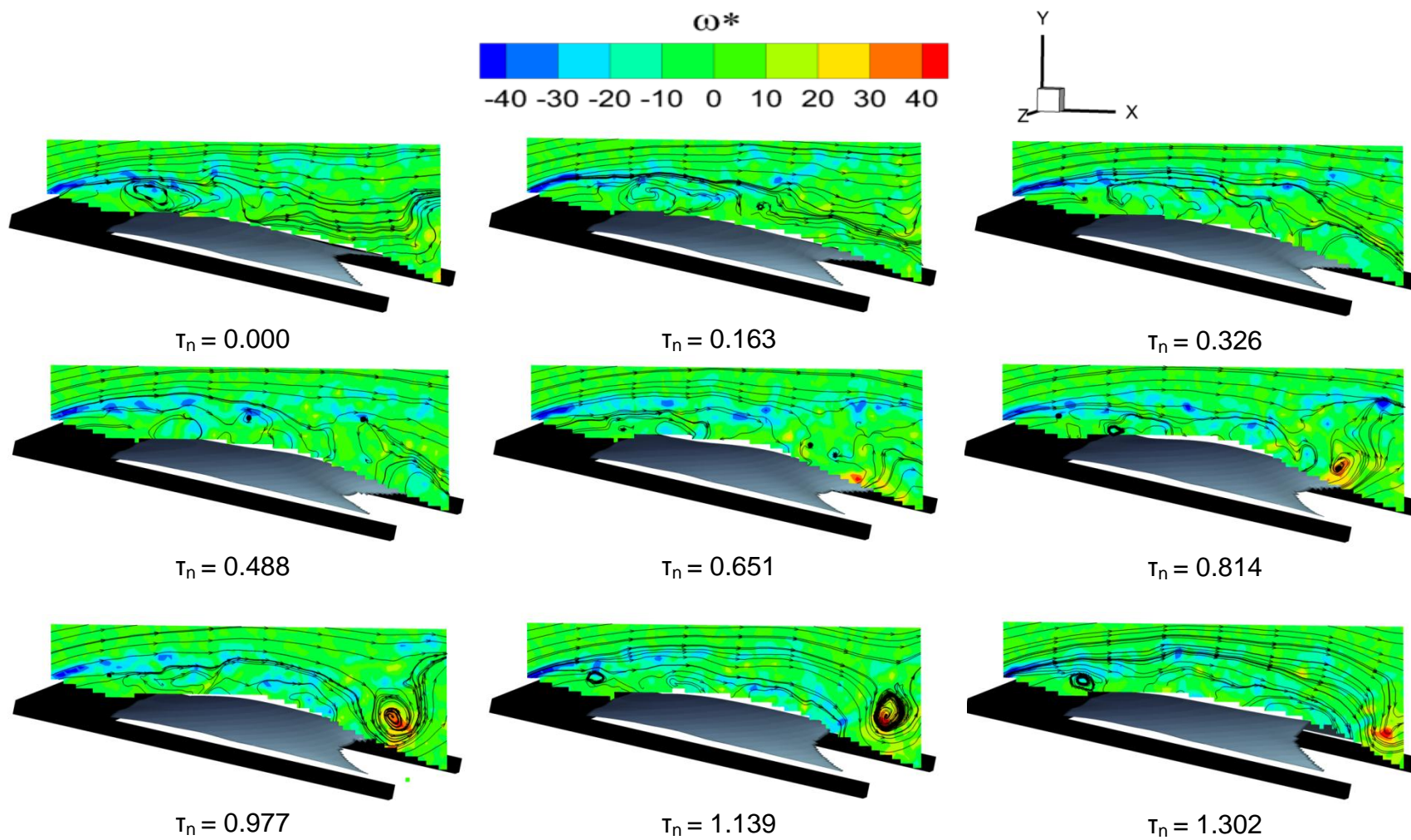


Figure 3-23. Normalized instantaneous vorticity,  $\omega^*$ , with streamlines for  $1.3\epsilon$  wing at  $\alpha = 12^\circ$ .

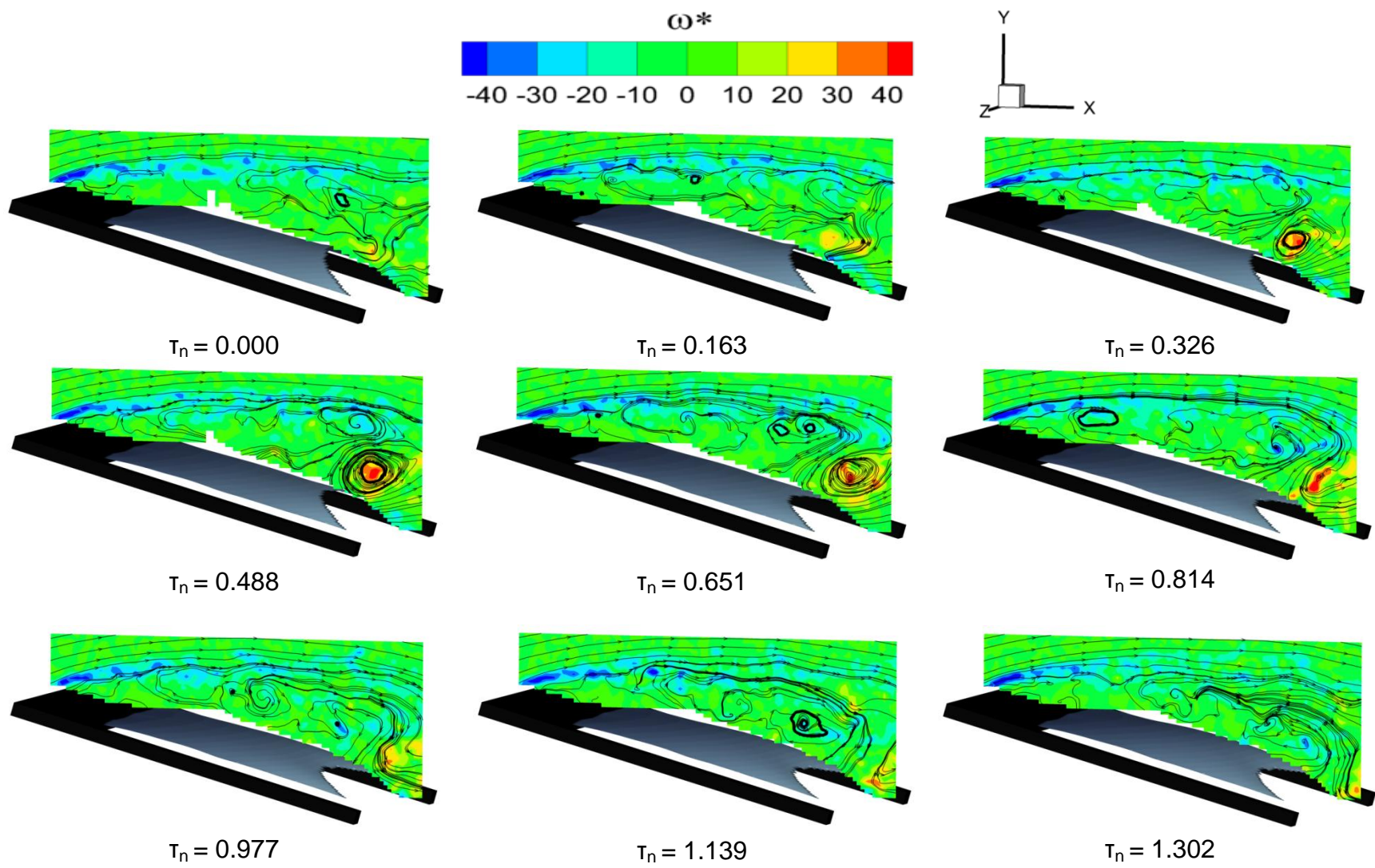


Figure 3-24. Normalized instantaneous vorticity,  $\omega^*$ , with streamlines for  $1.3\epsilon$  wing at  $\alpha = 16^\circ$ .

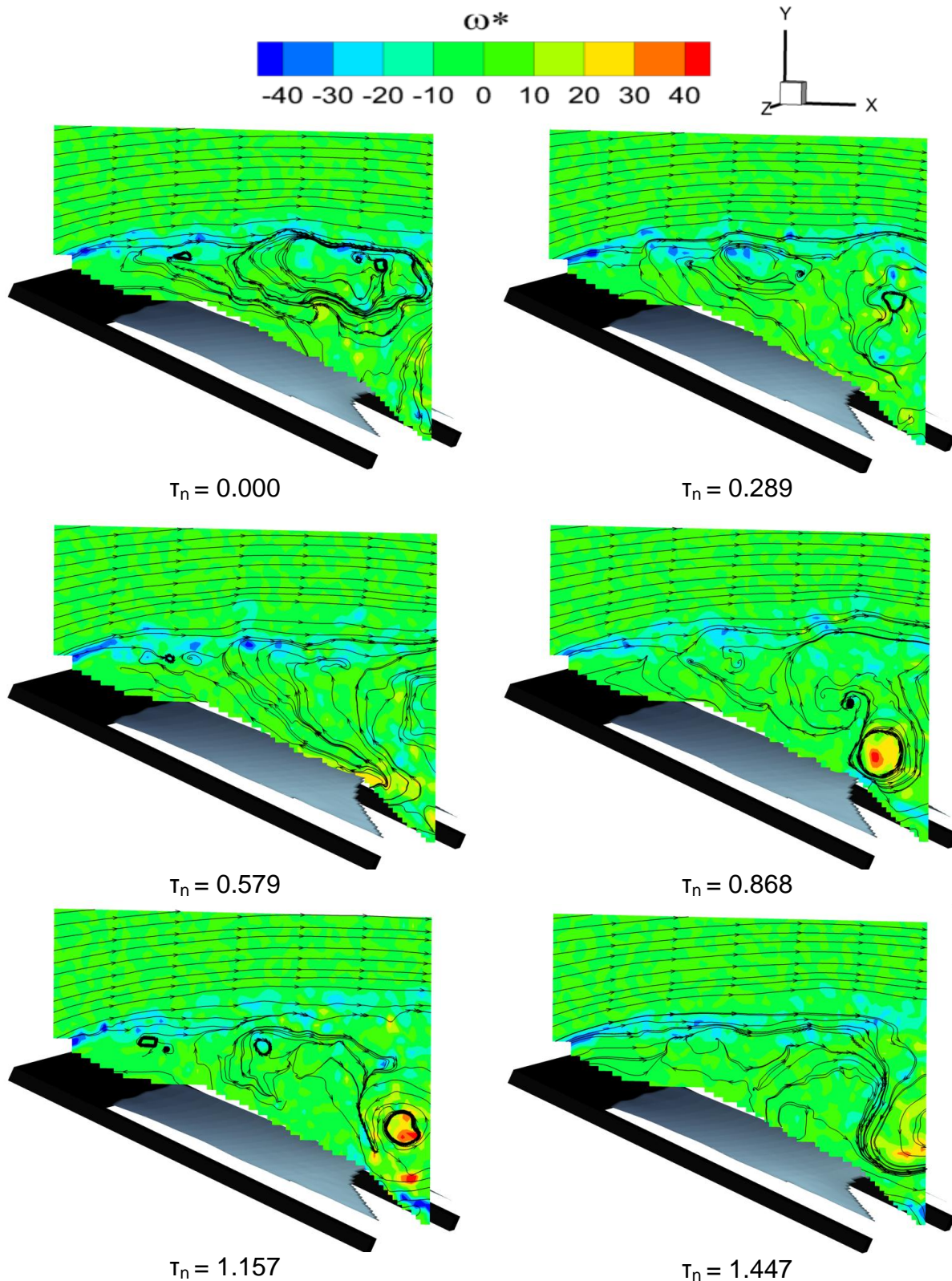
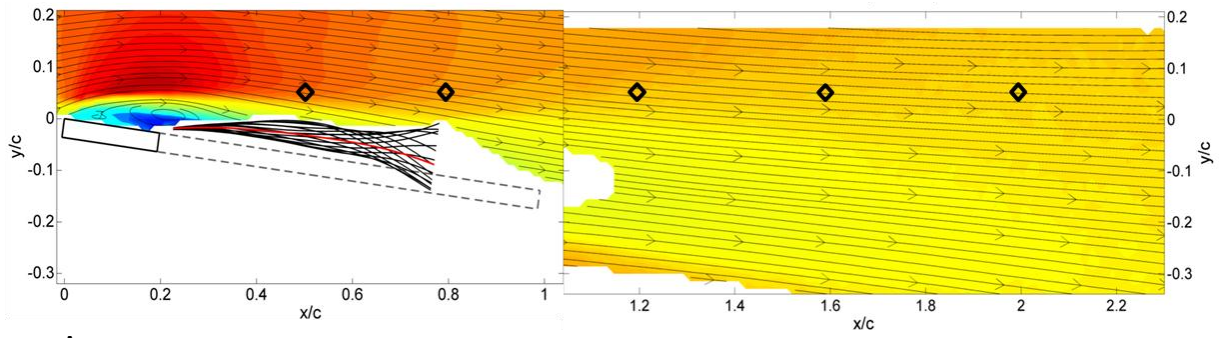
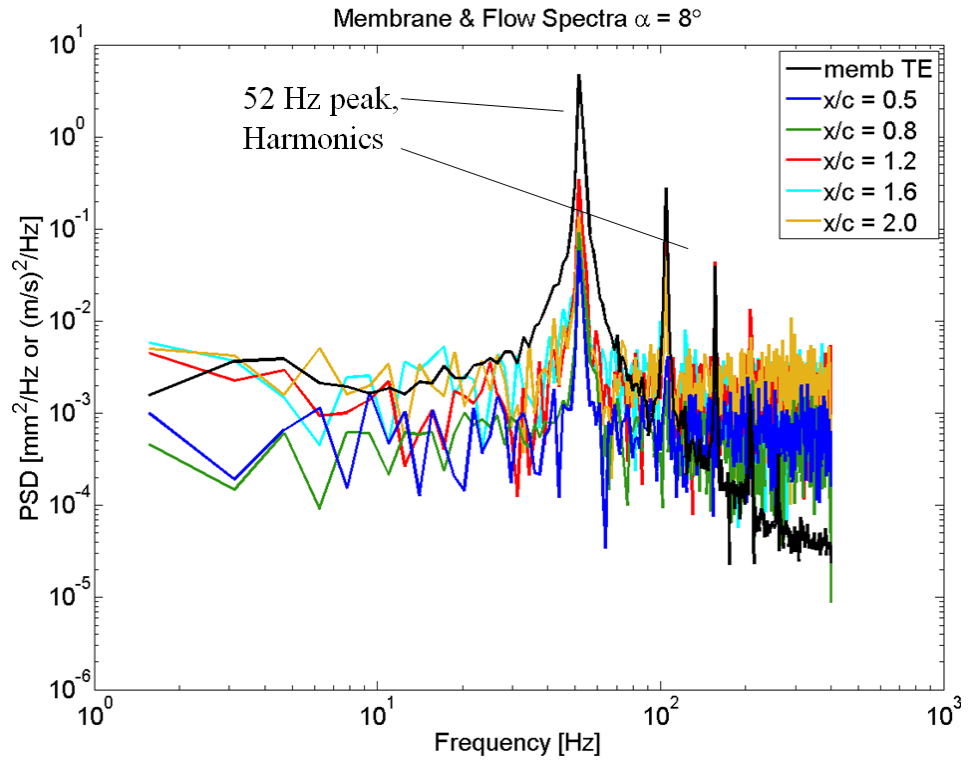


Figure 3-25. Normalized instantaneous vorticity,  $\omega^*$ , with streamlines for 1.3c wing at  $\alpha = 24^\circ$ .



A



B

Figure 3-26. PSD's showing membrane frequency in the flow field for  $1.3\epsilon$ ,  $\alpha = 8^\circ$ .  
 A) Locations of PSD indicated by diamonds over Umean plot. B) PSD of membrane TE combined with flow location PSD's.

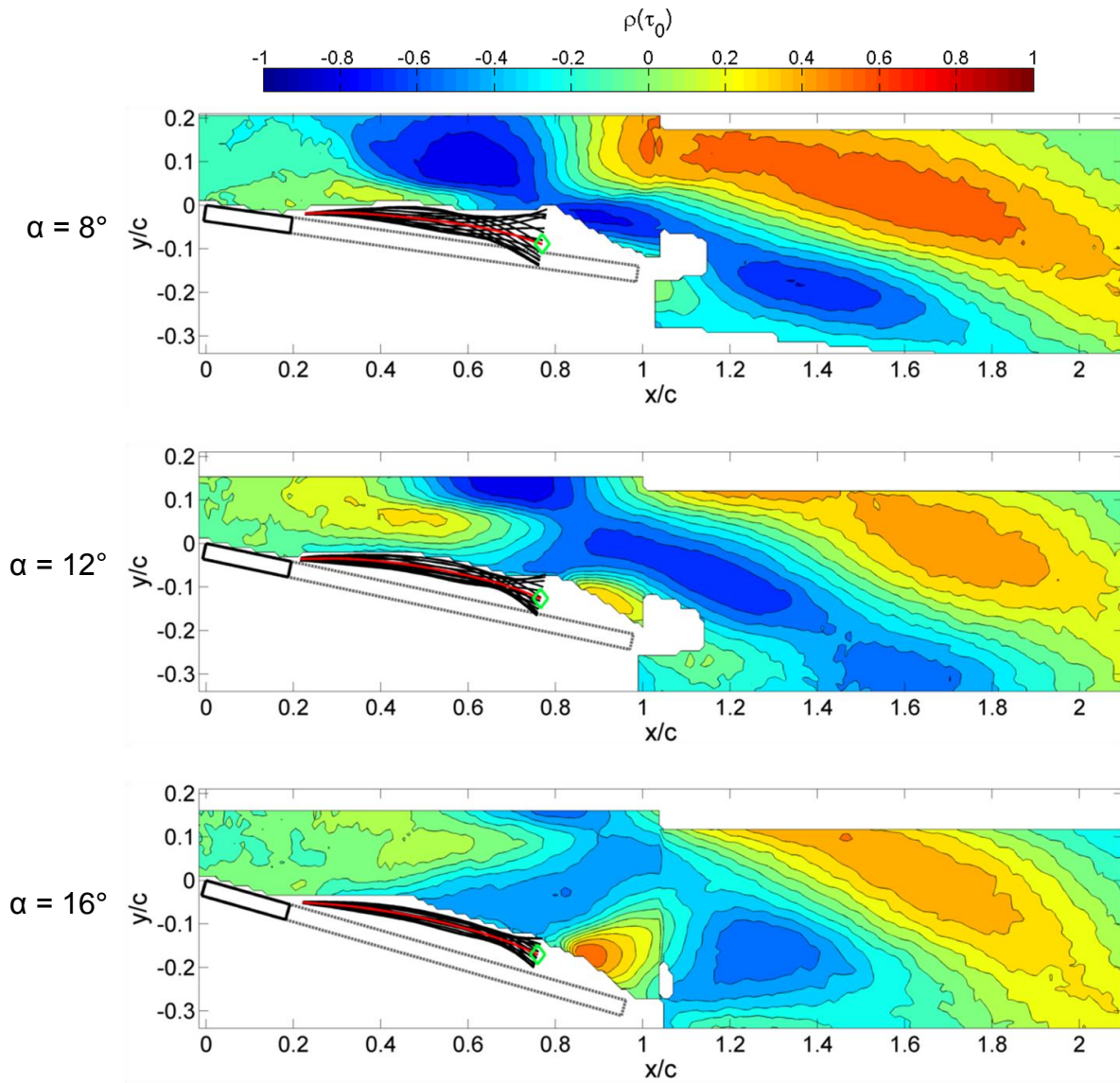


Figure 3-27. Correlation coefficient computed from TE  $m'$  and  $u'$  fluctuating signals.

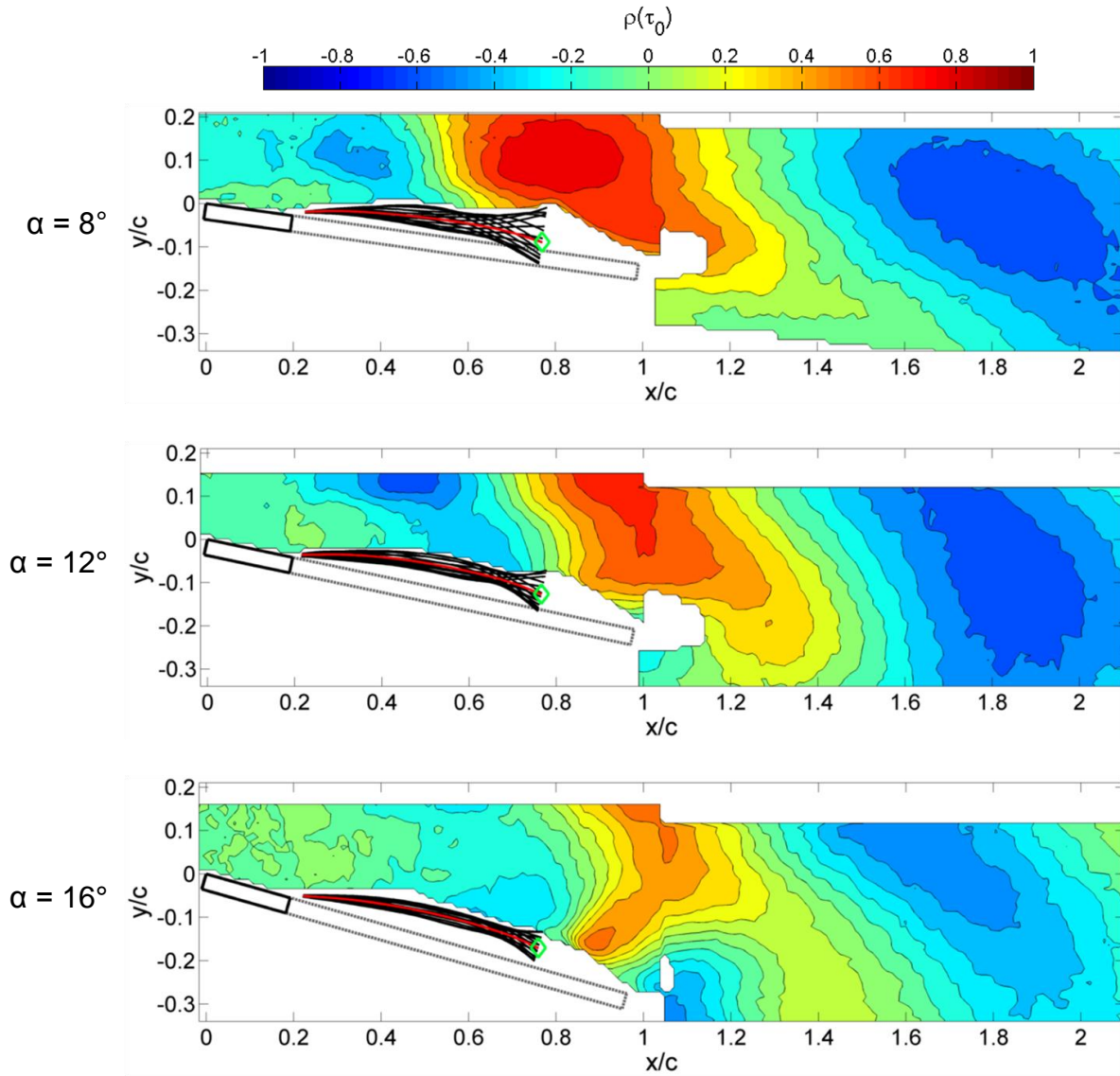


Figure 3-28. Correlation coefficient computed from TE  $m'$  and  $v'$  fluctuating signals.

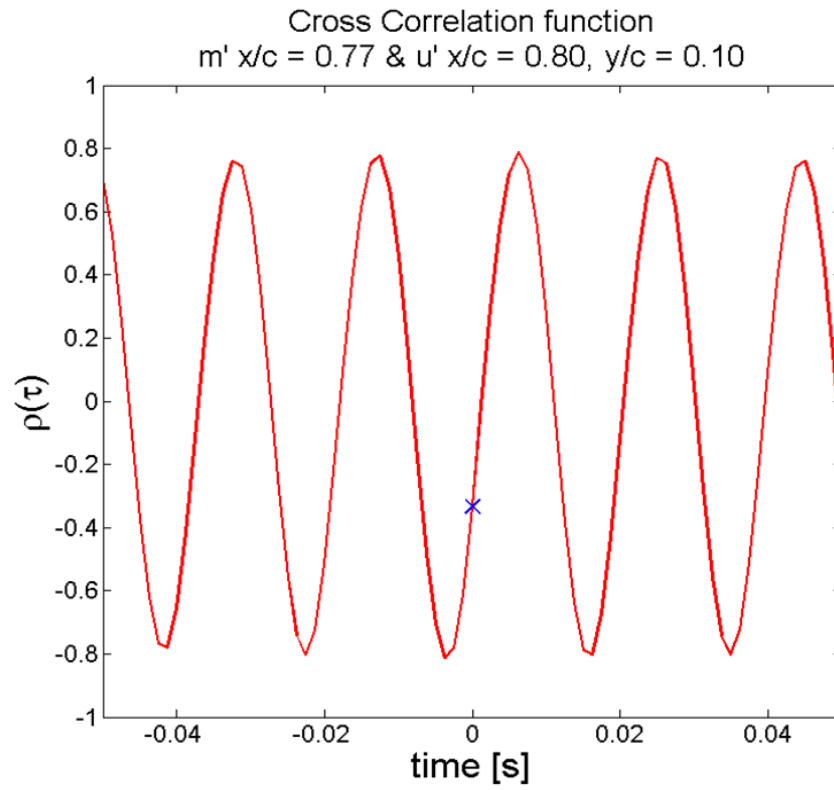


Figure 3-29. Cross correlation,  $\rho(\tau)$ , indicating periodic nature of the correlation values and that  $\rho(\tau_0)$  is not always near to maximum correlation.

## CHAPTER 4 CONCLUSIONS AND FUTURE WORK

Synchronous acquisition of time-resolved PIV and DIC data sets, as well as acquisitions made independent from each other, have been performed to study, in detail, the fluid-structure interactions of low Re membrane wings. Mean, fluctuating, and instantaneous flow and membrane properties have been explored and discussed. The multi-cell, batten-reinforced, and scalloped membrane wings were created under heating to create varying pre-tensions (low  $\varepsilon = 1.3\%$ , medium  $\varepsilon = 2.8\%$ , and high  $\varepsilon = 4.2\%$ ). In a collaborative and parallel effort force data was obtained for the same wings. A rigid flat-plate of identical aspect ratio was incorporated as a baseline wing.

### **Summary**

Mean streamwise flow analysis showed the baseline plate having a growing separation bubble (originating from the leading edge) at low  $\alpha$  before completely separating near  $12^\circ$   $\alpha$ . The membrane wings demonstrated a reduction of the size of the separation bubble, keeping the flow attached to higher angles of attack, and showed higher wake velocities. At higher angles of attack, the baseline case showed recirculated flow extending far into the wake, while membrane wings showed much less recirculation in all cases. At high  $\alpha$ , and a favorable downwashed wake was seen for membrane wings. Force data confirmed better aerodynamic efficiency for membrane wings and continued lift generation at high  $\alpha$  coinciding with mean flow interpretation. The medium pre-tension wing ( $2.8\varepsilon$ ), appeared more aerodynamic than the low pre-tension ( $1.3\varepsilon$ ) by showing higher flow accelerations, thinner shear layers, and more favorable wake velocities through flow analysis but could not be validated with force data.

Root-mean-square flow fluctuations and Reynolds shear stress values portrayed growing shear layers from the leading- and trailing-edges for the rigid plate. For the membrane wings, shear layers were seen being pulled tighter to the surface and also impinging and interacting with membrane oscillations, up to  $12^\circ$  aoa. At high aoa, enhanced turbulent mixing and momentum transport was seen for the membrane wings. At  $24^\circ$  aoa, particularly large stream and vertical flow fluctuations were seen in the near wake, driven by the membrane motions.

Analysis of the membrane vibrations, incorporating the high pre-tension ( $4.2\varepsilon$ ) wing as well, showed trends of dependence on angle of attack (average pressure), pre-tension (average tension), and flow behavior. When the shear layer was interacting with membrane, there was an increase in the membrane frequencies ( $\alpha \leq 12^\circ$ ) and larger RMS fluctuations. At these lower angles of attack, the membrane motions appear driven by the capture of dynamic pressure around the quarter chord location, which travels the length and gets released at the trailing-edge. Peak frequencies on average were found in the range of the estimated natural frequency  $\sim 58$  Hz. The vibration frequencies are much faster than typical deployable control surfaces (while the membrane itself is very lightweight and actuates freely) which can assist as passive control during gusty flight conditions. The high pre-tension case showed that under high tension, unique vibration behaviors can arise, but fluctuations and mean distention are greatly reduced. Time-averaged membrane shapes showed adaptive cambering with the extent largely dependent upon pre-tension. There was an association of largest passive cambering and most efficient aerodynamic performance from force data by the low pre-tension model.

Plots of the instantaneous vorticity field revealed much about the time-dependent nature of the FSI. At low angle of attack, shearing from the LE was seen to interact with the membrane distended up and then pass closely to the surface when it was down. As  $\alpha$  is increased, the membrane trailing-edge generated vortical structures by allowing a rush of fluid to pass under it, which quickly interacts with fluid being pulled down by the returning membrane motion. This typically creates a counter-clockwise vorticity structure that was found to affect streamlines of high and low momentum flow, enhancing the momentum transport. Vortex roll-up and shear layer excitation, as reported in other studies, were also seen in flow overtop the membrane's surface particularly as the flow tended toward separation at  $12^\circ$ .

The coupled flow and membrane behavior, as well as insight into where the membrane oscillations were most influential were investigated through spectral and correlation analyses. Membrane frequency content was seen throughout the flow field, as the flow was forced to oscillate at the membrane's dominant frequency. The power of the spectra depended on deviation magnitudes and was greater in the wake and near the membrane TE. Contours of the correlation coefficient showed that the membrane and flow fields were highly correlated and that local flow accelerations and decelerations were caused by the membrane motions. Correlations were shown to oscillate at the membrane frequency and have spatial and temporal dependence. The membrane influence was considerably weaker upstream of it, while still statistically significantly correlated. There was also a dependence of correlation strength on angle of attack, with generally lower values found at higher angles, likely dependent on the reduction of membrane vibration amplitude.

## Future

While some details of low Reynolds flow and membrane wing interactions were discovered in this study, there is much more to understand. The unsteady vorticity interactions, high turbulence intensities, and RSS behavior all indicate the complexity and three-dimensionality of the flow. In future study, spanwise and 3-component streamwise PIV could be incorporated to investigate flow in between membrane cells (batten plane) and in the nearest wake of trailing-edge interactions. The wing aspect ratio is also important, the effects at the wingtips, and how they interact with or alter membrane vibrations should be studied.

A study dedicated to tension effects could be carried out with the improved mounting and seeding developed in the progression of this work. This coupled with another thorough and precise loads study may enlighten answers to the sometimes contrasting results from the present research. The medium pre-tension model ( $2.8\varepsilon$ ) showed most favorable flows throughout, while the low pre-tension ( $1.3\varepsilon$ ) wing showed the most efficient aerodynamic forces.

The high correlation values found lend themselves as a basis of mathematical decomposition such as POD or stochastic estimation techniques. From these or future synchronized data sets, low order predictive models could be generated which govern the highly unsteady and coupled fluid-structure problems. Mutual flow and structure solvers will be more easily validated and honed by experiments such as these.

The results of this work have shown a dependence of the flow behavior on membrane oscillation frequency and amplitude. While characterized, the details and intricacies of mechanisms driving the membrane oscillations, and how those vibrations may be modeled as a predictable dynamic system, remain to be discovered.

## APPENDIX DYNAMIC MASKING

This appendix will demonstrate an example of the dynamic masking techniques as applied to the 80x80\_2.8ε model at 12° aoa. Figure A-1 shows the raw image, 2<sup>nd</sup> PIV frame where the in-PIV-frame (center cell) membrane is distended 'up' from the inverted model surface.

The 1<sup>st</sup> step is to track the bright pixels by Sobel edge detection and to remove bright seed pixels by looping spatial filtering until only pixels involved with the laser reflection of the model and membrane surface remain.

The 2<sup>nd</sup> step is to apply a high-order polynomial fit curve to the bright pixels which gives a line that outlines the membrane shape, to be stored (Figure A-2).

The 3<sup>rd</sup> step is to use the tracked shape to close a geometry that outlines membrane regions and define the shape of the masks (Figure A-3).

Finally, the mask black-white image would be reshaped into a grid size that could be fitted with the PIV vector matrices and the process was repeated for all images.

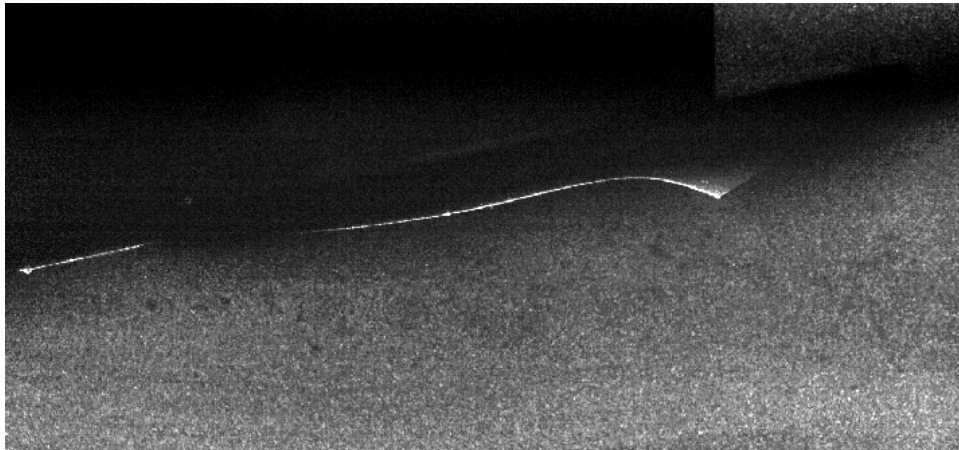


Figure A-1. 2<sup>nd</sup> frame PIV image, 80x80\_2.8ε at 12° aoa.

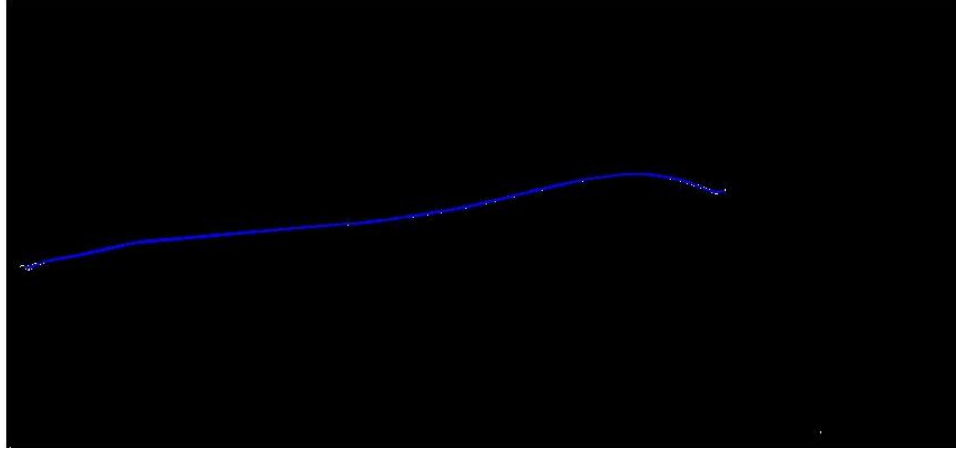


Figure A-2. Polynomial line tracking bright-pixel membrane shape.

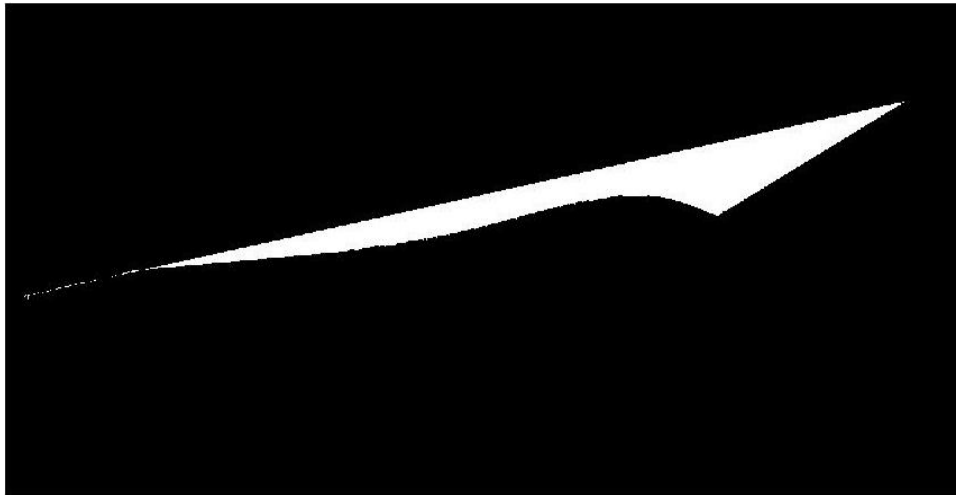


Figure A-3. Example mask where membrane resides created using bright pixel line and known model batten TE point.

The following method was used to track dark regions created by the out-of-plane (side cell) membranes or if seeding swayed in the wake frame. Figure [A-4](#) provides an example of an image where an out-of-plane membrane created a shadow that hid the in-plane membrane and would cause invalid PIV data.

Since the seed could cause very pixilated regions of lighter and darker light intensities, the image is blurred by a 7x7 mean filter convoluted with the original image (Figure A-5).

The blurred image was then turned directly into a mask by black-white conversion, using an Ostu developed gray-scale detection function to dictate which regions were dark or light. The mask is shown in Figure A-6.

Finally, it should be noted that these dynamic masks were combined with a static mask for each angle of attack tossing out data generated from 'below' the static model surface to create the final mask used with velocity data.



Figure A-4. 2<sup>nd</sup> frame PIV image, 80x80\_2.8ε at 12° aoa showing shadow from out-of-plane membrane.

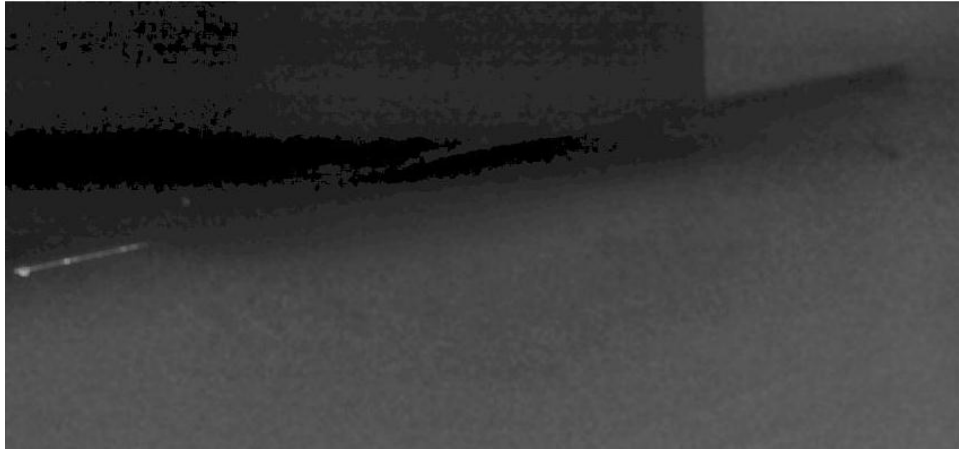


Figure A-5. Blurred image after convolution with 7x7 mean filter.



Figure A-6. Example mask generated for dark regions.

## LIST OF REFERENCES

- [1] Y. Lian, W. Shyy, D. Viieru, and B. Zhang, "Membrane wing aerodynamics for micro air vehicles," *Progress in Aerospace Sciences*, vol. 39, no. 6-7, pp. 425-465, Oct. 2003.
- [2] B. Stanford, P. Ifju, R. Albertani, and W. Shyy, "Fixed membrane wings for micro air vehicles: Experimental characterization, numerical modeling, and tailoring," *Progress in Aerospace Sciences*, vol. 44, no. 4, pp. 258-294, May 2008.
- [3] W. Shyy, P. Ifju, and D. Viieru, "Membrane Wing-Based Micro Air Vehicles," *Applied Mechanics Reviews*, vol. 58, no. 4, p. 283, 2005.
- [4] Y. Abudaram, B. Stanford, and P. Ifju, "Wind Tunnel Testing of Load-Alleviating Membrane Wings at Low Reynolds Numbers," *47th AIAA Aerospace Sciences Meeting*, pp. 1-16, Jan. 2009.
- [5] P. Rojratsirikul, Z. Wang, and I. Gursul, "Unsteady fluid–structure interactions of membrane airfoils at low Reynolds numbers," *Experiments in Fluids*, vol. 46, no. 5, pp. 859-872, Feb. 2009.
- [6] P. Dees, "Hang Glider Design and Performance," *AIAA Aviation Technology, Integration, and Operations Conference*, pp. 1-13, Sep. 2010.
- [7] G. M. Massaro, "Multi-Disciplinary Design of High Aspect Ratio, Gravity Control Hang Glider with Aero Elastically Enhanced Manoeuvrability," *ICAS*, 2000.
- [8] A. Hedenström, L. C. Johansson, M. Wolf, R. von Busse, Y. Winter, and G. R. Spedding, "Bat Flight Generates Complex Aerodynamic Tracks," *Science (New York, N. Y.)*, vol. 316, no. 5826, pp. 894-7, May 2007.
- [9] X. Tian et al., "Direct measurements of the kinematics and dynamics of bat flight," *Bioinspiration & biomimetics*, vol. 1, no. 4, pp. S10-8, Dec. 2006.
- [10] F. T. Muijres, G. R. Spedding, Y. Winter, and A. Hedenström, "Actuator disk model and span efficiency of flapping flight in bats based on time-resolved PIV measurements," *Experiments in Fluids*, Mar. 2011.
- [11] A. Song et al., "Aeromechanics of Membrane Wings with Implications for Animal Flight," *AIAA Journal*, vol. 46, no. 8, pp. 2096-2106, Aug. 2008.
- [12] M. Tamai, J. T. Murphy, and H. Hu, "An experimental study of flexible membrane airfoils at low Reynolds numbers," *AIAA 46<sup>th</sup> Aerospace Sciences Meeting*, pp. 1-12, Jan. 2008.

- [13] R. Albertani, B. Stanford, M. Sytsma, and P. Ifju, "Unsteady Mechanical Aspects of Flexible Wings: an Experimental Investigation Applied to Biologically Inspired MAVs," *European Micro Air Vehicle Conference and Flight Competition*, pp. 17–21 Sep. 2007.
- [14] P. Khambatta, L. Ukeiley, C. Tinney, B. Stanford, and P. Ifju, "Flow Characteristics of a Three-Dimensional Fixed Micro Air Vehicle Wing," *AIAA Fluid Dynamics Conference*, pp. 1-16, Jun. 2008.
- [15] Y. Lian and W. Shyy, "Laminar-Turbulent Transition of a Low Reynolds Number Rigid or Flexible Airfoil," *AIAA Journal*, vol. 45, no. 7, pp. 1501-1513, Jul. 2007.
- [16] C. P. Haggmark, A. A. Bakchinov, and P. H. Alfredsson, "Experiments on a Two-Dimensional Laminar Separation Bubble," *Philosophical Transactions: Mathematical, Physical and Engineering Sciences*, vol. 358, no. 1777, pp. 3193-3205, 2000.
- [17] M. Gaster, "The Structure and Behaviour of Laminar Separation Bubbles," *Aeronautical Research Council Reports and Memoranda*, no. 3595. Her Majesty's Stationary Office, London, 1969.
- [18] A. Pelletier and T. J. Mueller, "Low Reynolds Number Aerodynamics of Low-Aspect-Ratio, Thin/Flat/Cambered-Plate Wings," *Journal of Aircraft*, vol. 37, no. 5, pp. 825-832, Sep. 2000.
- [19] T. J. Mueller and J. D. DeLaurier, "Aerodynamics of Small Vehicles," *Annual Review of Fluid Mechanics*, vol. 35, no. 1, pp. 89-111, Jan. 2003.
- [20] R. C. Michelson, "Overview of Micro Air Vehicle System Design and Integration Issues," *Encyclopedia of Aerospace Engineering*, pp. 1-12, 2004.
- [21] G. Torres and T. J. Mueller, "Micro Aerial Vehicle Development: Design, Components, Fabrication, and Flight-Testing," 2000.
- [22] T. J. Mueller, "Aerodynamic Measurements at Low Reynolds Numbers for Fixed Wing Micro-Air Vehicles," in *RTO AVT / VKI Special Course on Development and Operation of UAVs for Military and Civil Applications*, 1999.
- [23] A. Hedenström, "Aerodynamics , evolution and ecology of avian flight," *Trends in Ecology & Evolution*, vol. 17, no. 9, pp. 415-422, 2002.
- [24] T. J. Mueller, *Fixed and Flapping Wing Aerodynamics for Micro Air Vehicle Applications (Progress in Astronautics and Aeronautics Series, Vol.195)*. AIAA, 2001.

- [25] J. M. Grasmeyer and M. T. Keennon, "Development of the Black Widow Micro Air Vehicle," *AIAA Aerospace Sciences Meeting*, pp. 1-9, Jan. 2001.
- [26] D. J. Pines and F. Bohorquez, "Challenges Facing Future Micro-Air-Vehicle Development," *Journal of Aircraft*, vol. 43, no. 2, pp. 290-305, 2006.
- [27] F. Barnhart, M. Cuipa, D. Stefanik, and Z. Swick, "Micro-Aerial Vehicle Design with Low Reynolds Number Airfoils," design report, Mar. 2004.
- [28] P. G. Ifju, S. Ettinger, D. Jenkins, and L. Martinez, "Composite Materials for Micro Air Vehicles," *SAMPE conference*, pp. 1-12, May. 2001.
- [29] P. G. Ifju, D. A. Jenkins, S. Ettinger, Y. Lian, W. Shyy, and M. R. Waszak, "Flexible-Wing-Based Micro Air Vehicles," *40th AIAA Aerospace Sciences Meeting*, pp. 1-13, 2002.
- [30] B. Thwaites, "The Aerodynamic Theory of Sails. I. Two-Dimensional Sails," *Proceedings of the Royal Society A: Mathematical, Physical and Engineering Sciences*, vol. 261, no. 1306, pp. 402-422, May 1961.
- [31] J. N. Nielsen, "Theory of Flexible Aerodynamic Surfaces," *Journal of Applied Mechanics*, vol. 30, no. 3, p. 435, 1963.
- [32] S. Tanaka and S. Murata, "Aerodynamic characteristics of a two-dimensional porous sail," *Journal of Fluid Mechanics*, vol. 206, pp. 463-475, 1989.
- [33] V. S. Holla, K. P. Rao, C. B. Asthana, and A. Arokkiaswamy, "Aerodynamic Characteristics of Pretensioned Elastics Membrane Rectangular Sailwings," *Applied Mechanics and Engineering*, vol. 44, pp. 1-16, 1984.
- [34] R. Smith and W. Shyy, "Computation of aerodynamic coefficients for a flexible membrane airfoil in turbulent flow: A comparison with classical theory," *Physics of Fluids*, vol. 8, no. 12, p. 3346, 1996.
- [35] R. Galvao et al., "The Aerodynamics of Compliant Membrane Wings Modeled on Mammalian Flight Mechanics," *Fluid Dynamics*, vol. 2866, June, pp. 1-12, 2006.
- [36] R. M. Waldman, A. J. Song, D. K. Riskin, S. M. Swartz, and K. S. Breuer, "Aerodynamic Behavior of Compliant Membranes as Related to Bat Flight," *38th AIAA Fluid Dynamics Conference*, pp. 1-13, 2008.
- [37] K. L. Bishop, "The relationship between 3-D kinematics and gliding performance in the southern flying squirrel, *Glaucomys volans*," *The Journal of experimental biology*, vol. 209, no. 4, pp. 689-701, Feb. 2006.

- [38] S. Arbos-Torrent, Z. Y. Pang, B. Ganapathisubramani, and R. Palacios, "Leading and trailing edge effects on the aerodynamic performance of compliant aerofoils," *49th AIAA Aerospace Sciences Meeting*, pp. 1-16, Jan. 2011.
- [39] P. Rojratsirikul, M. S. Genc, Z. Wang, and I. Gursul, "Flow-induced vibrations of low aspect ratio rectangular membrane wings," *Journal of Fluids and Structures*, pp. 1-14, Jul. 2011.
- [40] P. Rojratsirikul, Z. Wang, and I. Gursul, "Effect of pre-strain and excess length on unsteady fluid–structure interactions of membrane airfoils," *Journal of Fluids and Structures*, vol. 26, no. 3, pp. 359-376, Apr. 2010.
- [41] R. E. Gordnier and M. R. Visbal, "Implicit LES Computations with Applications to Micro Air Vehicles," in *2009 DoD High Performance Computing Modernization Program*, pp. 73-80, 2009.
- [42] S. Tiomkin, D. E. Raveh, and R. Arieli, "Parametric Study of a Two-dimensional Membrane Wing in Viscous Laminar Flow," *29th AIAA Applied Aerodynamics Conference*, pp. 1-23, Jun. 2011.
- [43] R. E. Gordnier and P. J. Attar, "Aeroelastic Simulations of an Aspect Ratio Two Flexible Membrane Wing," *50th AIAA Aerospace Sciences Meeting*, pp. 1-17, Jan. 2012.
- [44] L. Tregidgo, Z. Wang, I. Gursul, U. Kingdom, D. Current, and P. Student, "Pitching Motion at a Low Reynolds Number," *41<sup>st</sup> AIAA Fluid Dynamics Conference*, pp. 1-20, Jun. 2011.
- [45] H. Hu, M. Tamai, and J. T. Murphy, "Flexible-Membrane Airfoils at Low Reynolds Numbers," *Journal of Aircraft*, vol. 45, no. 5, pp. 1767-1778, Sep. 2008.
- [46] K. D. Scott, J. P. Hubner, L. Ukeiley, and P. G. Ifju, "Effects of Membrane Vibration on the Flow Field Surrounding Flat-Plate Membrane Airfoils," *49th AIAA Aerospace Sciences Meeting*, pp. 1-17, Jan. 2011.
- [47] J. W. Johnston, W. Romberg, P. J. Attar, and R. Parthasarathy, "Experimental Characterization of Limit Cycle Oscillations in Membrane Wing Micro Air Vehicles," *Journal of Aircraft*, vol. 47, no. 4, pp. 1300-1308, Jul. 2010.
- [48] P. J. Attar, R. E. Gordnier, J. W. Johnston, W. a. Romberg, and R. N. Parthasarathy, "Aeroelastic Analysis of Membrane Microair Vehicles—Part I: Flutter and Limit Cycle Analysis for Fixed-Wing Configurations," *Journal of Vibration and Acoustics*, vol. 133, no. 2, p. 021008, 2011.

- [49] J. N. Mastramico and J. P. Hubner, "A Study of the Wake Characteristics for Membrane Flat and Cambered Plates," *26th AIAA Aerodynamic Measurement Technology and Ground Testing Conference*, pp. 1-13 2008.
- [50] J. P. Hubner and T. Hicks, "Trailing-edge scalloping effect on flat-plate membrane wing performance," *Aerospace Science and Technology*, vol. 1, pp. 1-11, Jan. 2011.
- [51] Y. J. Abudaram, P. G. Ifju, J. P. Hubner, and L. Ukeiley, "Controlling Pre-tension of Silicone Membranes on Micro Air Vehicle Flexible Wings," *50th AIAA Aerospace Sciences Meeting*, pp. 1-11, Jan. 2012.
- [52] R. Albertani et al., "Validation of a Low Reynolds Number Aerodynamic Characterization Facility," *47th AIAA Aerospace Sciences Meeting*, pp. 1-10, Jan. 2009.
- [53] M. Raffel, C. E. Willert, S. T. Wereley, and J. Kompenhans, "Particle Image Velocimetry," *2nd ed.* Springer, 2007.
- [54] L. Strömungsmechanik, "Tracer particles and seeding for particle image velocimetry," *Measurement Science and Technology*, vol. 8, pp. 1406-1416, 1997.
- [55] A. Prasad, "Particle image velocimetry," *Current Science*, vol. 79, no. 1, pp. 51-60, Jul. 2000.
- [56] Z. Zhang, J. P. Hubner, A. Timpe, L. Ukeiley, Y. Abudaram, and P. Ifju, "Effect of Aspect Ratio on Flat-Plate Membrane Airfoils," *50th AIAA Aerospace Sciences Meeting*, pp. 1-15, 2012.
- [57] "DantecDynamics," *DynamicStudio Product Manual v3.10*, 2010.
- [58] R. Maini, "Study and Comparison of Various Image Edge Detection Techniques," *Image Processing*, vol. 147002, no. 3, pp. 1-12.
- [59] N. Ostu, "A Threshold Selection Method from Gray-Level Histograms," *IEEE Systems, man and Cybernetics*, vol. 9, no. 1, pp. 62-66, 1979.
- [60] R. L. Panton, *Incompressible Flow*, 3rd ed. J. Wiley, pp. 71-144 2005.
- [61] M. Okamoto and a. Azuma, "Aerodynamic Characteristics at Low Reynolds Numbers for Wings of Various Planforms," *AIAA Journal*, vol. 49, no. 6, pp. 1135-1150, Jun. 2011.
- [62] S. B. Pope, *Turbulent Flows*. Cambridge University Press, pp. 85-87, 2000.

- [63] J. S. Bendat and A. G. Piersol, *Random Data: Analysis and Measurement Procedures*, 4th ed. Wiley, pp. 368, 545, 2010.
- [64] Y. A. Cengel and J. M. Cimbala, *Fluid Mechanics: Fundamentals and Applications*. McGraw-Hill Higher Education, pp. 144-145, 2006.

## BIOGRAPHICAL SKETCH

Amory Timpe was born in the year of 1986 in the city of Athens, Georgia. He survived as the middle child with an older brother and younger sister, whom he dearly loves. Prior to previous recollection, his family moved to Winter Haven, Florida, where he grew up in awe of Florida's great Space Coast. This instilled in him a passion for feats of aerospace engineering and human flight. His other passion from a young age is one for the sport of hockey, even living in sunny Florida. He decided to pursue high school education at the International Baccalaureate (IB) world school housed at Bartow Senior High to ensure the best chance of becoming an aerospace engineer, graduating in 2005.

Accepted to the University of Florida, the next years were spent living and learning in Gainesville, Florida. In Gainesville he enjoyed participating in UF's Men's Roller Hockey Club, holding office and traveling to play tournaments against rival schools. An avid sports and Gators fan, he was fortunate to participate in intramural sports and to witness multiple NCAA national titles during his undergraduate studies.

He began undergraduate research in his junior year where he was able to assist with wind tunnel testing and airfoil designs, under guidance of Dr. Louis Cattafesta. In the fall of 2009, he graduated with a B.S. in mechanical engineering. Continuing research, he began a master's project in the fall of 2010 to study low Re membrane wing and flow interactions with advisor Dr. Lawrence Ukeiley. With the completion of his master's degree in aerospace engineering, Amory hopes to find work in the aerospace technology industry after graduating in May of 2012.